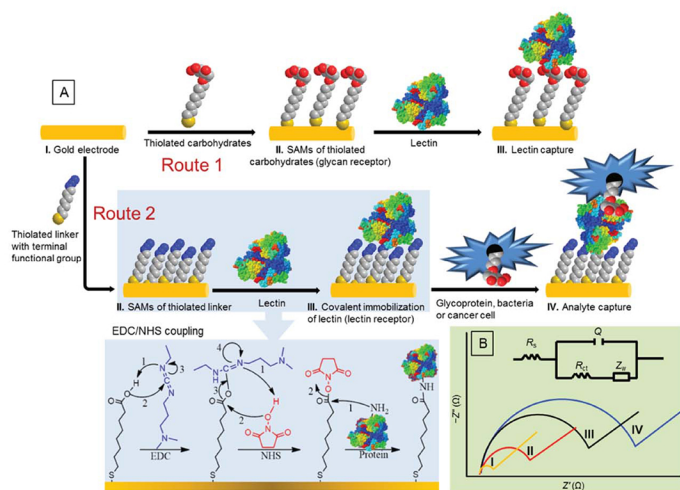


Jennie Brock  
Editor

# Electrochemical Impedance Spectroscopy

## Methods, Analysis and Research



CHEMISTRY RESEARCH AND APPLICATIONS

NOVA



**CHEMISTRY RESEARCH AND APPLICATIONS**

**ELECTROCHEMICAL  
IMPEDANCE SPECTROSCOPY  
METHODS, ANALYSIS  
AND RESEARCH**

No part of this digital document may be reproduced, stored in a retrieval system or transmitted in any form or by any means. The publisher has taken reasonable care in the preparation of this digital document, but makes no expressed or implied warranty of any kind and assumes no responsibility for any errors or omissions. No liability is assumed for incidental or consequential damages in connection with or arising out of information contained herein. This digital document is sold with the clear understanding that the publisher is not engaged in rendering legal, medical or any other professional services.

# **CHEMISTRY RESEARCH AND APPLICATIONS**

Additional books in this series can be found on Nova's website under the Series tab.

Additional e-books in this series can be found on Nova's website under the eBooks tab.

**CHEMISTRY RESEARCH AND APPLICATIONS**

**ELECTROCHEMICAL  
IMPEDANCE SPECTROSCOPY**

**METHODS, ANALYSIS  
AND RESEARCH**

**JENNIE BROCK**  
**EDITOR**



Copyright © 2017 by Nova Science Publishers, Inc.

**All rights reserved.** No part of this book may be reproduced, stored in a retrieval system or transmitted in any form or by any means: electronic, electrostatic, magnetic, tape, mechanical photocopying, recording or otherwise without the written permission of the Publisher.

We have partnered with Copyright Clearance Center to make it easy for you to obtain permissions to reuse content from this publication. Simply navigate to this publication's page on Nova's website and locate the "Get Permission" button below the title description. This button is linked directly to the title's permission page on copyright.com. Alternatively, you can visit copyright.com and search by title, ISBN, or ISSN.

For further questions about using the service on copyright.com, please contact:

Copyright Clearance Center

Phone: +1-(978) 750-8400

Fax: +1-(978) 750-4470

E-mail: info@copyright.com.

### **NOTICE TO THE READER**

The Publisher has taken reasonable care in the preparation of this book, but makes no expressed or implied warranty of any kind and assumes no responsibility for any errors or omissions. No liability is assumed for incidental or consequential damages in connection with or arising out of information contained in this book. The Publisher shall not be liable for any special, consequential, or exemplary damages resulting, in whole or in part, from the readers' use of, or reliance upon, this material. Any parts of this book based on government reports are so indicated and copyright is claimed for those parts to the extent applicable to compilations of such works.

Independent verification should be sought for any data, advice or recommendations contained in this book. In addition, no responsibility is assumed by the publisher for any injury and/or damage to persons or property arising from any methods, products, instructions, ideas or otherwise contained in this publication.

This publication is designed to provide accurate and authoritative information with regard to the subject matter covered herein. It is sold with the clear understanding that the Publisher is not engaged in rendering legal or any other professional services. If legal or any other expert assistance is required, the services of a competent person should be sought. **FROM A DECLARATION OF PARTICIPANTS JOINTLY ADOPTED BY A COMMITTEE OF THE AMERICAN BAR ASSOCIATION AND A COMMITTEE OF PUBLISHERS.**

Additional color graphics may be available in the e-book version of this book.

### **Library of Congress Cataloging-in-Publication Data**

ISBN: ; 9: /3/75834/452/7\*\*gDqqm†

*Published by Nova Science Publishers, Inc. † New York*

# CONTENTS

<b>Preface</b>	<b>vii</b>	
<b>Chapter 1</b>	Carbohydrate–Protein Interactions Studied Using Electrochemical Impedance Spectroscopy	<b>1</b>
	<i>Jay K. Bhattacharai, Vasilii Mikhaylov, Dharmendra Neupane, Bishal Nepal, Alexei V. Demchenko and Keith J. Stine</i>	
<b>Chapter 2</b>	An Electrochemical Study About the Stability and Durability of Poly(O-Aminophenol) Film Electrodes Employing Impedance Spectroscopy and Surface Resistance	<b>29</b>
	<i>Ricardo Tucceri</i>	
<b>Chapter 3</b>	The Effect of Cerium Content on the Corrosion Behavior of Amorphous Al <sub>85</sub> Ce <sub>x</sub> Ni <sub>15-x</sub> (x = 4, 5, 6, 7, and 10) Alloys Obtained by Melt Spinning	<b>77</b>
	<i>Carlos Triveño Ríos, Mara Cristina Lopes de Oliveira and Renato Altobelli Antunes</i>	
<b>Index</b>		<b>97</b>



## PREFACE

In Chapter One, the authors review the recent developments in the field of electrochemical impedance spectroscopy, discuss some of the challenges and compare EIS with the other relevant techniques. The effect of storage time without use (STWU) in the supporting electrolyte solution on the conducting properties of poly(o-aminophenol) (POAP) film electrodes was studied in Chapter Two. In Chapter Three, the authors study the effect of the cerium content on the corrosion behavior of Al<sub>85</sub>Ce<sub>x</sub>Ni<sub>15-x</sub> ( $x = 4, 5, 6, 7$  and  $10$ ) amorphous alloys obtained by melt spinning.

Chapter 1 – Carbohydrates (glycans) are very important molecules for clinical diagnosis and development. The interactions of carbohydrates with different proteins are found to be involved in many physiological and pathological conditions, including cell-cell adhesion, cell proliferation, inflammation, cancer-cell metastasis, and bacterial and viral invasion. The importance of understanding these phenomena have led to the development of a wide variety of techniques among which label-free techniques, such as surface plasmon resonance, quartz-crystal microbalance and electrochemical impedance spectroscopy (EIS) are widely used. The popularity of EIS among these is due to its sensitivity, ease of sample preparation steps, low costs and rapid measurements. The EIS technique is used to study carbohydrate–protein interactions with the two main goals: (1) sensitivity–detecting the smallest possible concentration of the analyte in the sample and (2) selectivity–determining weak biological interactions by finding the affinity constant. Owing to the ease of synthesis, stability at working conditions, and small size, carbohydrates are frequently used as bioreceptors by coupling to transducers to detect the desired analytes. However, the glycan part of glycoproteins is

commonly used as an analyte when treated as a biomarker, and a suitable lectin is used as a bioreceptor. Aberration in glycosylation and change in concentration of specific carbohydrates can be linked to a possible disease condition; early diagnosis of which can help effectively treat the disease. In this chapter, the authors review the recent developments in the field, discuss some of the challenges and compare EIS with the other relevant techniques.

Chapter 2 – The effect of storage time without use (STWU) in the supporting electrolyte solution on the conducting properties of poly(*o*-aminophenol) (POAP) film electrodes was studied. Cyclic voltammetry (CV), rotating disc electrode voltammetry (RDEV), Electrochemical Impedance Spectroscopy (EIS and surface resistance (SR) were employed. The storage of a POAP film without use for time periods longer than 32 h strongly reduces its electroactivity. Here, this effect is called deactivation. The attenuation of the voltammetric response of the polymer film with the increase of the storage time allows one to define a degree of deactivation ( $\theta_d$ ). A decrease of the electron transport rate ( $D_e$ ) with the increase of the degree of deactivation of POAP films was obtained from RDEV measurements. This effect was attributed to the increase of the mean distance between active redox sites in the bulk of the POAP film. The relative surface resistance change ( $\Delta R/R$ ) of a gold film coated with POAP is also attenuated by the increase of the STWU. The attenuation was attributed to interfacial (gold/POAP) redox site distributions where the nearest neighbor distance between redox sites gradually increases as the degree of deactivation increases. Impedance spectra of POAP films in the presence of an electroactive solution and in the sole presence of the supporting electrolyte were analyzed on the basis of two different impedance models: The deactivation of POAP films by the STWU studied in this work was compared with deactivations caused by other electrochemical and chemical treatments, such as prolonged potential cycling (PPC), high positive potential limits (HPPL) and soaking in a ferric ion solution (SFeIS), described in previous work.

Chapter 3 – The aim of the present work was to study the effect of the cerium content on the corrosion behavior of Al<sub>85</sub>Ce<sub>x</sub>Ni<sub>15-x</sub> (x = 4, 5, 6, 7 and 10) amorphous alloys obtained by melt spinning. The as-quenched amorphous ribbons were studied by differential scanning calorimetry and the amorphous character was confirmed by X-ray diffraction and transmission electron microscopy. The corrosion behavior was investigated using electrochemical impedance spectroscopy and potentiodynamic polarization. The results showed that the Al<sub>85</sub>Ce<sub>x</sub>Ni<sub>15-x</sub> alloys were amorphous independently of the

cerium concentration. The corrosion behavior was dependent on the cerium concentration. The general corrosion resistance decreased with the cerium content. However, increasing the cerium content led to a beneficial effect on the localized corrosion resistance of the alloys.



***Chapter 1***

**CARBOHYDRATE–PROTEIN INTERACTIONS  
STUDIED USING ELECTROCHEMICAL  
IMPEDANCE SPECTROSCOPY**

*Jay K. Bhattacharai, Vasili Mikhaylov,  
Dharmendra Neupane, Bishal Nepal,  
Alexei V. Demchenko and Keith J. Stine\**

Department of Chemistry and Biochemistry,  
University of Missouri St. Louis, Saint Louis, USA

**ABSTRACT**

Carbohydrates (glycans) are very important molecules for clinical diagnosis and development. The interactions of carbohydrates with different proteins are found to be involved in many physiological and pathological conditions, including cell-cell adhesion, cell proliferation, inflammation, cancer-cell metastasis, and bacterial and viral invasion. The importance of understanding these phenomena have led to the development of a wide variety of techniques among which label-free techniques, such as surface plasmon resonance, quartz-crystal microbalance and electrochemical impedance spectroscopy (EIS) are

---

\* Corresponding Author Email: [kstine@umsl.edu](mailto:kstine@umsl.edu).

widely used. The popularity of EIS among these is due to its sensitivity, ease of sample preparation steps, low costs and rapid measurements. The EIS technique is used to study carbohydrate–protein interactions with the two main goals: (1) sensitivity—detecting the smallest possible concentration of the analyte in the sample and (2) selectivity—determining weak biological interactions by finding the affinity constant. Owing to the ease of synthesis, stability at working conditions, and small size, carbohydrates are frequently used as bioreceptors by coupling to transducers to detect the desired analytes. However, the glycan part of glycoproteins is commonly used as an analyte when treated as a biomarker, and a suitable lectin is used as a bioreceptor. Aberration in glycosylation and change in concentration of specific carbohydrates can be linked to a possible disease condition; early diagnosis of which can help effectively treat the disease. In this chapter, we review the recent developments in the field, discuss some of the challenges and compare EIS with the other relevant techniques.

**Keywords:** EIS, carbohydrate–protein interactions, biosensing, charge-transfer resistance

## INTRODUCTION

Carbohydrate–protein interactions are linked to many important biological phenomena. Life originates (fertilization and proliferation), functions (cell-cell signaling and adhesion) and may end (inflammation, cancer-cell metastasis, bacterial and viral invasion) with these interactions [1-2]. Scientists have taken advantage of these interactions to design drugs and specifically target cancer cells and viruses [3], design vaccines to block the receptors and inhibit infection by viruses [4-5] and prepare biosensors for early detection of disease [6]. There are many analytical techniques discovered to study such interactions, which can loosely be categorized into labeling and label-free techniques. The labeling technique uses a tag in the molecules of interest for the study of carbohydrate–protein interactions, such as fluorescent [7], electrochemically active probe [8], enzymes [9-10], nanoparticles [10], and isotopes [11]. These labeling techniques have shown enhanced sensitivity; however, there are a number of shortcomings associated with them. Since the labeling is the incorporation of foreign materials on the molecules of interest, they may produce false positive or negative results. On the other hand, labeling is cumbersome and time-consuming, while labeling with radioactive isotopes has raised some safety concerns. Unlike labeling techniques, label-

free techniques use a change in a property of a transducer by simply monitoring presence or absence of the molecules of interest. The responses are generally obtained in the form of optical, electrochemical, or mechanical signals. Label-free techniques are also more convenient for studying real-time interactions. Most of the commonly used label-free techniques are based on plasmonics [12], impedance [13] or the piezoelectric effect [14]. In this chapter, our focus is to discuss the use of the impedance-based technique to study carbohydrate–protein interactions.

Impedance is the ability of a circuit to resist the flow of electric current, and the technique where impedance is plotted versus the frequency is called electrochemical impedance spectroscopy (EIS) [15]. The concept of EIS has been around for more than 100 years [16]. The foundation for impedance spectroscopy was laid by Oliver Heaviside in the late 19th century [17]. In those early days of development, EIS was mostly employed to measure the capacitance of ideally polarizable electrodes which resulted in the development of various models for electrified interfaces [16-17]. Despite having such a long history, it wasn't until the 1970s that it was explored as a tool for electrochemical measurement, which is credited to development of instruments combining potentiostats and frequency response analyzers [16]. Since then, EIS has been continuously developed and used to study various processes, such as metal corrosion [18], electron transport in the dye-sensitized solar cell [19], and biosensing [20].

The concept of the impedance was derived from the resistance which is defined by Ohm's law as a ratio of voltage ( $E$ ) and current ( $I$ ). The Ohm's law is simple concept of resistance which excludes the frequency and time dependent phase shift between sinusoidal current and voltage.

When expressed as a function of time ( $t$ ), the excitation sinusoidal potential is expressed as ( $E_t$ ) =  $E_0\text{Sin}(\omega t)$  and the response current ( $I_t$ ) =  $I_0\text{Sin}(\omega t + \phi)$ , where  $E_0$  and  $I_0$  are the amplitudes of potential and current respectively,  $\omega$  is radial frequency in radians/second (=  $2\pi f$ , where  $f$  is frequency in hertz), and  $\phi$  is the phase angle difference between current and potential. Then impedance ( $Z$ ) can be expressed as [21]

$$Z = \frac{E_t}{I_t} = \frac{E_0\text{Sin}(\omega t)}{I_0\text{Sin}(\omega t + \phi)} = Z_0 \frac{\text{Sin}(\omega t)}{\text{Sin}(\omega t + \phi)} \quad (1)$$

Using Euler's formula, the impedance can be expressed as a complex function [22],

$$Z(\omega) = |Z|e^{j\phi} = Z_0(\cos\phi + j\sin\phi) = Z' + jZ'' \quad (2)$$

Where  $j = (-1)^{1/2}$ , and  $Z'$  and  $Z''$  are real and imaginary impedance, respectively.

Since EIS can probe the nature of the electrode by applying a small sinusoidal potential (2–10 mV) as a function of frequency, it became the ideal candidate for studying biomolecular interactions. In the past decade, EIS has been heavily used for studying different types of biomolecular interactions, including carbohydrate–protein, protein–protein, and protein–DNA mainly because of the simplicity, cost-effectiveness and sensitivity of the technique [23–25]. This also led to its use in the detection of various disease biomarkers, bacteria and viruses as a biosensor technique [26]. EIS is also of particular interest because of its possibility to be used in miniaturized point-of-care devices. One of the critical issues for the biosensor detection is the background noise in the original sample, such as untargeted proteins, lipids, electrolytes etc. in the serum sample. To overcome this challenge, the sample should either be purified or diluted. The dilution technique is a good way to reduce the background noise; unfortunately, the analyte of interest will also get diluted. With EIS, detection of very small concentration of sample from nanomolar to attomolar range is possible [27].

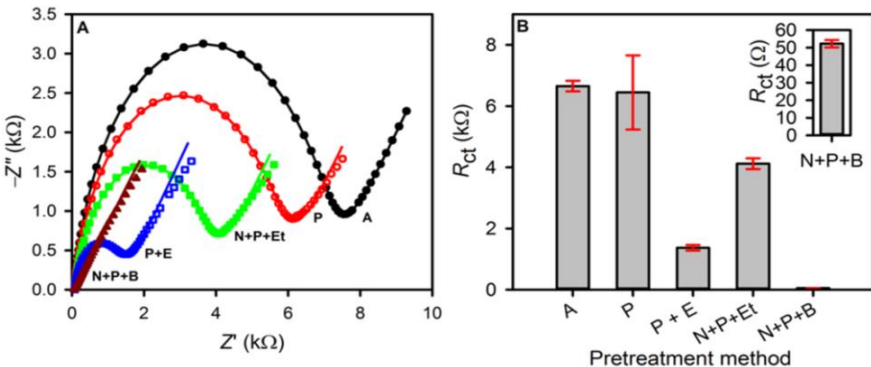


Figure 1. Comparison of bare gold wire (GW) before and after pretreatment A) Nyquist plots of the bare GW as-purchased (A) and after piranha cleaning (P), piranha + one-step chronoamperometric cleaning in 0.5 M  $H_2SO_4$  providing potential of –1.0 V for 1 min, 5 times (P + E), nitric acid + piranha + ethanol cleaning (N + P + Et), nitric acid + piranha + sodium borohydride + ethanol cleaning (N + P + B). B) Bar graph showing error bars in  $R_{ct}$  of different pretreatment methods, where error bars indicate the SD of four measurements. Reprinted with permission from reference [31]. Copyright 2016 Elsevier.

EIS data are most commonly expressed in the form of a Bode plot [28] or a Nyquist plot [29]. In a Bode plot, impedance is plotted versus the frequency; whereas in a Nyquist plot, the imaginary impedance component is plotted versus the real part of the impedance to obtain a semicircle at high frequency and a linear component at lower frequency [30]. The semicircle component in a Nyquist plot represents the charge or electron transfer limiting process at the electrode surface, whose value is calculated by measuring the diameter of the semicircle. The increase in the diameter of the semicircle means the increase in charge transfer resistance ( $R_{ct}$ ) and vice versa. The linear component of the Nyquist plot represents a diffusion-limited process. The Nyquist plot can be fitted with different types of equivalent circuits to obtain the required information. One of the most commonly utilized equivalent circuits for biosensing experiments is the Randles equivalent circuit, which consists of solution resistance ( $R_s$ ), charge transfer resistance ( $R_{ct}$ ), Warburg impedance ( $Z_w$ ) and a constant-phase element or non-ideal capacitor ( $Q$ ) [31]. The kinetics of the redox reaction of the probe at the electrode surface can be represented by  $R_{ct}$  and  $Q$ . However,  $Q$  is easily affected by the surface roughness of the electrode and chemical inhomogeneity [32-33], so  $R_{ct}$  is commonly used for Faradaic-based biosensing and  $Q$  is used for non-Faradaic-based biosensing [33]. On the other hand,  $Z_w$ , which represent the diffusion phenomenon, and  $R_s$  are the properties of the electrolyte solution and do not represent the dielectric properties of the electrode-electrolyte interface [34].

## ELECTRODES AND ELECTROLYTES

The electrodes used for studying the carbohydrate–protein interactions using EIS should be robust and conductive. Gold is the most commonly used electrode for EIS mainly because of its ability to form self-assembled monolayers. However, other properties of gold such as mechanical robustness, electrical conductivity and chemical inertness are also important factors for choosing gold as an electrode of choice. Moreover, gold electrodes can be easily cleaned by mechanical polishing, chemical treatment and/or electrochemical methods for multiple uses. However, it is very important to properly clean the gold surface before its use. Bertok and coworkers have reported that the sensitivity of the EIS also depends on the initial  $R_{ct}$  of the blank electrode. They found the limit of detection of glycoprotein fetuin on *Sambucus nigra* agglutinin (SNA) lectin is 73 pM when initial  $R_{ct}$  was 620  $\Omega$ , and 24 fM when initial  $R_{ct}$  was 32 k $\Omega$  [35]. However, one should also be aware that having higher initial  $R_{ct}$  may also be due to contaminants or a

thicker oxide layer on the surface of the electrode, which can easily interfere in the EIS response, making it challenging to obtain reproducible data. Our lab has reported an easy and reproducible gold electrode cleaning procedure for use in EIS experiments, Figure 1. However, other types of electrodes such as indium tin oxide (ITO) and screen-printed electrode modified with single-walled carbon nanotubes can also been used for studying carbohydrate–protein interactions using EIS [28, 36].

Electrolyte solution for EIS experiments most commonly consists of the redox probe of potassium hexacyanoferrate(III) and potassium hexacyanoferrate(II) in 1:1 molar ratio at concentration around 1 to 10 mM. The probes are commonly prepared in phosphate, HEPES or tris-buffer solution containing 0.1 M NaCl. It is very important to choose appropriate buffer type and maintain the low concentration of the probe for EIS experiments. The interfering effect of higher concentrations of probe solution can be seen when measurements are repeated on the same electrode without changing any other parameters [37]. It has been found that impedance keeps increasing after each additional scan up to a certain number of scans. However, the change in  $R_{ct}$  keeps decreasing before finally a constant value is obtained, which shows that the probe solution creates some interference. This can be minimized by decreasing the concentration of the probe solution to less than 5 mM [37]. The buffer solution, on the other hand, can have an affinity to gold surface and may also precipitate the metal ions ( $\text{Ca}^{2+}$  and  $\text{Mn}^{2+}$ ) necessary for the enhancing the affinity of lectins toward the glycan moiety. In one critical work toward EIS, it has also been reported that the cyanide ions have an etching effect toward gold, creating challenges in reproducing the results [38], however, more work is needed to support this statement. The presence of metal ions like  $\text{Ca}^{2+}$ ,  $\text{Mn}^{2+}$ , or  $\text{Mg}^{2+}$  in the probe solution can also have interfering effects.

## IMMOBILIZATION OF GLYCANS VERSUS LECTINS

Carbohydrate–protein interactions can be studied either by immobilizing carbohydrate or protein that acts as a receptor on the electrode surface. The goal of the immobilized receptor is to mimic the cell surface or the natural state of carbohydrate and protein so that in vitro study can be performed for the detection of pathogens or targeted biological molecules. The schematic diagram of the strategies to prepare glycan receptor and lectin receptor is presented in Figure 2A, and schematic of the corresponding Nyquist plots at each step are shown in Figure 2B.

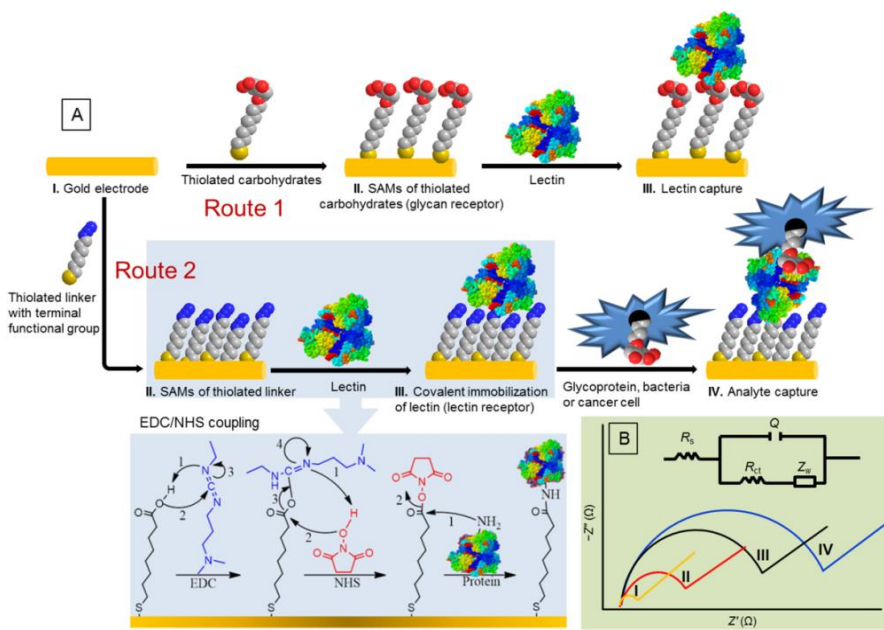


Figure 2. Schematic diagram of electrode modification strategies for studying carbohydrate–protein interactions using EIS. (A) Route 1: glycan receptor preparation and capturing lectin and route 2: lectin receptor preparation and capturing analytes like glycoprotein, bacteria or cancer cells. Bottom left is a mechanism for EDC/NHS coupling to immobilized lectin on the gold electrode modified with SAMs. (B) Schematic diagram showing shift of Nyquist plot during different steps of electrode modification. Inset is the Randles equivalent circuit corresponding to Nyquist plots.

## Glycan Receptor

In EIS experiments, small molecules are generally preferred as a receptor and larger molecules as an analyte. Since the pure glycan moiety is mono-, di-, or oligosaccharides, their sizes are smaller compared to the lectins. When the lectin is immobilized first, the response due to the pure glycan is difficult to monitor because of their smaller size. Therefore, for the experiments where the goal is to determine the binding constants of pure glycan moiety and the targeted lectin, preparing glycan as a receptor clearly has an advantage. The glycans to be used as a receptor can be synthesized chemically or isolated from the natural sources. The most common approach to present the glycans on the surface is through a self-assembled monolayer by chemically modifying the carbohydrates with organosulfur molecules (Figure 2A, route 1). This can

be done either by direct SAM formation on the gold surface or by the indirect method where a SAM presenting a suitable terminal functional group is prepared first, followed by use of click chemistry to capture modified or unmodified carbohydrates of interest [39]. Pure SAMs of the thiolated carbohydrates or mixed with thiolated polyethylene glycol in different ratio can be prepared by simply immersing gold electrode in ethanolic solution of the desired compounds for 1 h to overnight. Mixed SAM can help control the density of the terminal sugar and avoid the non-specific interactions of lectins. However, mixed SAM should be chosen carefully as not all the ratios improve the binding between carbohydrates and lectins [31]. Therefore, before choosing the ratio randomly, it is always preferred to perform the experiment to find the optimal ratio. Figure 3A shows the change in  $R_{ct}$  when lectin Concanavalin A (Con A) is captured on the different ratios of the mixed SAMs of thiolated mannosides (Man-C<sub>8</sub>-SH) and thiolated triethylene glycol (TEG-SH). It can be seen that a 1:1 ratio is decreasing the response from that of pure SAMs. This might be because of the unfavorable orientation of mannose for capturing Con A or at this ratio less mannose is immobilized on the electrode surface. The optimal response was found when 1:4 molar ratios were used. The Nyquist plots at different steps of capturing Con A by SAM prepared at 1:4 mixed ratios are shown in Figure 3B. The Con A interaction with mixed SAMs is evident by  $\Delta R_{ct} = 495 \pm 15 \Omega$  which is  $80 \pm 10 \Omega$  for the non-specific interaction of lectin peanut agglutinin (PNA).

Besides forming SAMs, there are other ways to present terminal carbohydrates on the electrode surface. Wang and coworkers immobilized mannose functionalized aniline polymer (manno-PANI) on indium tin oxide (ITO) glass slide for studying interaction with Con A finding a limit of detection of 0.12 nM [28].

## Lectin Receptor

Lectins are the type of proteins found in plants and animals that can specifically recognize carbohydrates in pure form or in the glycan moieties found on glycoproteins, immunoglobulins, glycolipids, bacteria and virus surface and cell surfaces. The affinity of lectins toward bound glycan moieties is found to be relatively less compared to free carbohydrates. The lectin binding to glycans is a reversible process, which makes isolation of glycoproteins and glycolipids easy from the mixture of sample extract by passing free carbohydrates through the captured glycoproteins and glycolipids.

A lectin array can be prepared by covalently immobilizing the lectin on self-assembled monolayers prepared on gold electrodes [40]. Although lectins can be isolated from various sources such as plant, bacterial, virus, and animals, the plant-based lectins are popular for their use as a receptor in EIS-based electrode because of their ease of preparation and cost. Some of the commonly used lectins, common source and their carbohydrate specificity along with the target analytes are provided in Table 1.

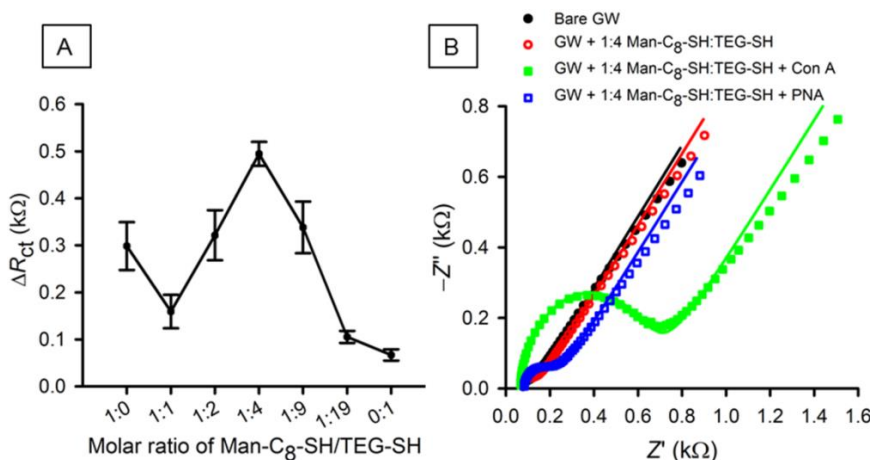


Figure 3. (A) Change in  $R_{ct}$  when Con A (0.5  $\mu$ M) was immobilized on gold wire modified with the mixture of Man-C<sub>8</sub>-SH and TEG-SH in different molar ratios (total concentration = 1 mM). Error bars indicate the SD of three measurements. (B) Nyquist plots showing an increase in  $R_{ct}$  when Con A was captured (solid square) on mixed SAMs formed by 1:4 mol ratio of Man-C<sub>8</sub>-SH and TEG-SH (open circle) on GW (solid circle). PNA was used as a control (open square). The solid lines in B are the fit to the equivalent circuit. Reprinted with permission from reference [29]. Copyright 2016 Elsevier.

Lectin receptor is very important in detecting glycoprotein biomarkers associated with various diseases. Most of the cancer biomarkers approved by US FDA are in glycosylated form [41-42]. Therefore, by choosing a suitable lectin receptor low biomarker concentrations can be determined for the early detection of disease. The common way to immobilize a lectin receptor on the electrode surface is through EDC/NHS (EDC = 1-ethyl-3-(3-dimethylaminopropyl) carbodiimide, NHS = *N*-hydroxysuccinimide) crosslinking reaction of terminal carboxyl group of SAM and amine groups of lysine residues on the lectin. The detailed mechanism of EDC/NHS chemistry is shown in the magnified rectangular box in Figure 2A, route 2. However, there

are other approaches to present the lectin on the electrode surface. Luna and coworkers used liposome immobilized on the gold electrode surface to capture Con A, which then is used for detecting serum glycoproteins in dengue infected patients [48].

**Table 1. Common lectins, their source, specificity, and analytes [41-44].**

Lectin/Agglutinin (Abbr.)	Common source	Specific carbohydrate	Analyte	Cancer
Peanut (PNA)	<i>Arachis hypogaea</i>	Gal $\beta$ -1,3GalNAc	CEA*	Colorectal
Jacalin (AIL)	<i>Artocarpus integrifolia</i>	Gal $\beta$ -1,3GalNAc	leukemic cells THP-1 and OCI-AMI3 [45]	Circulating tumor cells
Concanavalin A (Con A)	<i>Canavalia ensiformis</i>	$\alpha$ -D-Man, $\alpha$ -D-Glc	Serum glycoproteins from patients infected by dengue fever [46]	n/a
Soybean (SBA)	<i>Glycine max</i>	$\alpha/\beta$ -Gal; $\alpha/\beta$ -GalNAc	n/a	n/a
Griffonia simplicifolia (GSL)	<i>Griffonia simplicifolia</i>	$\alpha/\beta$ -GlcNAc	CA125/HE4*	Ovarian
Lens culinaris (LCA)	<i>Lens culinaris</i>	$\alpha$ -D-Man, $\alpha$ -D-Glc	$\alpha$ -fetoprotein*	Testicular and Liver
Maackia amurensis (MAA/MAL)	<i>Maackia amurensis I</i>	$\alpha$ -2,3Neu5Ac	CA15.3/CA27.29*	Breast
Ricinus communis (RCA-I/RCA60)	<i>Ricinus communis I</i>	$\beta$ -D-Gal	n/a	n/a
Ricinus communis (RCA-II/RCA120)	<i>Ricinus communis II</i>	Gal $\beta$ -1,4GalNAc	n/a	n/a
Sambucus nigra (SNA)	<i>Sambucus nigra</i>	Neu5Aca-2,6Gal/GalNAc	Transferrin and bovine submaxillary mucin antigen [47]	sialyl-Tn containing glycoproteins
Wheat Germ (WGA)	<i>Triticum vulgaris</i>	$\beta$ -D-GlcNAc, Neu5Ac	PSA*	Prostate
Ulex europaeus (UEA)	<i>Ulex europaeus</i>	Fuc $\alpha$ -1,2Gal	HER2*	Breast
Wisteria floribunda (WFL)	<i>Wisteria floribunda</i>	$\alpha/\beta$ -GalNAc	Tg*	Thyroid

Gal: galactose GaINAc: N-acetyl galactosamine, Man: mannose, Glc: glucose, GlcNAc: N-acetyl glucosamine, Neu5Ac: N-acetylneurameric acid (sialic acid), Fuc: fucose CA125: cancer antigen 125; CEA: carcinogenic embryonic antigen; HE4: human epididymis protein 4; PSA: prostate-specific antigen; Tg: thyroglobulin

\* US FDA-approved cancer biomarkers for various types of cancer

## STUDY OF CARBOHYDRATE–PROTEIN INTERACTIONS USING EIS

### 1. Pathogenic Bacteria

*E. coli* is a common bacteria naturally occurring in the intestines of humans and other animals. Some species of *E. coli* are a major cause of diarrheal disease among children in low-income countries [49] whereas other species like uropathogenic *E. coli* is a leading cause of urinary tract infection in humans [50]. The type 1 pili of *E. coli* consists of FimH adhesion which can mediate the invasion of urothelial cells through the multivalent interaction of mannose groups present on cell surfaces [51]. Mannose receptor prepared on the electrode surface is excellent at mimicking the cell surface and can be used to detect the *E. coli* in serum samples. Guo and coworkers developed mannose-terminated SAMs to specifically and selectively detect *E. coli* ORN 178 that doesn't show any increase in  $R_{ct}$  with another subset *E. coli* ORN 208. The model shows the linear relationship between  $R_{ct}$  and the logarithmic value of *E. coli* concentration from  $10^2$  to  $10^3$  CFU/mL, with the limit of detection of around 100 CFU/mL [25].

On the other hand, lipopolysaccharides (LPS) of the *E. coli* can also be targeted by the Con A receptor for its detection. da Silva and coworkers used polyaniline immobilized Con A for the EIS-based detection of *E. coli* targeting LPS and *Staphylococcus aureus* targeting lipoteichoic acid present on the surface of the bacteria [52]. The maximum value of  $R_{ct}$  for *E. coli* was found to be 4.40 kΩ and that for *S. aureus* was found to be 17.80 kΩ. In the another similar study, Con A was immobilized on the screen printed gold electrode for detecting *E. coli*, the  $R_{ct}$  was found to vary linearly with the logarithmic value of *E. coli* concentration from  $5.0 \times 10^3$  to  $5.0 \times 10^7$  CFU/mL.

### 2. Cancer Cell

Lectin immobilized on the electrode surface can be used as a cytosensor to detect cancer cells, which has important applications in cancer therapeutics and diagnosis. Hu and coworkers used Con A modified gold disk electrode to detect cancer cells from the sample using EIS [13]. They successfully detected human liver cancer cell Bel-7404 with a detection limit of 234 cells/mL, and recovery percentage ranging from 97.14% to 100.13%. An impedance

cytosensor was also applied to detect circulating tumor cells monocytic leukemic cells (THP-1) and myeloblastic leukemic cells (OCI-AMI3) based on Jacalin lectin receptor immobilized on ITO surface. This cytosensor is capable of differentiating leukemic cells from healthy monocyte cells with a limit of detection  $4 \pm 1$  cells/mL for THP-1 and  $3 \pm 1$  cells/mL for OCI-AMI3 [45].

### 3. Biomarkers

Aberration in protein glycosylation is found to be associated with cancer and other autoimmune diseases [47]. Early detection of such aberration can help treat disease at an early stage, which can drastically increase the chances of recovery of the patient. Biomarkers are found in the disease response mostly as an aberration of glycans and can be detected using biosensors. The challenge, however, is the ability to detect a very small amount of biomarker present in bodily fluids like serum, urine, saliva etc. Typical detection limits of label-free biosensing techniques like surface plasmon resonance (SPR) and quartz crystal microbalance (QCM) ranges from the micromolar to the nanomolar region, whereas EIS sensitivity can reach down to attomolar [27, 53].

Sialic acid present in glycoproteins is one of the important saccharides that are found to be affected early by the response of disease in the body. Sialic acid specific lectin such as SNA can, therefore, be used as a receptor for the capture and analysis of sialoglycoproteins. Proteins like fetuin containing 8.7% of sialic acid and asialofetuin containing 0.5% of sialic acid can be used as a model analyte for studying the effectiveness of the biosensor [27]. Figure 4A shows the response of the SNA lectin immobilized on 2D (planar gold surface) and the 3D (20 nm Au nanoparticles immobilized on the planar gold surface) electrode for 1fM and 10 aM fetuin, respectively. Figure 4B is a comparison of calibration curves for the 2D and the 3D lectin biosensor towards fetuin (FET) and asialofetuin (ASF) [54]. Tkac's group used SNA-based lectin receptor to discriminate antibody isolated from a patient with rheumatoid arthritis (RA) from that of healthy individuals [35]. It has been observed that EIS signal is higher for the healthy individual compared to the patient with RA, proving decreased amount of sialic acid in the glycan region of the antibody.

Alpha-fetoprotein (AFP) is a US FDA approved biomarker for hepatocellular carcinoma [41]. Yang and coworkers employed lectin wheat-germ agglutinin (WGA) immobilized on SWCNTs as a receptor for the

sensitive determination and discrimination of AFP [36]. With the detection of AFP by WGA, the charge transfer resistance increases linearly in the range from 1 to 100 ng/L and a detection limit of 0.1 ng/L. SWNTs were used to reduce the background enhancing the EIS response.

Using EIS, it is also possible to discriminate the serum glycoproteins of patients with dengue fever from those of healthy persons. By simply modifying the gold electrodes with gold nanoparticles, Con A, polyvinyl butyral, and bovine serum albumin, glycoproteins from the patients with dengue fever can be discriminated by monitoring the change in  $R_{ct}$  [46]. It is found that the  $R_{ct}$  value increases to 5.10 k $\Omega$  from 1.43 k $\Omega$  for blank sample and 2.09 for the control sample. Later, Luna and coworkers modified the gold electrode with 1,2-dipalmitoyl-sn-glycero-3-phosphocholine and Con A to study glycoproteins from the serum of patients infected with dengue serotypes 1, 2 and 3 [48]. The prepared biosystem was found to show the increased resistance with all the serotypes, but a relatively higher response was obtained for glycoproteins present in dengue serotype 3.

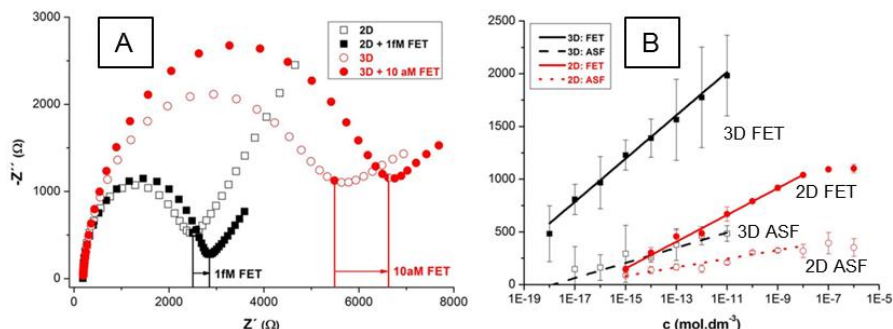


Figure 4. (A) Comparison of the response of the 2D (planar gold surface) and the 3D (20 nm Au nanoparticles immobilized on planar gold surface) biosensor to its analyte fetuin (FET) with concentration close to the detection limit, represented in a Nyquist plot and (B). Comparison of calibration curves for the 2D and the 3D lectin biosensor towards its two analytes – glycoproteins fetuin (FET) and asialofetuin (ASF).

Reprinted with permission from reference [54]. Copyright 2015 ESG.

#### 4. Binding Constant Determination

For the research and development of drugs and vaccines, it is important to know the binding constant between carbohydrates and proteins. It has been found that equilibrium dissociation constant ( $K_d$ ) for carbohydrate–protein

interactions are generally considered to be in the micromolar to millimolar range [55]. EIS can be used to determine real  $K_d$  of carbohydrate-protein interactions, as it is affected by many environmental factors. It has been found that such interactions are weak in solution compared to on the solid support [56]. Isothermal titration calorimetry (ITC) has been utilized to examine the binding affinity of Con A to a series mono-, di- and tri-mannosides in solution [57]. The binding affinity was found to be highest for the O-methylated  $\alpha(1-3,1-6)$  trimannoside with  $K_d = 2.0 \mu\text{M}$  slightly higher than  $K_d$  of free trimannoside  $3.0 \mu\text{M}$ . Our group used EIS to determine the  $K_d$  of Con A interaction with mono-, di- and tri-mannosides immobilized on the gold wire [31]. Man-C<sub>8</sub>-SH, Man(1-3)Man-C<sub>8</sub>-SH, and Man(1-4,1-6)Man-C<sub>8</sub>-SH show the comparable  $K_d$  of  $70 \pm 19$ ,  $75 \pm 20$  and  $81 \pm 31 \text{ nM}$ , respectively, similar to that reported for similar interaction when performed on the solid support using SPR and QCM [58-59]. However, Man(1-6)Man-C<sub>8</sub>-SH and Man(1-3,1-6)Man-C<sub>8</sub>-SH showed stronger binding with  $K_d = 14 \pm 4$  and  $30 \pm 5 \text{ nM}$ , respectively. The stronger interaction of surface bound mannoses and Con A compared to that of the solution is due to the multivalent interactions [60]. Multivalent interactions are possible when the distance between the immobilized mannoses are optimal for capturing Con A.

## COMPARISON OF EIS WITH OTHER TECHNIQUES

There is a wide variety of other techniques used for the study of carbohydrate–protein interactions. All of these techniques have their own advantages and disadvantages. Most of the techniques developed so far have to be supported by the supplementary technique. The carbohydrate–protein interactions can be studied either in a solution or on a solid substrate. Enzyme-linked lectin assays (ELLA) and isothermal titration microcalorimetry (ITC) are the method of choice to study these types of interactions in the solution. However, with the advancement of nanotechnology other sensitive methods are developed for studying such interactions. Among many techniques, label-free techniques, such as surface plasmon resonance, quartz-crystal microbalance and electrochemical impedance spectroscopy have shown clear advantages, as the interaction can be studied without labeling the molecules with dyes or radioactive materials, which themselves can interfere in the interaction. In this part of the chapter, we will discuss and compare these techniques with EIS for studying carbohydrate–protein interactions, Table 3.

**Table 2. Limit of detection (LOD) and linearity range determined by EIS for some carbohydrate–protein interactions**

Electrode	Interaction (Receptor–Analyte)	LOD	Linearity	Ref
ITO	Mannose–Con A	0.12 nM	3–15 nM	[28]
SPCEs-AuNp	Glucose–Con A	0.099 pmol	2.2–40.0 µg/mL	[61]
	Mannose–Con A	0.078 pmol		
Au wire	Mannose–Con A	4 nM	1–50 nM	[31]
Au disk	ConA–cancer cell (Bel-7404)	234 cells/mL	n/a	[13]
ITO	Jacalin–leukemic cells (THP-1)	4 ± 1 cells/mL	n/a	[45]
	Jacalin–leukemic cells (OCI-AMI3)	3 ± 1 cells/mL		
Au disk	Mannose– <i>E. coli</i> (ORN 178)	10 <sup>2</sup> CFU/mL	10 <sup>2</sup> –10 <sup>3</sup> CFU/mL	[25]
Au electrode	Con A– <i>E. coli</i> (DH5)	75 cells/mL	10 <sup>2</sup> –10 <sup>5</sup> cells/mL	[40]
Au/SPE	Con A– <i>E. coli</i> (CECT 515)	5.0 × 10 <sup>3</sup> CFU/mL	10 <sup>3</sup> –10 <sup>7</sup> CFU/mL	[62]
Cu/Ni/Au PCB	PNA–TF-antigen	1 pg/mL (13 fM)	n/a	[63]
	PNA–asialofetuin	10 pg/mL (150 fM)		
	SNA–fetuin	10 pg/mL (150 fM)		
Au chip	SNA–IgG	3.2 nM	n/a	[35]
	SNA–fetuin	3.5 µg/mL (73 pM)		
	SNA–asialofetuin	1.3 µg/mL (2.7nM)		
Au	SNA–fetuin	0.33 fM	n/a	[53]
	SNA–asialofetuin	0.54 fM		
Au	Con A–transferrin	≈1 pM	n/a	[64]
	Con A–invertase	≈1 fM		
	SNA–fetuin	≈100 fM		
	SNA–asialofetuin	≈1 pM		
	RCA–fetuin	130 fm		
	RCA–asialofetuin	10 fm		
SWNTs-SPCE	WGA–α-fetoprotein	0.1 ng/L	1–100 ng/L	[36]
Au	Con A–serum glycoproteins from patients infected by dengue fever	80 fold dilution	10–80 fold dilution	[46]
Si–Au array	SNA–fetuin/BXPC-3	1 pg/mL	1 pg/ml–10 ng/mL	[65]
Au/SPE	SNA–I–transferrin	20 ng	10–70 ng	[47]

**ITO:** indium tin oxide, **SWNT:** single-wall carbon nanotubes, **SPCE:** screen-printed carbon electrode, **PCB:** printed circuit board, **BXPC-3:** protein extracts from a cultured human pancreatic cancer cell line, **Au/SPE:** screen-printed gold electrode

**Table 3. Carbohydrate–protein interaction studies using other common techniques.**

Techniques	Substrate	Interactions (receptor-analyte)	LOD	Linear range ( $\mu\text{g}/\text{mL}$ )	Ref
Colorimetric	Au nanoparticles	Maltose–Con A	80 nM	n/a	[82]
		Mannose–Con A	$\approx$ 100 nM	n/a	[67]
		Galactose–RCA <sub>120</sub>	9 nM	n/a	[83]
SPR	Au film	WGA– <i>E. coli</i> (O157:H7)	$3 \times 10^3$ CFU/mL	n/a	[71]
		Sialosides–SNA	$\approx$ 50 nM	10–100 $\mu\text{g}/\text{mL}$	[72]
QCM	Au on quartz crystal	Mannose+Con A– <i>E. coli</i> (W1485)	$7.5 \times 10^2$ cells/mL	$7.5 \times 10^2$ – $7.5 \times 10^7$ cells/mL	[77]
		Mannose– <i>E. coli</i> (W1485)	$3.0 \times 10^7$ cells/mL	$2.9 \times 10^7$ – $2.7 \times 10^8$ cells/mL	
		Con A– <i>C. jejuni</i>	$10^3$ cells	$10^3$ – $10^4$ cells	[78]
Field-effect transistor	Si nanowires	Galactose–lectin from <i>E. cristagalli</i>	0.1 pg/mL	n/a	[79]
Anodic stripping	Au electrode	Mannose–Con A	0.070 $\mu\text{g}/\text{mL}$	0.084–50.0 $\mu\text{g}/\text{mL}$	[81]

## Colorimetry

Colorimetry is one of the early adopted quantitative techniques for rapid detection of carbohydrate–protein interactions [66]. This technique is based on nanoparticles, where the signal in the form of color change is obtained due to aggregation of nanoparticles caused by the interaction of lectins with the carbohydrate functionalized nanoparticles [67]. The degree of aggregation is directly proportional to the concentration of the lectin. Kataoka and co-workers have shown the quantitative and reversible interaction of lectin *R. communis* agglutinin (RCA<sub>120</sub>) with lactose immobilized on gold nanoparticles under physiologically relevant conditions [66]. The color of the solution changes from red to purple when there is an interaction between lactose and RCA<sub>120</sub>, which then changes back to red when galactose is introduced to reverse the interaction. Unlike the electrodes used in EIS technique, the selectivity and sensitivity of the colorimetric technique can be easily reduced due to the possibility of nanoparticles to aggregate in a high ionic concentration of the solution.

## Surface Plasmon Resonance

Surface plasmon resonance (SPR) is the most commonly used optical technique for studying affinity-based interactions, such as carbohydrate–protein interactions, protein–protein interactions, enzyme–substrate interactions and DNA hybridization [68]. When an electromagnetic wave incidents on the surface of a thin Au film ( $\approx 50$  nm), plasmons propagate along  $x$ - and  $y$ -axes producing evanescent waves along the  $z$ -axis [69]. Any changes in refractive index near/on the interface of the gold surface cause interference with the evanescent waves, which is directly proportional to the concentration of biomolecules [70]. This property can be utilized for studying carbohydrate–protein interaction using SPR technique. Wang and coworkers used SPR for rapid detection of *E. coli* (O157:H7) using five different types of lectins [71]. They obtained the better response when lectin WGA was used as a receptor with the limit of detection of  $3 \times 10^3$  CFU/mL. They further test the real food sample for the possibility of *E. coli* highlighting the sensitivity, reliability and effectiveness of detection. In another study, SPR is used to study the specificity and sensitivity of four different types of lectin toward  $\alpha$ 2,6-linked sialosides receptor [72]. It was found that lectin SNA binds strongly to the  $\alpha$ 2,6-linked sialosides compared to MAL, Con A and WGA, with SPR showing linear relationship ranging from 10–100  $\mu$ g/mL and limit of detection down to 50 nM. It was also found that any alteration in sialyl linkage and terminal sialic acid structure greatly changes the binding affinity to SNA. SPR, however, is mainly used in finding the binding affinity between biomolecules than detecting the small analytes as in EIS.

SPR is closely related to other plasmonic techniques such as localized surface plasmon resonance (LSPR) and surface enhanced Raman spectroscopy (SERS), which are also frequently used for studying such interactions [73].

## Quartz-Crystal Microbalance

Quartz-crystal microbalance (QCM) is another popular label-free technique with the possibility of real-time monitoring of biomolecules interactions and its sensitivity can go down to  $\text{ng/cm}^2$  [74]. QCM detects changes in the electromechanical properties of an oscillating piezoelectric quartz-crystal sensor [75]. The frequency shift ( $\Delta f$ ) due to the immobilization of biomolecules is related to the mass change at the surface of the crystal, and

hence can be utilized for the *in situ* real-time monitoring of carbohydrate–protein interactions [76]. Shen and coworkers used SAMs of mannose in combination with lectin Con A to detect *E. coli* W1485 through the strong multivalent interactions [77]. The cell wall of the *E. coli* W1485 contains lipopolysaccharides having O-antigen which favors the interaction with the immobilized Con A, and as the bacteria approaches closer to the QCM surface type 1 fimbriae present on cell walls specifically interact strongly with mannose. In this way, the QCM sensor was used for detection of *E. coli* as low as  $7.5 \times 10^2$  cells/mL which otherwise with mannose alone is  $3.0 \times 10^7$  cells/mL with the linear response  $7.5 \times 10^2$ – $7.5 \times 10^7$ . Other foodborne pathogenic enterobacteria, such as *Campylobacter jejuni* (*C. jejuni*), *Helicobacter pylori* (*H. pylori*) can also be detected using QCM based on lectin receptor [78].

## Other Methods

Although EIS, SPR and QCM are the commonly used techniques for studying carbohydrate–protein interactions, there are other methods like field-effect transistor (FET) and anodic stripping voltammetry, which are found to be as effective as EIS, SPR and QCM.

FET is biosensing technique based on change in electric conductance of transistor due to binding of biomolecules. Silicon nanowire (SiNW)-based FET biosensor can detect lectin from *Erythrina cristagalli* to as low as 100 fg/mL by using galactose as a receptor [79]. In another study, single-walled carbon nanotube FET was used to detect lectin from *Pseudomonas aeruginosa* using glycosylated FET surface. The sensor can detect lectin as low as 2 nM, and the dissociation constant of the interaction was found to be 6.8  $\mu\text{M}$  [80]. Anodic stripping voltammetry was also used for detecting as low as 0.070  $\mu\text{g}/\text{mL}$  of lectin Con A using carbohydrate-stabilized gold nanoparticles and silver-enhancement reaction, which shows the linear response for Con A concentration from 0.084  $\mu\text{g}/\text{mL}$  to 50.0  $\mu\text{g}/\text{mL}$  [81].

## CONCLUSION

The development and use of EIS for biosensing experiments are on the rise because of simplicity and sensitivity of the technique. Efforts have been made to use the same electrode for EIS and other suitable techniques. Our

group has studied the mannose-con A interactions using EIS and LSPR technique on the LSPR-active nanostructured gold surface [84]. Lazar and co-workers were able to simultaneous run EIS and LSPR experiments to study glycopolymers lectin binding affinity [85].

Since EIS is a very sensitive technique, it is also challenging to obtain a reproducible data and has a higher possibility of introducing false positive and negative values. The measurement should be performed in sets by providing the exact conditions from electrode cleaning to final readout. Change in even a small condition may give a totally different reading. The results from EIS should always be backed by performing control experiments and if possible with other suitable techniques. In this chapter, we discussed some of the recent advances and use of EIS technique and compared it with other commonly used techniques for studying carbohydrate–protein interactions.

## ACKNOWLEDGEMENTS

The authors acknowledge the recent support of the work in this area by the University of Missouri–St. Louis and by the NIGMS awards R01-GM090254 and R01-GM111835.

## REFERENCES

- [1] Varki, A., Glycan-based interactions involving vertebrate sialic-acid-recognizing proteins. *Nature* 2007, *446* (7139), 1023-1029.
- [2] Stencel-Baerenwald, J. E.; Reiss, K.; Reiter, D. M.; Stehle, T.; Dermody, T. S., The sweet spot: defining virus-sialic acid interactions. *Nat. Rev. Micro.* 2014, *12* (11), 739-749.
- [3] Biswas, S.; Medina, S. H.; Barchi, J. J., Jr., Synthesis and cell-selective antitumor properties of amino acid conjugated tumor-associated carbohydrate antigen-coated gold nanoparticles. *Carbohydr. Res.* 2015, *405*, 93-101.
- [4] Arnaiz, B.; Martinez-Avila, O.; Falcon-Perez, J. M.; Penades, S., Cellular uptake of gold nanoparticles bearing HIV gp120 oligomannosides. *Bioconjugate Chem.* 2012, *23* (4), 814-25.

- [5] Aussedat, B.; Vohra, Y.; Park, P. K.; Fernández-Tejada, A.; Alam, S. M.; Dennison, S. M.; Jaeger, F. H.; Anasti, K.; Stewart, S.; Blinn, J. H., Chemical synthesis of highly congested gp120 V1V2 N-glycopeptide antigens for potential HIV-1-directed vaccines. *J. Am. Chem. Soc.* 2013, *135* (35), 13113-13120.
- [6] Zhang, X.; Teng, Y.; Fu, Y.; Xu, L.; Zhang, S.; He, B.; Wang, C.; Zhang, W., Lectin-based biosensor strategy for electrochemical assay of glycan expression on living cancer cells. *Anal. Chem.* 2010, *82* (22), 9455-9460.
- [7] Disney, M. D.; Zheng, J.; Swager, T. M.; Seeberger, P. H., Detection of bacteria with carbohydrate-functionalized fluorescent polymers. *J. Am. Chem. Soc.* 2004, *126* (41), 13343-13346.
- [8] Kikkeri, R.; Kamena, F.; Gupta, T.; Hossain, L. H.; Boonyaratpalakalin, S.; Gorodyska, G.; Beurer, E.; Coullerez, G.; Textor, M.; Seeberger, P. H., Ru(II) glycodendrimers as probes to study lectin–carbohydrate interactions and electrochemically measure monosaccharide and oligosaccharide concentrations. *Langmuir* 2010, *26* (3), 1520-1523.
- [9] Ding, L.; Ji, Q.; Qian, R.; Cheng, W.; Ju, H., Lectin-based nanoprobe functionalized with enzyme for highly sensitive electrochemical monitoring of dynamic carbohydrate expression on living cells. *Anal. Chem.* 2010, *82* (4), 1292-1298.
- [10] Zhang, J.-J.; Cheng, F.-F.; Zheng, T.-T.; Zhu, J.-J., Design and implementation of electrochemical cytosensor for evaluation of cell surface carbohydrate and glycoprotein. *Anal. Chem.* 2010, *82* (9), 3547-3555.
- [11] del Carmen Fernández-Alonso, M.; Díaz, D.; Alvaro Berbis, M.; Marcelo, F.; Jimenez-Barbero, J., Protein-carbohydrate interactions studied by NMR: from molecular recognition to drug design. *Curr. Protein Pept. Sci.* 2012, *13* (8), 816-830.
- [12] Li, X.; Martin, S. J.; Chinoy, Z. S.; Liu, L.; Rittgers, B.; Dluhy, R. A.; Boons, G. J., Label-free detection of glycan–protein interactions for array development by surface-enhanced Raman spectroscopy (SERS). *Chem. Eur. J.* 2016, *22* (32), 11180-11185.
- [13] Hu, Y.; Zuo, P.; Ye, B. C., Label-free electrochemical impedance spectroscopy biosensor for direct detection of cancer cells based on the interaction between carbohydrate and lectin. *Biosens. Bioelectron.* 2013, *43*, 79-83.

- [14] Pei, Y.; Yu, H.; Pei, Z.; Theurer, M.; Ammer, C.; André, S.; Gabius, H.-J.; Yan, M.; Ramström, O., Photoderivatized polymer thin films at quartz crystal microbalance surfaces: sensors for carbohydrate– protein interactions. *Anal. Chem.* 2007, 79 (18), 6897-6902.
- [15] Bard, A. J.; Faulkner, L. R., *Electrochemical methods: Fundamentals and applications*. New York: 2001.
- [16] Macdonald, D. D., Reflections on the history of electrochemical impedance spectroscopy. *Electrochim. Acta* 2006, 51 (8), 1376-1388.
- [17] Macdonald, J. R., Impedance spectroscopy. *Ann. Biomed. Eng.* 1992, 20 (3), 289-305.
- [18] Jüttner, K., Electrochemical impedance spectroscopy (EIS) of corrosion processes on inhomogeneous surfaces. *Electrochim. Acta* 1990, 35 (10), 1501-1508.
- [19] Adachi, M.; Sakamoto, M.; Jiu, J.; Ogata, Y.; Isoda, S., Determination of parameters of electron transport in dye-sensitized solar cells using electrochemical impedance spectroscopy. *J. Phys. Chem. B* 2006, 110 (28), 13872-13880.
- [20] Ruan, C.; Yang, L.; Li, Y., Immunobiosensor chips for detection of Escherichia coli O157: H7 using electrochemical impedance spectroscopy. *Anal. Chem.* 2002, 74 (18), 4814-4820.
- [21] Retter, U.; Lohse, H., Electrochemical impedance spectroscopy. In *Electroanalytical Methods*, Springer: 2002; pp 149-166.
- [22] Barsoukov, E.; Macdonald, J. R., *Impedance spectroscopy: theory, experiment, and applications*. John Wiley & Sons: 2005.
- [23] Xu, D.; Xu, D.; Yu, X.; Liu, Z.; He, W.; Ma, Z., Label-free electrochemical detection for aptamer-based array electrodes. *Anal. Chem.* 2005, 77 (16), 5107-5113.
- [24] Chen, X.; Wang, Y.; Zhou, J.; Yan, W.; Li, X.; Zhu, J.-J., Electrochemical impedance immunosensor based on three-dimensionally ordered macroporous gold film. *Anal. Chem.* 2008, 80 (6), 2133-2140.
- [25] Guo, X.; Kulkarni, A.; Doepke, A.; Halsall, H. B.; Iyer, S.; Heineman, W. R., Carbohydrate-based label-free detection of Escherichia coli ORN 178 using electrochemical impedance spectroscopy. *Anal. Chem.* 2012, 84 (1), 241-6.

- [26] Wang, S.; Li, L.; Jin, H.; Yang, T.; Bao, W.; Huang, S.; Wang, J., Electrochemical detection of hepatitis B and papilloma virus DNAs using SWCNT array coated with gold nanoparticles. *Biosens. Bioelectron.* 2013, *41*, 205-210.
- [27] Bertok, T.; Sediva, A.; Katrlik, J.; Gemeiner, P.; Mikula, M.; Nosko, M.; Tkac, J., Label-free detection of glycoproteins by the lectin biosensor down to attomolar level using gold nanoparticles. *Talanta* 2013, *108*, 11-18.
- [28] Wang, Z.; Sun, C.; Vigesna, G.; Liu, H.; Liu, Y.; Li, J.; Zeng, X., Glycosylated aniline polymer sensor: Amine to imine conversion on protein-carbohydrate binding. *Biosens. Bioelectron.* 2013, *46*, 183-189.
- [29] Shah, A. K.; Hill, M. M.; Shiddiky, M. J. A.; Trau, M., Electrochemical detection of glycan and protein epitopes of glycoproteins in serum. *Analyst* 2014, *139* (22), 5970-5976.
- [30] Chang, B.-Y.; Park, S.-M., Electrochemical impedance spectroscopy. *Annu. Rev. Anal. Chem.* 2010, *3*, 207-229.
- [31] Bhattarai, J. K.; Tan, Y. H.; Pandey, B.; Fujikawa, K.; Demchenko, A. V.; Stine, K. J., Electrochemical impedance spectroscopy study of Concanavalin A binding to self-assembled monolayers of mannosides on gold wire electrodes. *J. Electroanal. Chem.* 2016, *780*, 311-320.
- [32] Oliveira, M. D. L.; Correia, M. T. S.; Coelho, L. C. B. B.; Diniz, F. B., Electrochemical evaluation of lectin-sugar interaction on gold electrode modified with colloidal gold and polyvinyl butyral. *Colloids Surf. B* 2008, *66* (1), 13-19.
- [33] Daniels, J. S.; Pourmand, N., Label-free impedance biosensors: opportunities and challenges. *Electroanalysis* 2007, *19* (12), 1239-1257.
- [34] Pihíková, D.; Kasák, P.; Tkac, J., Glycoprofiling of cancer biomarkers: Label-free electrochemical lectin-based biosensors. *Open Chem.* 2015, *13* (1).
- [35] Bertok, T.; Šedivá, A.; Filip, J.; Ilcikova, M.; Kasak, P.; Velic, D.; Jane, E.; Mravcová, M.; Rovenský, J.; Kunzo, P.; Lobotka, P.; Šmatko, V.; Vikartovská, A.; Tkac, J., Carboxybetaine modified interface for electrochemical glycoprofiling of antibodies isolated from human serum. *Langmuir* 2015, *31* (25), 7148-7157.
- [36] Yang, H.; Li, Z.; Wei, X.; Huang, R.; Qi, H.; Gao, Q.; Li, C.; Zhang, C., Detection and discrimination of alpha-fetoprotein with a label-free electrochemical impedance spectroscopy biosensor array based on lectin functionalized carbon nanotubes. *Talanta* 2013, *111*, 62-8.

- [37] Bogomolova, A.; Komarova, E.; Reber, K.; Gerasimov, T.; Yavuz, O.; Bhatt, S.; Aldissi, M., Challenges of electrochemical impedance spectroscopy in protein biosensing. *Anal. Chem.* 2009, 81 (10), 3944-3949.
- [38] Vogt, S.; Su, Q.; Gutierrez-Sanchez, C.; Noll, G., Critical view on electrochemical impedance spectroscopy using the ferri/ferrocyanide redox couple at gold electrodes. *Anal. Chem.* 2016, 88 (8), 4383-90.
- [39] Stine, K. J., *Carbohydrate nanotechnology*. John Wiley & Sons: 2015.
- [40] Yang, H.; Zhou, H.; Hao, H.; Gong, Q.; Nie, K., Detection of Escherichia coli with a label-free impedimetric biosensor based on lectin functionalized mixed self-assembled monolayer. *Sens. Actuators B: Chem.* 2016, 229, 297-304.
- [41] Badr, H. A.; AlSadek, D. M.; Darwish, A. A.; ElSayed, A. I.; Bekmanov, B. O.; Khussainova, E. M.; Zhang, X.; Cho, W. C.; Djansugurova, L. B.; Li, C.-Z., Lectin approaches for glycoproteomics in FDA-approved cancer biomarkers. *Expert Rev. Proteomics* 2014, 11 (2), 227-236.
- [42] Gutman, S.; Kessler, L. G., The US Food and Drug Administration perspective on cancer biomarker development. *Nat. Rev. Cancer.* 2006, 6 (7), 565-571.
- [43] Kim, E. H.; Misek, D. E., Glycoproteomics-based identification of cancer biomarkers. *Int. J. Proteomics* 2011, 2011, 10.
- [44] Pihíková, D.; Kasák, P.; Tkac, J., Glycoprofiling of cancer biomarkers: Label-free electrochemical lectin-based biosensors. *Open Chem.* 2015, 13 (1), 636-655.
- [45] Cancino-Bernardi, J.; Marangoni, V. S.; Faria, H. A. M.; Zucolotto, V., Detection of leukemic cells by using Jacalin as the biorecognition layer: A new strategy for the detection of circulating tumor cells. *ChemElectroChem* 2015, 2 (7), 963-969.
- [46] Oliveira, M. D. L.; Correia, M. T. S.; Diniz, F. B., A novel approach to classify serum glycoproteins from patients infected by dengue using electrochemical impedance spectroscopy analysis. *Synth. Met.* 2009, 159 (21–22), 2162-2164.
- [47] Silva, M. L.; Gutierrez, E.; Rodriguez, J. A.; Gomes, C.; David, L., Construction and validation of a *Sambucus nigra* biosensor for cancer-associated STn antigen. *Biosens. Bioelectron.* 2014, 57, 254-61.

- [48] Luna, D. M.; Oliveira, M. D.; Nogueira, M. L.; Andrade, C. A., Biosensor based on lectin and lipid membranes for detection of serum glycoproteins in infected patients with dengue. *Chem. Phys. Lipids* 2014, **180**, 7-14.
- [49] Kaper, J. B.; Nataro, J. P.; Mobley, H. L., Pathogenic Escherichia coli. *Nat. Rev. Microbiol.* 2004, **2** (2), 123-140.
- [50] Marrs, C. F.; Zhang, L.; Foxman, B., Escherichia coli mediated urinary tract infections: Are there distinct uropathogenic E. coli (UPEC) pathotypes? *FEMS Microbiol. Lett.* 2005, **252** (2), 183-190.
- [51] Martinez, J. J.; Mulvey, M. A.; Schilling, J. D.; Pinkner, J. S.; Hultgren, S. J., Type 1 pilus-mediated bacterial invasion of bladder epithelial cells. *EMBO J.* 2000, **19** (12), 2803-2812.
- [52] da Silva, J. S. L.; Oliveira, M. D. L.; de Melo, C. P.; Andrade, C. A. S., Impedimetric sensor of bacterial toxins based on mixed (Concanavalin A)/polyaniline films. *Colloids Surf. B* 2014, **117**, 549-554.
- [53] Bertok, T.; Gemeiner, P.; Mikula, M.; Gemeiner, P.; Tkac, J., Ultrasensitive impedimetric lectin based biosensor for glycoproteins containing sialic acid. *Microchim. Acta* 2013, **180** (1-2), 151-159.
- [54] Bertok, T.; Sediva, A.; Vikartovska, A.; Tkac, J., Comparison of the 2D and 3D nanostructured lectin-based biosensors for in situ detection of sialic acid on glycoproteins. *Int. J. Electrochem. Sci.* 2014, **9**, 890-900.
- [55] Bewley, C. A.; Shahzad-ul-Hussan, S., Characterizing carbohydrate-protein interactions by NMR. *Biopolymers* 2013, **99** (10), 10.1002/bip. 22329.
- [56] Dam, T. K.; Brewer, C. F., Thermodynamic studies of lectin-carbohydrate interactions by isothermal titration calorimetry. *Chem. Rev.* 2002, **102** (2), 387-430.
- [57] Mandal, D. K.; Kishore, N.; Brewer, C. F., Thermodynamics of lectin-carbohydrate interactions. Titration microcalorimetry measurements of the binding of N-linked carbohydrates and ovalbumin to concanavalin A. *Biochemistry* 1994, **33** (5), 1149-1156.
- [58] Schlick, K. H.; Cloninger, M. J., Inhibition binding studies of glycopolymers/lectin interactions using surface plasmon resonance. *Tetrahedron* 2010, **66** (29), 5305-5310.
- [59] Mori, T.; Toyoda, M.; Ohtsuka, T.; Okahata, Y., Kinetic analyses for bindings of concanavalin A to dispersed and condensed mannose surfaces on a quartz crystal microbalance. *Anal. Biochem.* 2009, **395** (2), 211-216.

- [60] Halkes, K. M.; Carvalho De Souza, A.; Maljaars, C. E. P.; Gerwig, G. J.; Kamerling, J. P., A facile method for the preparation of gold glyconanoparticles from free oligosaccharides and their applicability in carbohydrate-protein interactionstudies. *Eur. J. Org. Chem.* 2005, (17), 3650-3659.
- [61] Loaiza, O. A.; Lamas-Ardisana, P. J.; Jubete, E.; Ochoteco, E.; Loinaz, I.; Cabanero, G.; Garcia, I.; Penades, S., Nanostructured disposable impedimetric sensors as tools for specific biomolecular interactions: sensitive recognition of concanavalin A. *Anal. Chem.* 2011, 83 (8), 2987-95.
- [62] Gamella, M.; Campuzano, S.; Parrado, C.; Reviejo, A. J.; Pingarrón, J. M., Microorganisms recognition and quantification by lectin adsorptive affinity impedance. *Talanta* 2009, 78 (4–5), 1303-1309.
- [63] La Belle, J. T.; Gerlach, J. Q.; Svarovsky, S.; Joshi, L., Label-free impedimetric detection of glycan–lectin interactions. *Anal. Chem.* 2007, 79 (18), 6959-6964.
- [64] Bertok, T.; Klukova, L.; Sediva, A.; Kasák, P.; Semak, V.; Micusik, M.; Omastova, M.; Chovanová, L.; Vlček, M.; Imrich, R., Ultrasensitive impedimetric lectin biosensors with efficient antifouling properties applied in glycoprofiling of human serum samples. *Anal. Chem.* 2013, 85 (15), 7324-7332.
- [65] Nagaraj, V. J.; Aithal, S.; Eaton, S.; Bothara, M.; Wiktor, P.; Prasad, S., NanoMonitor: a miniature electronic biosensor for glycan biomarker detection. *Nanomedicine (Lond)* 2010, 5 (3), 369-78.
- [66] Otsuka, H.; Akiyama, Y.; Nagasaki, Y.; Kataoka, K., Quantitative and reversible lectin-induced association of gold nanoparticles modified with  $\alpha$ -lactosyl- $\omega$ -mercapto-poly (ethylene glycol). *J. Am. Chem. Soc.* 2001, 123 (34), 8226-8230.
- [67] Hone, D. C.; Haines, A. H.; Russell, D. A., Rapid, quantitative colorimetric detection of a lectin using mannose-stabilized gold nanoparticles. *Langmuir* 2003, 19 (17), 7141-7144.
- [68] Homola, J., Present and future of surface plasmon resonance biosensors. *Anal. Bioanal. Chem.* 2003, 377 (3), 528-539.
- [69] Homola, J.; Yee, S. S.; Gauglitz, G., Surface plasmon resonance sensors: review. *Sens. Actuators B: Chem.* 1999, 54 (1), 3-15.
- [70] Piliarik, M.; Vaisocherová, H.; Homola, J., Surface plasmon resonance biosensing. *Biosens. Biodec.* 2009, 65-88.

- [71] Wang, Y.; Ye, Z.; Si, C.; Ying, Y., Monitoring of Escherichia coli O157:H7 in food samples using lectin based surface plasmon resonance biosensor. *Food Chem.* 2013, *136* (3–4), 1303-1308.
- [72] Linman, M. J.; Taylor, J. D.; Yu, H.; Chen, X.; Cheng, Q., Surface plasmon resonance study of protein–carbohydrate interactions using biotinylated sialosides. *Anal. Chem.* 2008, *80* (11), 4007-4013.
- [73] Anker, J. N.; Hall, W. P.; Lyandres, O.; Shah, N. C.; Zhao, J.; Van Duyne, R. P., Biosensing with plasmonic nanosensors. *Nat. Mater.* 2008, *7* (6), 442-453.
- [74] Bouchet-Spinelli, A.; Reuillard, B.; Coche-Guerente, L.; Armand, S.; Labbe, P.; Fort, S., Oligosaccharide biosensor for direct monitoring of enzymatic activities using QCM-D. *Biosens. Bioelectron.* 2013, *49*, 290-6.
- [75] Fredriksson, C.; Kihlman, S.; Rodahl, M.; Kasemo, B., The piezoelectric quartz crystal mass and dissipation sensor: a means of studying cell adhesion. *Langmuir* 1998, *14* (2), 248-251.
- [76] Pei, Z.; Anderson, H.; Aastrup, T.; Ramström, O., Study of real-time lectin–carbohydrate interactions on the surface of a quartz crystal microbalance. *Biosens. Bioelectron.* 2005, *21* (1), 60-66.
- [77] Shen, Z.; Huang, M.; Xiao, C.; Zhang, Y.; Zeng, X.; Wang, P. G., Nonlabeled quartz crystal microbalance biosensor for bacterial detection using carbohydrate and lectin recognitions. *Anal. Chem.* 2007, *79* (6), 2312-9.
- [78] Safina, G.; van Lier, M.; Danielsson, B., Flow-injection assay of the pathogenic bacteria using lectin-based quartz crystal microbalance biosensor. *Talanta* 2008, *77* (2), 468-472.
- [79] Zhang, G.-J.; Huang, M. J.; Ang, J. A. J.; Yao, Q.; Ning, Y., Label-free detection of carbohydrate–protein interactions using nanoscale field-effect transistor biosensors. *Anal. Chem.* 2013, *85* (9), 4392-4397.
- [80] Vedala, H.; Chen, Y.; Cecioni, S.; Imberty, A.; Vidal, S.; Star, A., Nanoelectronic detection of lectin-carbohydrate interactions using carbon nanotubes. *Nano lett.* 2010, *11* (1), 170-175.
- [81] Min, I. H.; Choi, L.; Ahn, K. S.; Kim, B. K.; Lee, B. Y.; Kim, K. S.; Choi, H. N.; Lee, W. Y., Electrochemical determination of carbohydrate-binding proteins using carbohydrate-stabilized gold nanoparticles and silver enhancement. *Biosens. Bioelectron.* 2010, *26* (4), 1326-31.

- [82] Sato, Y.; Murakami, T.; Yoshioka, K.; Niwa, O., 12-Mercaptododecyl  $\beta$ -maltoside-modified gold nanoparticles: specific ligands for concanavalin A having long flexible hydrocarbon chains. *Anal. Bioanal. Chem.* 2008, 391 (7), 2527-2532.
- [83] Schofield, C. L.; Mukhopadhyay, B.; Hardy, S. M.; McDonnell, M. B.; Field, R. A.; Russell, D. A., Colorimetric detection of Ricinus communis agglutinin 120 using optimally presented carbohydrate-stabilised gold nanoparticles. *Analyst* 2008, 133 (5), 626-634.
- [84] Bhattacharai, J. K.; Sharma, A.; Fujikawa, K.; Demchenko, A. V.; Stine, K. J., Electrochemical synthesis of nanostructured gold film for the study of carbohydrate–lectin interactions using localized surface plasmon resonance spectroscopy. *Carbohydr. Res.* 2015, 405, 55-65.
- [85] Lazar, J.; Rosencrantz, R. R.; Elling, L.; Schnakenberg, U., Simultaneous electrochemical impedance spectroscopy and localized surface plasmon resonance in a microfluidic chip: new insights into the spatial origin of the signal. *Anal. Chem.* 2016, 88 (19), 9590-9596.



## ***Chapter 2***

# **AN ELECTROCHEMICAL STUDY ABOUT THE STABILITY AND DURABILITY OF POLY (O-AMINOPHENOL) FILM ELECTRODES EMPLOYING IMPEDANCE SPECTROSCOPY AND SURFACE RESISTANCE**

***Ricardo Tucceri\****

Instituto de Investigaciones Fisicoquímicas Teóricas y Aplicadas  
(INIFTA), CONICET, Facultad de Ciencias Exactas,  
Universidad Nacional de La Plata, La Plata, Argentina

## **ABSTRACT**

The effect of storage time without use (STWU) in the supporting electrolyte solution on the conducting properties of poly(*o*-aminophenol) (POAP) film electrodes was studied. Cyclic voltammetry (CV), rotating disc electrode voltammetry (RDEV), Electrochemical Impedance Spectroscopy (EIS and surface resistance (SR) were employed. The storage of a POAP film without use for time periods longer than 32 h

---

\* Mailing Address: R. Tucceri, Instituto de Investigaciones Fisicoquímicas Teóricas y Aplicadas (INIFTA), Sucursal 4, Casilla de Correo 16, (1900) La Plata, Argentina. Fax: (54) (0221) 425-4642, E-mail address: [rtuccce@inifta.unlp.edu.ar](mailto:rtuccce@inifta.unlp.edu.ar).

strongly reduces its electroactivity. Here, this effect is called deactivation. The attenuation of the voltammetric response of the polymer film with the increase of the storage time allows one to define a degree of deactivation ( $\theta_d$ ). A decrease of the electron transport rate ( $D_e$ ) with the increase of the degree of deactivation of POAP films was obtained from RDEV measurements. This effect was attributed to the increase of the mean distance between active redox sites in the bulk of the POAP film. The relative surface resistance change ( $\Delta R/R$ ) of a gold film coated with POAP is also attenuated by the increase of the STWU. The attenuation was attributed to interfacial (gold/POAP) redox site distributions where the nearest neighbor distance between redox sites gradually increases as the degree of deactivation increases. Impedance spectra of POAP films in the presence of an electroactive solution and in the sole presence of the supporting electrolyte were analyzed on the basis of two different impedance models: The deactivation of POAP films by the STWU studied in this work was compared with deactivations caused by other electrochemical and chemical treatments, such as prolonged potential cycling (PPC), high positive potential limits (HPPL) and soaking in a ferric ion solution (SFeIS), described in previous work.

**Keywords:** poly(*o*-aminophenol) film electrodes, storage time without use, deactivation by storage, charge-transport and charge-transfer parameters

## 1. INTRODUCTION

The oxidation of *o*-aminophenol (*o*-AP) on different electrode materials (gold, platinum, carbon, indium-tin oxide, etc.) in aqueous medium was shown to form poly-*o*-aminophenol (POAP) [1-3]. *O*-AP can be polymerized electrochemically in acidic, neutral and alkaline solutions. While a conducting film is only formed in acidic media, POAP synthesized in neutral and alkaline media leads to a nonconducting film [4]. The properties of POAP synthesized in basic medium are favorable to applications in the field of bioelectrochemistry and electrocatalysis [5]. The charge-transport process at POAP films synthesized in acid medium was mainly studied from the basic research viewpoint employing different electrochemical techniques [1, 3, 6, 7]. POAP synthesized in acidic medium is also found to be a useful material to build electrochemical sensors and electrocatalysts. The development of nitric oxide [8] and ferric cations [9] sensors based on POAP synthesized in acid medium has been reported. POAP was also employed for the electrocatalytic detection of dihydronicotinamide adenine dinucleotides, NAD(P)H [10] and dissolved

oxygen reduction [11]. Considering the interest in POAP synthesized in acid medium in both basic and applied research, no much attention has been paid to the decay of the electroactivity of POAP caused by its extensive use. It is often indicated that POAP films have good electrochemical properties in terms of conductivity and ion-permeability and also that they present good durability and long-term stability under storage during several weeks. In this regard, it is assumed that the reversible redox response and conducting properties of POAP remain substantially unchanged before and after it have been used. The aim of the present work was demonstrate that charge-transport and charge-transfer parameters of POAP change with its storage without use for prolonged time periods. Four techniques were employed in this work: Cyclic Voltammetry (CV), Rotating Disc Electrode Voltammetry (RDEV), Electrochemical Impedance Spectroscopy (EIE) and Surface Resistance (SR) [12]. CV was employed to assess a degree of deactivation. RDEV data were analyzed in terms of the electron hopping model by assuming that the polymer deactivation by storage leads to an increase of the electron hopping distance between redox sites [13]. Impedance diagrams of POAP films after to be stored for different time periods were interpreted by employing two theoretical models: the first was used to obtain transport parameters when POAP contacts an electroactive solution and the second one was employed to analyze the impedance behavior of POAP films in the sole presence of the supporting electrolyte solution. The objective of the interfacial resistance measurements was to demonstrate the existence of different distributions of redox sites at deactivated POAP film electrodes as compared with nondeactivated ones. Changes of the redox site configuration after POAP deactivation by storage monitored by SR were associated to changes of the charge-transfer and charge-transport parameters obtained by employing RDEV and EIE. It is expected that the present work will shed light on the limits of stability and durability of POAP, particularly when it is proposed as material to develop sensors and electrocatalysts.

## 2. EXPERIMENTAL

### 2.1. CV, RDEV and *ac* Impedance Experiments

A gold rotating disc electrode (RDE) was used as base electrode to deposit POAP films. This gold RDE consisted of a gold rod press-fitted with epoxy resin into a Teflon sleeve so as to leave a  $1\text{cm}^2$  disc area exposed. The

electrode was carefully polished with emery paper of decreasing grit size followed by alumina suspensions of 1, 0.3 and 0.05  $\mu\text{m}$ , respectively, until a mirror-like finish was obtained. Then, it was submitted to ultrasonic cleaning to remove residual abraded polishing material. In order to obtain a more specular gold surface to deposit POAP films, a gold film about 50 nm in thickness was deposited by vacuum evaporation [12-15] ( $\sim 10^{-7}$  Torr) on the gold disc. The thickness of the evaporated gold thin film was determined as described in [14, 16]. Then, in all experiments carried out in this work, POAP films were deposited on a specular gold film surface. POAP films were grown on these base electrodes following the procedure described in [1, 2]. That is, polymer films were obtained by immersing the base electrode in a  $10^{-3}$  M *ortho*aminophenol + 0.4 M NaClO<sub>4</sub> + 0.1 M HClO<sub>4</sub> solution and cycling the potential between -0.25 and 0.8 V (*versus* SCE) at a scan rate  $v = 0.05$  V s<sup>-1</sup>. In the same way as in [6, 13, 17, 18], POAP films were grown up to an approximate thickness of  $\phi_p \sim 60$  nm by using a reduction charge ( $Q_{\text{Red,T}} = 2.8$  mC cm<sup>-2</sup>) *versus* the ellipsometric thickness working curve [17]. These POAP-coated gold film electrodes were then rinsed and transferred to the supporting electrolyte solution (0.4 M NaClO<sub>4</sub> + 0.1 M HClO<sub>4</sub>) free of monomer, where they were stabilized by a continuous potential cycling at a scan rate of 0.01 V s<sup>-1</sup>. A typical voltammetric response of these films is shown in Figure 1 (plot (a)). The POAP films maintain this response on potential cycling within the potential range  $-0.2 < E < 0.5$  V up to 500 cycles. These POAP films are herein called nondeactivated films. A large-area gold grid was used as counterelectrode. All the potentials reported in this work are referred to the SCE.

A series of eight POAP-coated RDE was prepared (see first column in Table 1) and each one of them was successively employed in an individual experiment. That is, each POAP film was stored without use in a deoxygenated supporting electrolyte solution for a given time period (see second column in Table 1) and then, it was cycled within the potential region  $-0.2 < E < 0.5$  V to obtain a stable voltammetric response. Then, the corresponding  $j-E$  responses for each one of the eight POAP films were compared. An attenuation of the voltammetric response was observed for these films as the storage time increases beyond 32 h (Figure 1). These POAP films are herein called deactivated films. Then, with both nondeactivated and deactivated by storage POAP films, RDEV and *ac* impedance experiments were performed in the presence of a solution containing equimolar concentrations of *p*-benzoquinone (Q) and hydroquinone (HQ) species (0.1 M HClO<sub>4</sub> + 0.4 M NaClO<sub>4</sub> +  $2 \times 10^{-3}$  M Q/HQ). Stationary current-potential

curves ( $I-E$ ) at different electrode rotation rates,  $\Omega$ , were recorded. From these curves, cathodic and anodic limiting current *versus* electrode rotation rate ( $I_{\text{lim}}$  *versus*  $\Omega^{1/2}$ ) dependences were obtained. Also, with nondeactivated and deactivated POAP films, *ac* impedance diagrams at the cathodic current plateaux were obtained for different electrode rotation rates. In some experiments the HQ/Q redox couple concentration in solution was varied. Impedance spectra of nondeactivated and deactivated POAP-coated electrodes in the sole presence of the supporting electrolyte solution (0.4 M NaClO<sub>4</sub> + 0.1 M HClO<sub>4</sub>) solution were also recorded.

In CV and RDEV measurements a PAR Model 173 potentiostat and a PAR Model 175 (Princeton, USA) function generator were used. An X1-X2-Y Hewlett-Packard Model 7046 B plotter (Pasadena, California, USA) was used to record  $j-E$  and steady-state current-potential curves  $I-E$ . The electrode rotation speed,  $\Omega$ , was controlled with homemade equipment that allows one to select a constant  $\Omega$  in the range  $50 \text{ rev min}^{-1} < \Omega < 7000 \text{ rev min}^{-1}$ . This was periodically controlled with a digital photo tachometer (Power Instruments Inc., model 891). Impedance spectra were measured following a 30-min application of the steady-state potential ranging from -0.35 V to 0.0 V. Impedance values were determined at seven discrete frequencies per decade with a signal amplitude of 5 mV. The validation of the impedance spectra was done by using Kramers-Kronig transformations. Impedance measurements in the frequency range 0.01 Hz–10 kHz were performed with a PAR 309 system (Princeton, USA).

AR grade chemicals were used throughout. *O*-aminophenol (Fluka, Darmstadt, Germany) was purified as described elsewhere [1, 2]. HClO<sub>4</sub> and NaClO<sub>4</sub> (Merck, Darmstadt, Germany) were used without further purification. Benzoquinone and hydroquinone (Merck, Darmstadt, Germany) were also used without purification. The solutions were prepared with water purified using a Millipore Milli-Q system ((Merck, Darmstadt, Germany).

## 2.2. Surface Resistance Measurements

The experimental arrangement employed to perform SR experiments is one in which a POAP film is supported on a rectangular thin gold film. Eight gold thin film electrodes of constant thickness  $\phi_m \sim 30 \text{ nm}$  were prepared by vacuum evaporation as was previously described [12, 14, 15]. All these electrodes exhibit initial resistance ( $R$ ) values of about 20.02 ohm. The

relationship between the length  $l$  and the width  $w$  ( $G = l/w$ ) of these gold film electrodes was 2. The electrode area was  $1 \text{ cm}^2$ . POAP films of 60 nm were grown on these base electrodes following the procedure previously described. A series of eight POAP-coated gold film electrodes was prepared and each one of them was successively employed in an individual experiment. That is, each POAP film was stored without use in a deoxygenated supporting electrolyte solution for the time periods indicated in Table 1. Then, the corresponding  $j-E$  and  $\Delta R/R-E$  responses for each one of the eight POAP films were recorded.

The experimental setup for simultaneous voltammetric and SR measurements on thin film electrodes has previously been described in detail [12, 16]. The electrochemical cell also was the same as that described previously [16]. The electrode resistance change was measured employing the three contact method described earlier (see Figure 1 and Figure 6 in [19]). In this method, the voltage drop along the resistive electrode due to a constant current ( $I_m = 1 \text{ mA}$ ) applied to the extremes is measured. That is, in this method a current is fed through two contacts at the extremes of the rectangular thin film electrode while the third one, the central contact, is connected to the current follower of the potentiostat. The possibility of coupling between the faradaic and measuring currents into the electrode was taken into account in [19]. It was demonstrated in [19] that side effects of the faradaic current passing through the electrode can be neglected when the contacts at the ends of the electrode are symmetrically placed with respect to the central one. Then, the potential drop along of the resistive electrode together the polarization current is measured as a function of the applied potential  $E$ . The voltage difference at the extremes of the film is directly proportional to the resistance, and thus to the resistivity of the electrode. The potential drop along the extremes of the film was measured with a voltmeter. The out-put of the voltmeter was compensated employing a reference tension. In this was only resistance variations,  $\Delta R$  (or  $\Delta V$  potential variations), as a function of electrode potential,  $E$ , are measured.  $\Delta R$  changes around  $10^{-4} \text{ ohm}$  could be measured. Usually, the relative resistance change as a function of potential ( $\Delta R/R-E$ ) is recorded in SR experiments, where  $R$  is a constant value. As was indicated, for a 30 nm thick gold film, the  $R$  value is 20.02 ohm.

A PAR Model 173 potentiostat together with a PAR Model 175 function generator were also used for potentiodynamic measurements. The potential drop at the extremes of the film was measured with a Keithley Model 160 voltmeter.

### 3. RESULTS AND DISCUSSION

#### 3.1. Voltammetric Responses of Nondeactivated and Deactivated POAP Films

The voltammetric response corresponding to a nondeactivated POAP film within the potential range comprised between -0.2 V and 0.5 V is shown in Figure 1 (plot (a)). As was indicated, the POAP film maintains this response within the potential range  $-0.2 \text{ V} < E < 0.5 \text{ V}$  even after to be stored without use in the supporting electrolyte solution for 32 h. However, after a higher storage time this response starts to change. Figure 1 compares the  $j-E$  responses of a nondeactivated POAP film (plots (a)) with those of the films (1), (2), (4), (5), (6) and (8) (see first column of Table 1) that were stored without use in the supporting electrolyte for the time periods listed in column 2 of Table 1. The more attenuated voltammetric response observed in Figure 1, as the storage time increases indicates a deactivation of the POAP film. In this regard, voltammetric reduction charge values corresponding to the completely reduced POAP films were compared for a nondeactivated film ( $Q_{\text{Red,T}} = 2.8 \text{ mC cm}^{-2}$ ) and the different deactivated films ( $Q_{\text{Red,c}}$ ) indicated in Table 1. Then, a degree of deactivation (column 4 of Table 1) was defined as

$$\theta_c^d = 1 - (Q_{\text{Red,c}}/Q_{\text{Red,T}}) \quad (1)$$

$Q_{\text{Red,c}}$  is the total reduction charge assessed by integration of the corresponding  $j-E$  response from  $E = 0.5 \text{ V}$  towards the negative potential direction for a deactivated film, and  $Q_{\text{Red,T}} = 2.8 \text{ mC cm}^{-2}$  is the total reduction charge for the nondeactivated film. In this way, for a nondeactivated POAP film (plot (a) in Figure 1) the degree of deactivation was  $\theta_c^d = 0$ , taking  $Q_{\text{Red,T}} = 2.8 \text{ mC cm}^{-2}$  as reference charge. However, values of  $\theta_c^d > 0$  are indicative of POAP films that have been deactivated by storage in the supporting electrolyte solution.

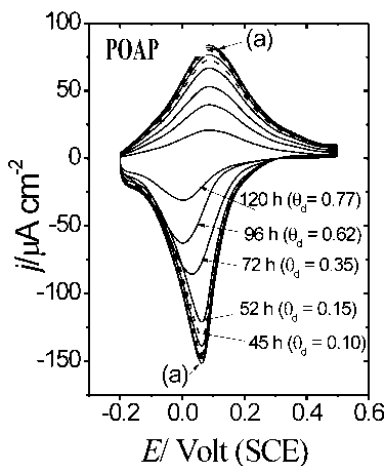


Figure 1. Voltammetric ( $j$ - $E$ ) responses for a  $2.8 \text{ mC cm}^{-2}$  ( $\phi_0 = 60 \text{ nm}$ ) thick POAP film. (a) A nondeactivated POAP film ( $\theta_d = 0$ ). The other voltammetric responses correspond to POAP films which were held without use in the supporting electrolyte solution for the time periods indicated in the figure. The degrees of deactivation of the films are indicated in Table 1. Electrolyte:  $0.1 \text{ M HClO}_4 + 0.4 \text{ M NaClO}_4$ . Scan rate:  $v = 0.01 \text{ V s}^{-1}$ .

**Table 1. Effect of the storage time without use in the supporting electrolyte solution on the voltammetric charge of a POAP film**

<sup>a</sup> POAP films	<sup>b</sup> Storage time/h	<sup>c</sup> $Q_{\text{Red},c}/\text{mC cm}^{-2}$	<sup>d</sup> $\theta_c$
1	32	2.65	0.05
2	45	2.52	0.10
3	52	2.37	0.15
4	60	2.10	0.25
5	72	1.83	0.35
6	83	1.67	0.41
7	96	1.12	0.62
8	120	0.62	0.77

<sup>a</sup> Numbers 1 to 8 represent different deactivated POAP films. <sup>b</sup> Storage time (in hours) of each POAP film in the supporting electrolyte solution. <sup>c</sup> Voltammetric reduction charge of the different deactivated POAP films after being held without use in the supporting electrolyte solution for the time periods listed in column 2. <sup>d</sup> Degree of deactivation of each one of the POAP films after being held without use in the supporting electrolyte solution for the time periods listed in column 2. The degree of deactivation achieved by each film after storage was calculated from  $\theta_c = 1 - (Q_{\text{Red},c}/Q_{\text{Red,T}})$ , where  $Q_{\text{Red,T}}$  ( $= 2.8 \text{ mC cm}^{-2}$ ) is the voltammetric reduction charge of a nondeactivated film

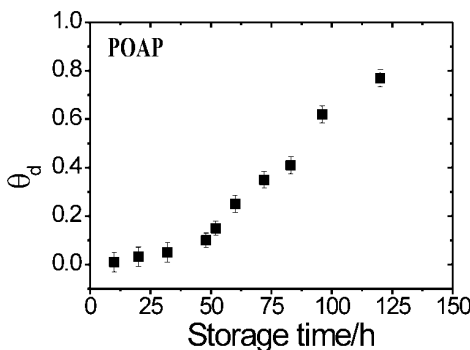


Figure 2. Degrees of deactivation of a POAP film achieved after to be stored without use in the supporting electrolyte solution for the time periods indicated in Table 1.

Figure 2 shows the dependence of the degree of deactivation of a POAP film on the storage time in the supporting electrolyte solution.

### 3.2. Rotating Disc Electrode Voltammetry and Ac Impedance Measurements in the Presence of an Electroactive Solution

As was indicated, RDEV and EIS were employed to study the behavior of nondeactivated and deactivated POAP films in contact with an electroactive solution containing the hydroquinone/p-benzoquinone redox couple. In the presence of a redox active solution, besides charge transfer between redox sites of the polymer and the external redox couple, the oxidation and reduction of fixed sites introduce charged sites into the polymer film, which, in order to achieve charge neutrality, require the ingress of counterions from the contacting electrolyte solution and, according to the Donnan relation, the egress of co-ions. Disregarding the charge-transport control, a redox polymer undergoing electrolysis may follow Fick's diffusion law and usually Fick's formalism agrees with the experimental results. Electron hopping is believed to be the mechanism for electron transport at polymer materials, but it is also possible that ion motions may partially or totally control the rate of charge transport. Then, steady-state current-potential curves were interpreted on the basis of the traditional electron hopping model [20-22] and impedance spectra were analyzed employing the general theory of ac impedance described in [23], which allows one to obtain electron and ion diffusion coefficients and different interfacial (metal/polymer and polymer/solution) resistances and capacitances of an electroactive material.

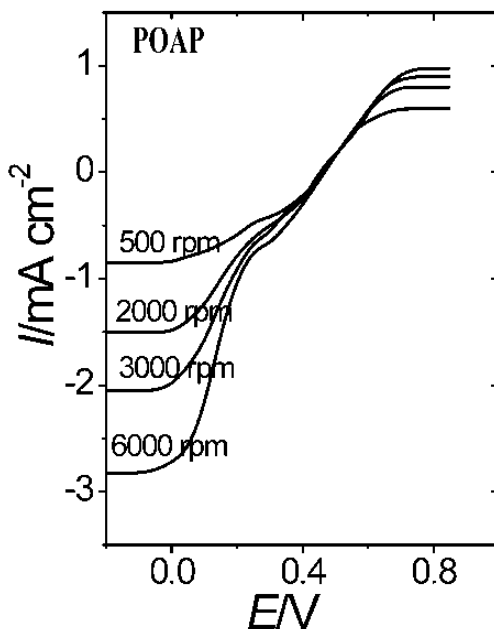


Figure 3. Steady-state current-potential ( $I-E$ ) curves for different rotation rates ( $\Omega$ ) of the rotating disc electrode. A nondeactivated POAP film.  $\Omega$  Values are indicated in the figure. Film thickness: 60 nm. Electrolyte: 0.1 M  $\text{HClO}_4$  + 0.4 M  $\text{NaClO}_4$  +  $2 \times 10^{-3}$  M( $\text{HQ}/\text{Q}$ ).

In previous work [18] RDEV experiments at gold electrodes coated with POAP films were carried out to study the diffusion processes of benzoquinone ( $Q$ ) and hydroquinone ( $\text{HQ}$ ) species through nondeactivated films. Diffusion-limited currents at  $E < 0.0$  V for  $Q$  reduction and at  $E > 0.8$  V for  $\text{HQ}$  oxidation were observed. While the anodic limiting current corresponds to the oxidation of  $\text{HQ}$  species that penetrate through the polymer film to reach the metal surface, cathodic limiting currents for  $Q$  reduction are related to a rapid electron-transfer mediation at the POAP|redox active solution interface, which occurs without significant penetration of  $Q$  into the polymer layer. As we use the theory of Vorotyntsev et al. [23] to interpret the impedance behavior of POAP films and this theory was developed within the framework of the assumption that the redox active species are only present in the solution phase but not inside the film, and they participate in the interfacial electron exchange with the polymer at the film-solution boundary, only the electrochemical behavior of nondeactivated and deactivated POAP films at negative potential values ( $E < 0.0$  V) was considered.

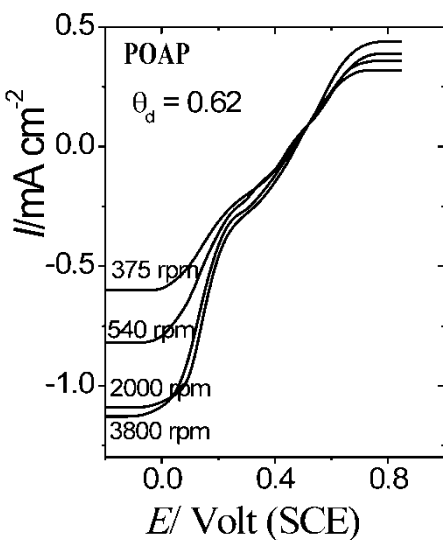


Figure 4. Steady-state current-potential ( $I$ - $E$ ) curves for different rotation rates ( $\Omega$ ) of the rotating disc electrode. A deactivated POAP film ( $\theta_d = 0.62$ ).  $\Omega$  Values are indicated in the figure. Film thickness: 60 nm. Electrolyte: 0.1 M HClO<sub>4</sub> + 0.4 M NaClO<sub>4</sub> +  $2 \times 10^{-3}$  M(HQ/Q).

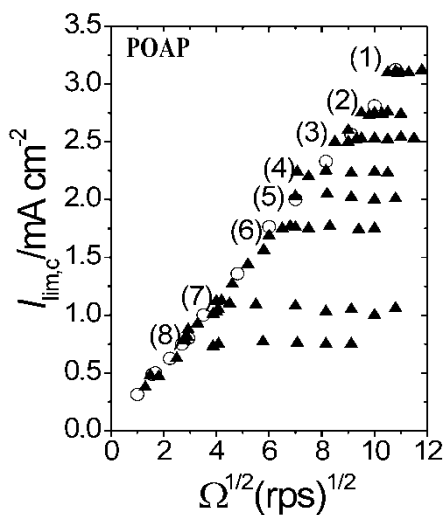


Figure 5. Levich representations  $I_{\text{lim},c}$  versus  $\Omega^{1/2}$  for POAP films contacting a 0.1 M HClO<sub>4</sub> + 0.4 M NaClO<sub>4</sub> +  $2 \times 10^{-3}$  M (HQ/Q) solution. (O) Empty circles correspond to a nondeactivated POAP film. Black triangles correspond to deactivated films. Numbers from (1) to (8) indicate the different films listed in Table 1.

Figure 3 shows stationary current-potential curves ( $I$ - $E$ ) at different electrode rotation rates,  $\Omega$ , for a nondeactivated POAP film contacting a 0.1 M HClO<sub>4</sub> + 0.4 M NaClO<sub>4</sub> + 2 × 10<sup>-3</sup> M Q/HQ solution. ( $I$ - $E$ ) curves at different  $\Omega$  values were also obtained for each one of the deactivated POAP films indicated in Table 1. For instance, Figure 4 shows this representation for a deactivated POAP film with  $\theta_d = 0.62$ . As can be seen by comparing Figures 3 and 4, at each electrode rotation rate, both anodic and cathodic limiting currents for a deactivated POAP film are lower than those for a nondeactivated one. Also, after a given electrode rotation rate, which depends on the degree of deactivation, the cathodic limiting current for a deactivated film becomes independent of this variable.  $I_{\text{lim},c}$  versus  $\Omega^{1/2}$  dependences at potential values  $E < 0.0$  V for both nondeactivated and deactivated POAP films are shown in Figure 5. For a nondeactivated POAP film a linear  $I_{\text{lim},c}$  versus  $\Omega^{1/2}$  dependence, which follows the Levich equation, is obtained within a wide range of  $\Omega$  values (empty circles in Figure 5). However, for POAP films that have been deactivated by storage without use for different time periods, after a certain  $\Omega$  value, a constant cathodic limiting current value,  $I_{\text{lim},c}$ , independent of  $\Omega$  is achieved (black triangles in Figure 5). Also, it is observed that the transition at which the cathodic limiting current becomes independent of  $\Omega$  occurs at lower  $\Omega$  values as the degree of deactivation increases. The explanation of this effect can be given in terms of the electron hopping model [20-22]. Limiting current values at which  $I_{\text{lim},c}$  (=  $I_e$ ) becomes constant were considered as a representation of the maximum flux of electrons confined in the polymer, according to Eq. (2) [22]

$$I_e = n F A D_e c / \phi_p \quad (2)$$

In Eq. (2),  $c$  is the concentration of redox sites of the polymer and  $\phi_p$  the polymer film thickness.  $D_e$  represents a measure of the electron hopping rate and  $n$  expresses the numbers (fractions) of unit charges per monomer unit of the polymer.  $A$  is the electrode area and  $F$  the Faraday's constant. Experimental  $I_e$  values, corresponding to each one of the eight deactivated POAP films contacting a 2 × 10<sup>-3</sup> M HQ/Q solution, were extracted from the cathodic plateau and they are listed in Table 2 (Third column).

As can be seen from Table 2,  $I_e$  decreases with increasing  $\theta_d$ . The constant value of the current ( $I_e$ ) at a given  $\Omega$  value for deactivated POAP films can be related to a slow electron transport across the POAP film to mediate in the electron-transfer reaction at the polymer|solution interface, as compared with a

nondeactivated POAP film. As one increases the flux of  $Q$  (increase of  $\Omega$ ) from the bulk solution, then if the flux exceeds the supply of electrons from the electrode through the polymer to the electrolyte interface, the rate-limiting step will shift from the limiting transport of  $Q$  to the limiting transport of the charge through the polymer. In order to verify this limiting charge-transport process across the POAP film, the HQ/Q concentration in solution was varied. It is found that the constant current for a given deactivated film remains unchanged with changing redox couple concentration in solution. According to Eq. (2), the slower electron transport in deactivated films, as compared with nondeactivated ones, could be attributed to a decrease of  $D_e$ . By employing the  $I_e$  values shown in Table 2 and using the parameter values  $c = 4.7 \text{ M}$  [1],  $A = 1 \text{ cm}^2$ ,  $n = 0.44$  [24] and  $\phi_p = 60 \text{ nm}$  in Eq. (2), one obtains a decrease of  $D_e$  from  $2.00 \times 10^{-11}$  to  $0.5 \times 10^{-11} \text{ cm}^2 \text{ s}^{-1}$  for a relative increase of  $\theta_c$  from 0.05 to 0.77.

**Table 2. Efficiency ( $I_e/I_0 \times 100$ ) of a POAP film to act as mediator in the HQ/Q redox reaction after to be stored without use in the supporting electrolyte solution for different time periods**

POAP Film	$\theta_c^d$	$I_e/\text{mA cm}^{-2}$	$I_e/I_0 \times 100$
1	0,05	3.01	94
2	0,10	2.75	86
3	0,15	2.55	79
4	0,25	2.23	70
5	0,35	2.02	63
6	0,41	1.74	54
7	0,62	1.05	33
8	0,77	0,55	16

As can be seen from Figure 6, the electron diffusion coefficient extracted from RDEV measurements seems to decrease linearly with the increase of  $\theta_d$ . The electron diffusion coefficient,  $D_e$ , in electroactive materials has been expressed in terms of the mean distance between adjacent active redox sites [25], according to  $D_e = (a^2 k_o)$ , where  $k_o$  is the intermolecular electron-transfer rate constant and  $a$  is the mean distance between two adjacent redox sites. The hopping rate,  $k_o$ , exhibits an exponential dependence on  $a$ , through the energy  $-U(x+a)$  of a state with an electron in the position  $x$  along the current direction (see eq. (23) in Ref. [25]). In this respect, a  $k_o$  decrease should be expected as the hopping distance  $a$  increases. The decrease of  $D_e$  obtained from Eq. (2)

could be attributed to an increase of the hopping distance between remnant active redox sites after polymer deactivation by storage. A similar explanation has been given to justify impedance data which show a decrease of the electronic conductivity of POAP with the increase of the solution *pH* [26]. As the electronic conductivity in electroactive polymers depends on the electron diffusion coefficient, then the  $D_e$  decrease with *pH* increase was adjudicated to a decrease of the intermolecular electron-transfer rate constant,  $k_o$ , with the polymer deprotonation. In this regard, it is well-known that POAP deactivates with the increase of the solution *pH* [1, 2]. It is interesting to remark that a constant current  $I_e$  independent of  $\Omega$  is also obtained for a nondeactivated POAP film in contact with a 0.1 M HClO<sub>4</sub> + 0.4 M NaClO<sub>4</sub> + 2 × 10<sup>-3</sup> M Q/HQ solution. However, in this case the constant current is obtained at very high electrode rotation rates ( $\Omega > 9000$  rpm). It is possible that at high angular speeds of the rotating disc electrode, the flux into the bulk solution would not longer laminar, so that the proportionality between the current and  $\Omega^{1/2}$ , should not be expected. However, if the HQ/Q concentration is increased (0.01 M) a constant current  $I_e$  ( $\approx 15$  mA cm<sup>-2</sup>) is observed for a nondeactivated film at about 7000 rpm (Figure 7). As this value is reproducible and it decreases as the deactivation of the polymer increases, then our interpretation of a change in the rate limiting process during the mediated electron-transfer reaction seems to be correct. Similar effects were observed for other polymers [27]. Considering the constant current value obtained for high HQ/Q concentrations, a  $D_e$  about 1.22 × 10<sup>-10</sup> cm<sup>2</sup> s<sup>-1</sup> is obtained for a nondeactivated POAP film. This finding seems to indicate that a restriction for the electron transport also occurs across a nondeactivated POAP film in contact of a concentrated electroactive solution and high enough flux into the bulk solution.

On the basis of data showed in Figures 5 and 6, one can assess the efficiency of POAP to act as mediator in the 0.1 M HClO<sub>4</sub> + 0.4 M NaClO<sub>4</sub> + 2 × 10<sup>-3</sup> M Q/HQ solution. By taking as reference a high enough electrode rotation rate ( $\Omega = 7000$  rpm) to reach a constant current for all the deactivated films treated in the work (Figures 5 and 6), one can calculate the ( $I_e/I_o \times 100$ ) ratio, where  $I_e$  are the different constant current values for the different deactivated films (see Table 2) and  $I_o$  is the current value (3.2 mA cm<sup>-2</sup>) corresponding to the nondeactivated film, which follows the Levich relationship at  $\Omega = 7000$  rpm (Figure 5). In Table 2, ( $I_e/I_o \times 100$ ) represents the efficiency of POAP to act as mediator in the HQ/Q redox reaction. For a nondeactivated film,  $I_o = I_e = 3.2$  mA cm<sup>-2</sup> at  $\Omega = 7000$  rpm, then,  $I_e/I_o = 1$  and ( $I_e/I_o \times 100$ ) = 100, which corresponds to the maximal efficiency. As can be

seen from the Table 2, the efficiency of a POAP film is reduced to about 16 per cent for a storage time without use of 120 h.

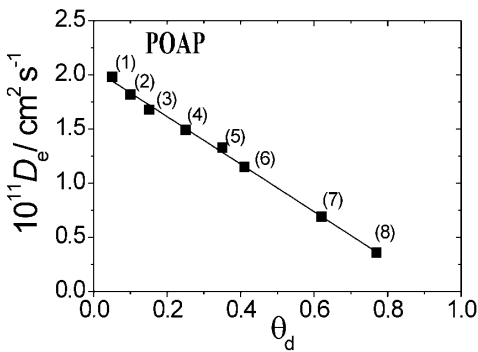


Figure 6. Electron diffusion coefficient ( $D_e$ ) (Eq. (2)) as a function of  $\theta_d$ . Numbers (1) to (8) correspond to each one of the deactivated POAP films listed in Tables 1 and 2.

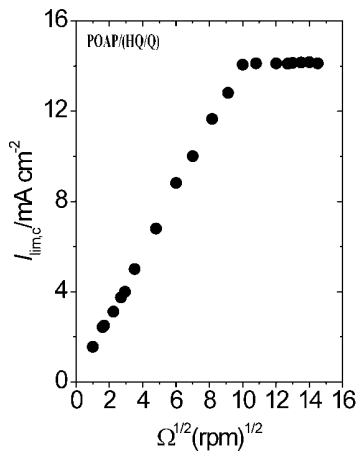


Figure 7. Levich representation  $I_{\text{lim},c}$  versus  $\Omega^{1/2}$  for a nondeactivated POAP film contacting a 0.1 M HClO<sub>4</sub> + 0.4 M NaClO<sub>4</sub> + 0.01 M (HQ/Q) solution.

Impedance measurements were also performed with nondeactivated and deactivated POAP films contacting a 0.1 M HClO<sub>4</sub> + 0.4 M NaClO<sub>4</sub> + 2 × 10<sup>-3</sup> M (Q/HQ) solution at potential values  $E < 0.0$  V. Nyquist diagrams at different electrode rotation rates for a nondeactivated POAP film are shown in Figure 8. A Warburg region at high frequency, followed by a semicircle, is observed in the impedance diagrams of a nondeactivated film.

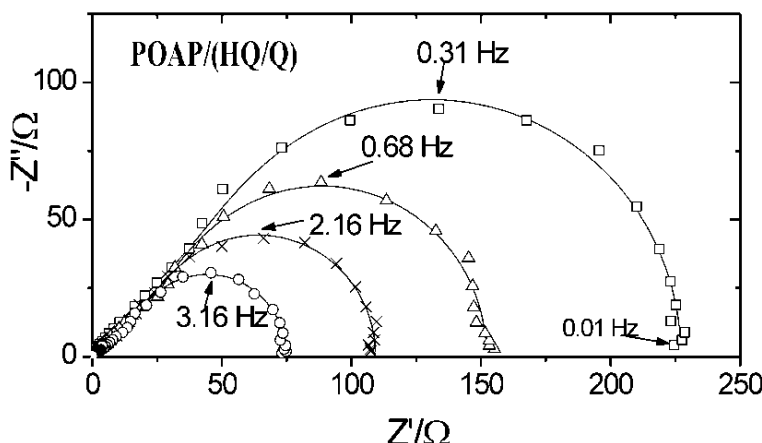


Figure 8. Ac impedance diagrams in the Nyquist coordinates ( $-Z''$  versus  $Z$ ) obtained at  $E = -0.3$  V for a nondeactivated POAP film. The different diagrams correspond to different electrode rotation rates,  $\Omega$ : (□) 100 rpm; (Δ) 200 rpm; (X) 300 rpm; (O) 600 rpm. Electrolyte: 0.1 M HClO<sub>4</sub> + 0.4 M NaClO<sub>4</sub> + 2 × 10<sup>-3</sup> M (HQ/Q) solution. Discrete points are experimental data and continuous lines represent the fitting by using the theory given in [23].

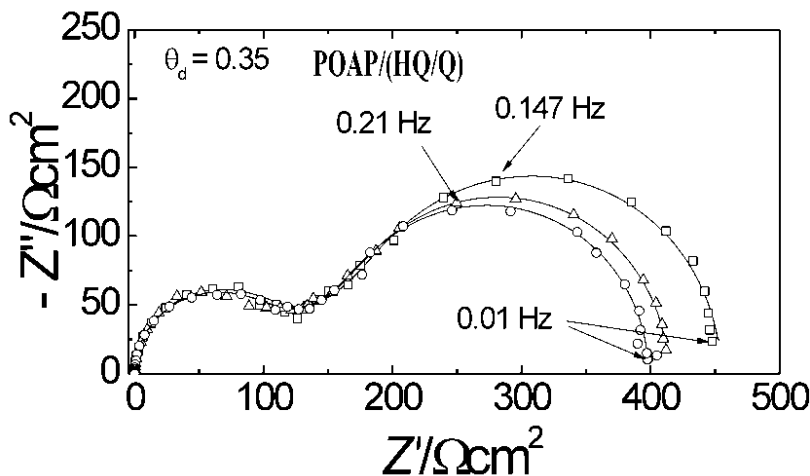


Figure 9. Ac Impedance diagrams in the Nyquist coordinates ( $-Z''$  versus  $Z$ ) obtained at  $E = -0.2$  V for a deactivated POAP film,  $\theta_d = 0.35$ . The different diagrams correspond to different electrode rotation rates,  $\Omega$ : (O) 2600 rpm; (Δ) 1500 rpm; (□) 1000 rpm. Electrolyte: 0.1 M HClO<sub>4</sub> + 0.4 M NaClO<sub>4</sub> + 2 × 10<sup>-3</sup> M (HQ/Q) solution. Discrete points are experimental data and continuous lines represent the fitting by using the theory given in [23].

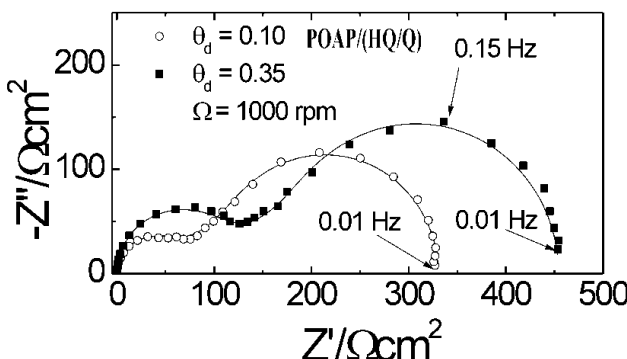


Figure 10. *Ac* Impedance diagrams in the Nyquist coordinates ( $-Z''$  versus  $Z'$ ) obtained at  $E = -0.2$  V and a constant electrode rotation rate,  $\Omega = 1000$  rpm, for two deactivated POAP films: (O)  $\theta_d = 0.10$ ; (■)  $\theta_d = 0.35$ . Electrolyte:  $0.1$  M  $\text{HClO}_4 + 0.4$  M  $\text{NaClO}_4 + 2 \times 10^{-3}$  M (HQ/Q) solution. Discrete points are experimental data and continuous lines represent the fitting by using the theory given in [23].

Impedance diagrams of each one of the eight deactivated POAP films indicated in Table 1 exhibit two loops (Figure 9). While the loop at low frequency is  $\Omega$  dependent, the high-frequency semicircle is independent of this variable. However, the size of the high-frequency semicircle depends on the degree of deactivation (Figure 10). In this regard, at a given  $\Omega$  value, the higher the  $\theta_d$  value is, the greater the high-frequency semicircle becomes.

Although several *ac* impedance diagrams at potential values within the range  $-0.30$  V  $< E < 0.0$  V (*versus* SCE) were recorded for different POAP films, those shown in Figures 8 to 10 were considered as representative of the potential region where POAP is in its reduced state. The coverage of the gold disc surface with an evaporated gold film, as described in the experimental section, leads to reproducible impedance data within the potential range comprised between  $-0.3$  V and  $0.0$  V. The good reproducibility can be attributed to the use of a smooth and renewable gold surface, obtained by evaporation, to deposit the POAP film in each experiment. However, it should be indicated that impedance data at potential values slightly more negative than  $-0.30$  V exhibit a strong increase in values of the real impedance constituent, which leads to poor reproducibility of experimental data. In this regard, at potential values more negative than  $-0.30$  V, the gold film deposited by vacuum evaporation on the gold disc electrode is slowly detached (peeled off) from the gold disc surface, possibly due to incipient hydrogen evolution (bubbles on the gold film surface are visible). Impedance data obtained in such conditions were not reproducible, and then they are not presented here.

### 3.2.1. Interpretation of Ac Impedance Diagrams

On the basis of the experimental arrangement used, i.e., a gold disc electrode of low surface roughness (high specularity) after deposition of a thin gold film by evaporation coated with a thick POAP film [7, 28], the system could be considered as a good enough approximation to a uniform polymer layer deposited on a smooth electrode surface to apply a homogeneous electrochemical impedance model in the interpretation of experimental *ac* impedance diagrams.

It is well-known that thin metal films obtained by evaporation (low rate of evaporation) exhibit specular surfaces with a relatively low amount of defects as compared with a massive metal surface. The specularity of a metal film surface being represented by its specularity parameter,  $p$  [12, 14]. The value of  $p$  for a thin metal film can be interpreted as the fraction of the surface which specularly reflects conduction electrons from the inside of the film to its surface. The value of  $p$  ranges from 0 for complete diffuse scattering to 1 for complete specular scattering. The value of  $p$  depends on the quality of the metal film surface, that is, on the method of preparation of the metal film. Thus, a metal film surface with a smooth mirrorlike finish, which is free of defects, should have a specularity parameter near 1. Our gold films are prepared at low evaporation rates and they show a specularity parameter near 0.91. For more details about the significance of  $p$  see section 4.

With regard to the thickness of the POAP film, it was demonstrated in a previous work [18] that POAP deposition on a rotating gold disc starts with the formation of a rather porous structure whereas dense structures are formed later on as the polymer thickness increases. SEM images (Figure 8 in [18]) and permeation rate measurements (Table 1 in [18]) show that thick POAP films (thickness higher than 50 nm thickness) are uniform and compact enough to restrain the physical diffusion of species through the film. Also, recent resistance measurements on POAP-coated gold film electrodes [28] demonstrate the POAP coverage higher than  $0.8 \text{ mC cm}^{-2}$  (60 nm) are sufficiently compact at the gold-POAP interface to prevent the specific adsorption of anions and cations proceeding from the external electrolyte solution on the gold film surface.

Then, as was indicated, the general theory of *ac* impedance described by Vorotyntsev et al. in [23] was employed to interpret experimental impedance data of this modified electrode system. It should be indicated that the theory developed in [23] is strictly valid when the charging of interfacial double layers is negligible, i.e., it does not account for the charging of the film|substrate and film|solution layers in parallel with the processes of

injection of charge carriers. If this is not the case, a more complete model, such as the one developed by Vorotyntsev in [29], should have to be used. In this model [29], besides the traditional “double-layer” capacitance and interfacial charge-transfer resistances, two additional parameters for each boundary, “interfacial numbers” for each species and “asymmetry factors,” are introduced. Although we also fitted our experimental impedance diagrams with the model reported in [29], the fitting did not result much more precise than that using the model given in [23], and furthermore, the increasing mathematical difficulty of determining the numerous parameters of the model given in [29] from experimental data was a major drawback. Then, despite this last theoretical limitation, the model described in [23] concerning a uniform and nonporous film and no penetration of redox species from the solution was employed to interpret our experimental impedance diagrams.

As in the present case one has the modified electrode geometry with a redox active electrolyte solution ( $m|film|es$ ), Eq. (41) of Ref. [23] (Eq. (3) in this work) must be applied

$$Z_{m|film|es} = R_{m|f} + R_f + R_s + [Z_e^{fs} R_i^{fs} + W_f Z_{12}^m] (Z_e^{fs} + R_i^{fs} + 2 W_f \coth 2\nu)^{-1} \quad (3)$$

where

$$Z_{12}^m = Z_e^{fs} [\coth \nu + (t_e - t_i)^2 \tanh \nu] + R_i^{fs} 4t_i^2 \tanh \nu + W_f 4t_i^2 \quad (4)$$

In Eqs. (3) and (4):

$\nu = [(j\omega\phi_p^2)/4D]^{1/2}$  is a dimensionless function of the frequency  $\omega$ ,  $\phi_p$  is the film thickness,  $D$  is the binary electron-ion diffusion coefficient, and  $t_i$  and  $t_e$  are the migration (high frequency) bulk-film transference numbers for anions and electrons, respectively.  $D$  is defined as  $D = 2D_e D_i (D_e + D_i)^{-1}$  and  $t_{i,e} = D_{i,e} (D_e + D_i)^{-1}$ , where  $D_e$  and  $D_i$  are the diffusion coefficients for the electrons and ion species, respectively.

$W_f = [\nu/j\omega\phi_p C_p] = \Delta R_f/\nu$  is a Warburg impedance for the electron-ion transport inside the polymer film.  $\Delta R_f (= \phi_p/4DC_p)$  is the amplitude of the Warburg impedance inside the film, and  $C_p$  is the redox capacitance per unit volume.

$R_f (= \phi_p/\kappa)$  is the high-frequency bulk-film resistance,  $R_s$  the ohmic resistance of the bulk solution ( $\kappa$  is the high-frequency bulk conductivity of the film),  $R_{m|f}$  is the metal|film interfacial electron-transfer resistance, and  $R_i^{fs}$  is the film|solution interfacial ion-transfer resistance.

$Z_e^{\text{fls}} = (R_e^{\text{fls}} + W_s)$  is the electronic impedance, where  $R_e^{\text{fls}}$  is the interfacial electron-transfer resistance at the film|solution interface, and  $W_s$  is the convective diffusion impedance of redox species in solution, which contains the bulk concentrations of ox(red) forms,  $c_{\text{ox}}(c_{\text{red}})$ , and their diffusion coefficients inside the solution,  $D_{\text{ox}}(D_{\text{red}})$ . Also, it contains the Nernst layer thickness,  $\delta$ .

$R_e^{\text{fls}}$  is defined as

$$R_e^{\text{fls}} = RT (nF^2 k_o c_{\text{red}})^{-1} \quad (5)$$

where  $k_o$  is the rate constant of the reaction between the film and the redox active forms in solution. Diffusion of the redox forms from the bulk solution to the film|solution interface can be regarded as stationary through the diffusion layer thickness, expressed in cm by

$$\delta = 4.98 D_{\text{ox,red}}^{1/3} \eta^{1/6} \Omega^{-1/2} \quad (6)$$

where  $\eta$  is the kinematic viscosity of the solution in the same units as  $D_{\text{ox,red}}$ , and  $\Omega$  the rotation rate of the disk electrode in rpm. The rest of the constants have their usual meaning. This model also includes the impedance behavior of the polymer contacting the inactive electrolyte (absence of the redox couple in solution) by considering  $Z_e^{\text{fls}} \rightarrow \infty$  in Eq. (3).

### 3.2.2. Dependences of the Different Charge-Transport and Charge-Transfer Parameters on the Degree of Deactivation

As was indicated, continuous lines on the impedance diagrams shown from Figures 8 to 10 are simulated curves calculated by using Eq. (3). As it is often considered that some transformed curves could give more valuable information about the goodness of the fitting than Nyquist plots, real and imaginary parts *versus* frequency plots corresponding to each one of the Nyquist representations were also built. One of these representations for a  $\theta_c^d$  value of 0.42 is shown in Figure 8.

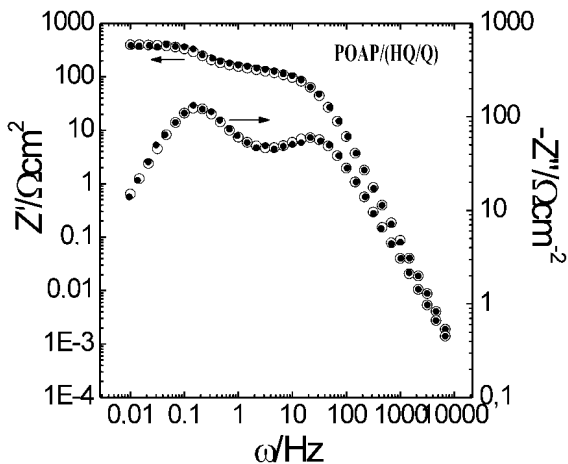


Figure 11. Real part ( $Z'$ ) and imaginary part ( $-Z''$ ) versus frequency ( $\omega$ ) plots (point-to-point representations) for a POAP film with  $\theta_d = 0.62$ .  $E = -0.3$  V,  $\Omega = 2600$  rpm. Electrolyte:  $0.1$  M  $\text{HClO}_4 + 0.4$  M  $\text{NaClO}_4 + 2 \times 10^{-3}$  M (HQ/Q) solution. (●) Experimental data; (○) fitting by using Eq. (3) [23].

A good fitting was observed for the different impedance diagrams. The fitting procedure by using Eq. (3) was based on the CNLS (Complex Nonlinear Squares) method. A rigorous fitting procedure was performed. Six replicate measurements for each degree of deactivation were carried out, and the error structure was assessed following the method recommended by Agarwal et al. [30-32] and Orazem [33]. The standard deviation for the real ( $\sigma_{Zr}$ ) and imaginary ( $\sigma_{Zj}$ ) parts of the impedance followed the form proposed by Orazem (see eq. (8) of Ref. [33])

$$\sigma_{Zr} = \sigma_{Zj} = \alpha |Z_j| + \beta |Z_r| + \gamma |Z|^2 R_m^{-1} + \delta \quad (7)$$

where  $R_m$  is the current measuring resistor used for the experiment,  $Z_r$  is the real part of the impedance, and  $Z_j$  is the imaginary part of the impedance.  $\alpha$ ,  $\beta$ ,  $\gamma$  and  $\delta$  are constants that have to be determined. The values of these scaling factors were  $\alpha = 0$ ,  $\beta = 3.15 \times 10^{-3} \pm 0.005 \times 10^{-3}$ ,  $\gamma = 2.7 \times 10^{-5} \pm 0.1 \times 10^{-5}$  and  $\delta = 6.8 \times 10^{-3} \pm 0.3 \times 10^{-3}$ . The error structure was found to follow the same model within the range of degree of capture  $0.05 < \theta_d < 0.77$ . At  $\theta_d$  values lower than 0.05, the error structure model parameters had different values, but these results are not reported here. Then, continuous lines in Figures 8 to 10 and point representation in Figure 11 represent the weighted

complex nonlinear least-squares fit to the data. The regression was weighted by the inverse of the variance of the stochastic part of the measurement. In all conditions the weighted sum of the square of the residuals was below one [33].

In the simulations the number of transferred electrons,  $n$ , was assumed to be 0.44 [24], and diffusion coefficient values of the redox species (Q and HQ) were considered equal,  $D_{\text{ox,red}} = 1.5 \times 10^{-5} \text{ cm}^2 \text{ s}^{-1}$ . Also, the bulk concentrations of the redox substrate species were considered equal ( $c_{\text{ox}} = c_{\text{red}} = 2 \times 10^{-6} \text{ mol cm}^{-3}$ ). The polymer thickness was considered as  $\phi_p = 60 \text{ nm}$  [18]. The value of the total redox site concentration of POAP was considered as  $c_o = 4.7 \times 10^{-3} \text{ mol cm}^{-3}$  [1, 24]. The ohmic resistance of the solution in contact with the polymer films,  $R_s$ , was measured. A value  $R_s \sim 1.43 \text{ ohm cm}^2$  was obtained. Then, by considering the high-frequency intercept of impedance diagrams of POAP films in the presence and in the absence of the redox couple in solution as  $R_o$ , the high-frequency bulk POAP film resistance,  $R_f$ , was calculated as  $R_f = R_o - R_s$  [34]. The latter value varied within the range  $1.17 < R_f < 2.14 \text{ ohm cm}^2$  and it seems not to be strongly dependent on the degree of deactivation. Then,  $R_f$  and  $R_s$  values were imposed in the fitting. The remnant parameters contained in Eq. (3) ( $R_{\text{mf}}$ ,  $R_i^{\text{fs}}$ ,  $R_e^{\text{fs}}$ ,  $C_p$ ,  $D_e$  and  $D_i$ ) were calculated from the experimental impedance data by the fitting procedure described above. The first three parameters ( $R_{\text{mf}}$ ,  $R_i^{\text{fs}}$  and  $R_e^{\text{fs}}$ ) were varied without restraints during the fitting. However, some reference values were considered for  $C_p$ ,  $D_e$  and  $D_i$ . For the nondeactivated POAP film thickness used in this work ( $\phi_p = 60 \text{ nm}$ ) and solution  $pH = 1$ ,  $D_e$  and  $D_i$  values were allowed to vary within the range  $10^{-7}$ - $10^{-12} \text{ cm}^2 \text{ s}^{-1}$ , in such a way that diffusion coefficient values lower than  $10^{-12}$  were considered unrealistic for these thick films. That is,  $D_e$  and  $D_i$  values lower than  $10^{-12}$  were only obtained from impedance diagrams (not shown) of very thin POAP films ( $Q_{\text{T,Red}} = 0.15 \text{ mC cm}^{-2}$ ,  $\phi_p = 9 \text{ nm}$ ) contacting solutions of  $pH = 1$ , where incomplete coating of the metal area by the thin polymer film is possible. Concerning  $C_p$ , reference values were extracted from experimental  $-Z''$  versus  $\omega^1$  slopes of impedance diagrams at sufficiently low frequency (in the absence of the redox substrate in solution). A contribution of the interfacial capacitance,  $C_H$ , also considered as a fitting parameter, was included in order to represent the actual impedance diagrams from the calculated ones.

Different charge-transport and charge-transfer parameters versus  $\theta_d$  dependences, extracted from the fitting procedure described above, are shown from Figures 12 to 17.

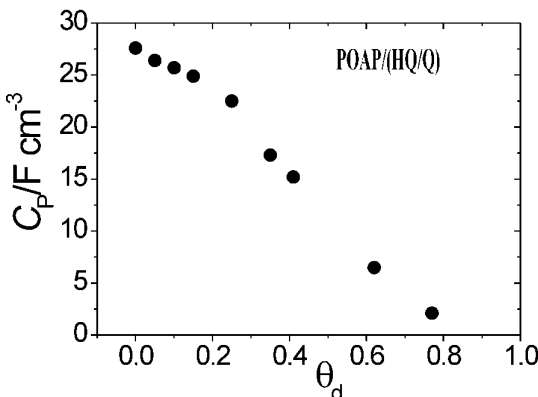


Figure 12. Redox capacitance ( $C_p$ ) as a function of  $\theta_d$ . The value  $27.5 \text{ F cm}^{-3}$  for  $\theta_d = 0$  corresponds to a nondeactivated film. Electrolyte:  $0.1 \text{ M HClO}_4 + 0.4 \text{ M NaClO}_4 + 2 \times 10^{-3} \text{ M (HQ/Q)}$  solution.

The  $C_p$  versus  $\theta_c$  dependence is shown in Figure 12. As can be seen, starting from a  $C_p$  value of about  $27.5 \text{ F cm}^{-3}$ , for a nondeactivated film, a slow decrease of  $C_p$  with increasing  $\theta_d$  up to 0.3 is observed. Then, from a degree of deactivation of 0.3 up to 0.77, a more pronounced decrease is observed. In this regard, a break at a degree of deactivation about 0.3 seems to be evident in the  $C_p$  versus  $\theta_c$  dependence. The observed decrease of the redox capacitance is consistent with the gradual attenuation of the voltammetric response as the degree of deactivation increases (Figure 1). It should be kept in mind that these  $C_p$  values correspond to the reduced state of POAP. There was no difference in the redox capacitance *versus*  $\theta_d$  dependence achieved in the supporting electrolyte from the  $-Z'$  *versus*  $\omega^1$  slopes and in the presence of the redox active substrate from Eq. (3). Only small differences in the numerical values of  $C_p$  were found. The good agreement between the redox capacitance values attained under these different conditions could be considered as an indication of the high fitting accuracy reached to obtain optimum parameter values (in this case  $C_p$ ) for the treated system by using Eq. (3).

$R_{\text{mf}}$  and  $R_{\text{i}}^{\text{fs}}$  on  $\theta_d$  dependences are shown in Figures 13 and 14, respectively.  $R_{\text{i}}^{\text{fs}}$  as a function of  $\theta_d$  exhibits a different feature as compared with  $R_{\text{mf}}$ . That is, while  $R_{\text{mf}}$  increases almost linearly within the whole  $\theta_d$  range,  $R_{\text{i}}^{\text{fs}}$  shows a clear break about a degree of deactivation of 0.3. In this regard,  $R_{\text{i}}^{\text{fs}}$  firstly exhibits a slow increase in the  $\theta_d$  range comprised between 0.0 and 0.3 and then, a more pronounced increase between 0.3 and 0.7 is observed. The magnitude of  $R_{\text{mf}}$  and  $R_{\text{i}}^{\text{fs}}$  change within the whole  $\theta_d$  range is

also different. The whole  $R_i^{fs}$  change is around four times lower than  $R_{mf}$  change. It is possible that both resistances contribute to the high-frequency semicircle on impedance diagrams shown in Figures 8 to 10. The increase of interfacial  $R_{mf}$  resistance could be due to an increasing number of inactive sites at the metal|polymer interface with the increase of deactivation. The  $R_i^{fs}$  increase with the increase of the degree of deactivation could be attributed to an increasing difficulty to incorporate ions into the polymer matrix as the polymer becomes deactivated more.

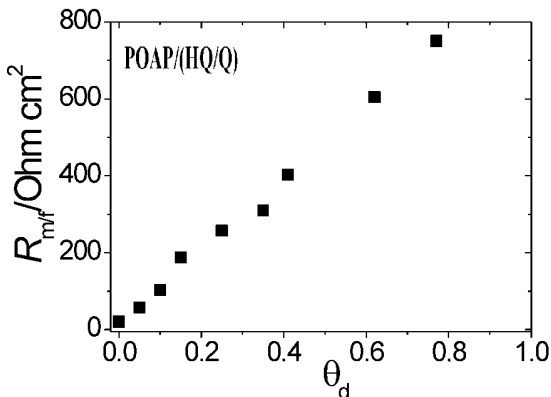


Figure 13. Metal-polymer interfacial electron-transfer resistance ( $R_{mf}$ ) as a function of  $\theta_d$ . Electrolyte: 0.1 M HClO<sub>4</sub> + 0.4 M NaClO<sub>4</sub> + 2 × 10<sup>-3</sup> M (HQ/Q) solution.

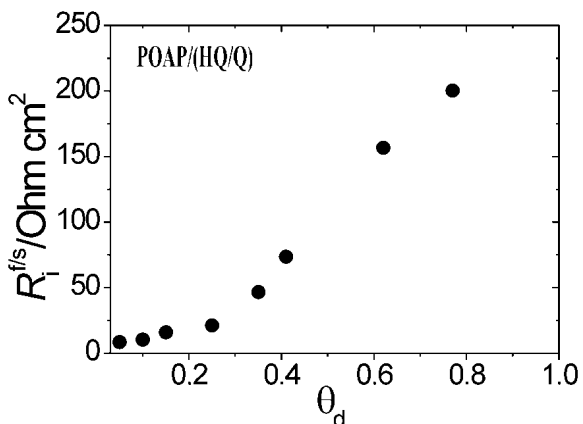


Figure 14. Polymer-solution interfacial ion-transfer resistance ( $R_i^{fs}$ ) as a function of  $\theta_i$ . Electrolyte: 0.1 M HClO<sub>4</sub> + 0.4 M NaClO<sub>4</sub> + 2 × 10<sup>-3</sup> M (HQ/Q) solution.

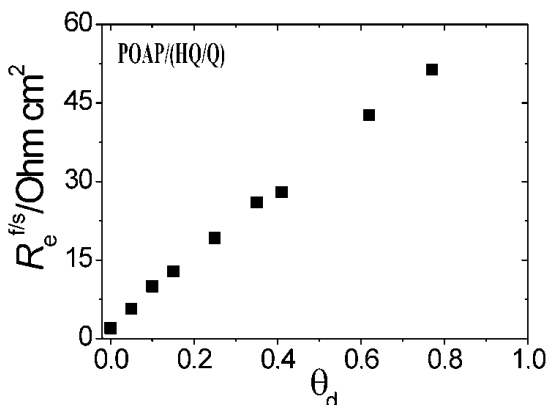


Figure 15. Interfacial electron-transfer resistance ( $R_e^{fs}$ ) as a function of  $\theta_d$ . Electrolyte: 0.1 M  $\text{HClO}_4$  + 0.4 M  $\text{NaClO}_4$  +  $2 \times 10^{-3}$  M (HQ/Q) solution.

$R_e^{fs}$  values were extracted from Eq. (5) using  $k_o$  as fitting parameter ( $0.01 < k_o < 1000 \text{ cm s}^{-1}$ ). The feature of  $R_e^{fs}$  versus  $\theta_d$  dependence is similar to  $R_{m/f}$  versus  $\theta_d$  dependence. However, the  $R_e^{fs}$  values are around one order of magnitude lower than  $R_{m/f}$  values. Also, it is interesting to note that the  $R_e^{fs}$  change is lower than the  $R_i^{fs}$  change within the whole  $\theta_d$  range. Then, the storage time without use seems to affect more strongly the polymer|solution interfacial ion-transfer resistance  $R_i^{fs}$  than the polymer|solution interfacial electron-transfer resistance,  $R_e^{fs}$ . The increase of interfacial  $R_e^{fs}$  resistance could be due to an increasing number of inactive sites at the polymer|solution interface with the increase of deactivation.

Ion and electron diffusion coefficients versus  $\theta_d$  dependences are shown in Figures 16 and 17, respectively. Both diffusion coefficients decrease as  $\theta_d$  increases. However, while  $D_e$  decreases almost linearly with the increase of  $\theta_d$ ,  $D_i$  versus  $\theta_d$  exhibits a break at about  $\theta_d = 0.3$ . Also,  $D_e$  values are nearly two orders of magnitude higher than  $D_i$  values. It is possible that electron hopping controls the charge-transport process at a POAP film in its oxidized state, where the polymer is swollen, which facilitates ion transport. However, in the present work, relative diffusion coefficient values ( $D_e > D_i$ ) refer to the reduced state of POAP. As was proposed from RDEV data, the decrease of  $D_e$  with the increase of  $\theta_d$  could be attributed to an increase of the hopping distance between remnant redox active sites after polymer deactivation. Although the Vorotyntsev's model gives  $D_e$  values near three orders of magnitude higher than  $D_i$  values extracted from RDEV, both  $D_e$  versus  $\theta_d$

dependences are linear. The interpretation of diffusion coefficients at polymer films depends on the model employed to describe the charge propagation and sometimes on the technique used in its measurement.

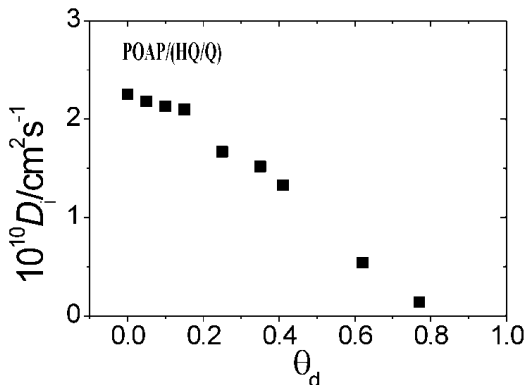


Figure 16. Ion diffusion coefficient ( $D_i$ ) as a function of  $\theta_d$ . Electrolyte: 0.1 M HClO<sub>4</sub> + 0.4 M NaClO<sub>4</sub> + 2 × 10<sup>-3</sup> M (HQ/Q) solution.

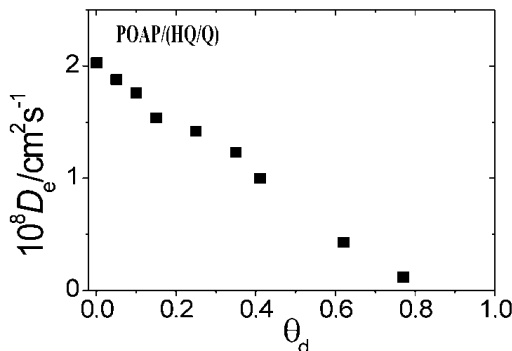


Figure 17. Electron diffusion coefficient ( $D_e$ ) as a function of  $\theta_d$ . Electrolyte: 0.1 M HClO<sub>4</sub> + 0.4 M NaClO<sub>4</sub> + 2 × 10<sup>-3</sup> M (HQ/Q) solution.

The break observed in the  $D_i$  versus  $\theta_d$  dependence at about  $\theta_d \sim 0.3$  also seems to be evident in the  $R_i^{\text{fls}}$  versus  $\theta_d$  dependence (Figure 14). Probe beam deflection measurements [35] suggest that while protons and anions are exchanged during POAP oxidation, insertion of protons is the dominant process during the POAP reduction process. Also, impedance measurements reported in [7] indicate that POAP is only doped with hydrogen ions and the effect of anions is negligible. Then, it is possible that both parameters  $R_i^{\text{fls}}$  and

$D_i$  are related to proton movements across the POAP|solution interface and inside the polymer film, respectively, rather than to anion transport. Concerning the proton movement into POAP films, the existence of two forms (mobile and bound) of hydrogen ions in the bulk film has been proposed [7]. It was suggested that in polymers derived from aromatic amines, hydrogen ions could be constrained by nitrogen atoms of polymer chains and do not contribute to the electrical conductance of the film, and another part of such constrained groups is able to dissociate producing the mobile form of hydrogen, which provides the film conductance. In other words, besides mobile protons, some traps for hydrogen ions within the bulk of the film may be present, which provides the binding of these protons with polymer film fragments. This proton conduction mechanism is similar to that proposed for ion transport in some solid-state materials [36], where ion movement occurs by a hopping process with the participation of two different types of sites. While some sites allow a fast ion diffusion process, other sites immobilize ions and do not allow ions to participate in the diffusion process. The existence of these different types of sites was explained in terms of different energy barriers [36]. In this regard, the slight increase in the  $R_i^{\text{fls}}$  versus  $\theta_d$  (the slight decrease in the  $D_i$  versus  $\theta_d$ ) dependence within the range  $0 < \theta_d < 0.3$  could be due to the inhibition of traps for hydrogen ions, which only causes a small ion conductivity change. However, the strong  $R_i^{\text{fls}}$  increase (more pronounced  $D_i$  decrease) for  $\theta_d > 0.3$  could be attributed to the inhibition of nitrogen-containing groups that provide the binding of hydrogen ions and at the same time are able to dissociate and give the mobile form of hydrogen that markedly contributes to the polymer conductivity.

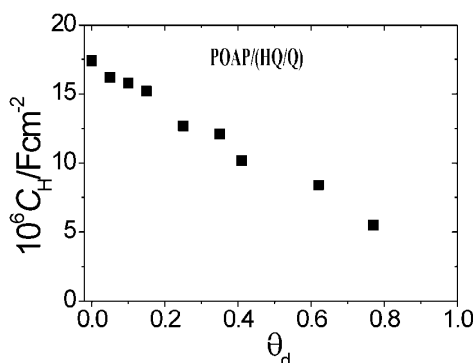


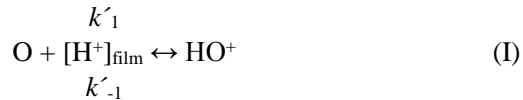
Figure 18. Interfacial capacitance  $C_H$  at the metal-polymer interface as a function of  $\theta_d$ . Electrolyte: 0.1 M  $\text{HClO}_4$  + 0.4 M  $\text{NaClO}_4$  +  $2 \times 10^{-3}$  M (HQ/Q) solution.

With regard to  $C_H$  values, starting from a value of around  $17.5 \mu\text{F cm}^{-2}$  for a nondeactivated film,  $C_H$  decreases almost linearly as the degree of deactivation increases, reaching a value of about  $5.5 \mu\text{F cm}^{-2}$  for  $\theta_d \sim 0.77$ . The  $C_H$  decrease, in the same way as the  $R_{\text{mif}}$  increase, could be assigned to the creation of inactive gaps in the redox site configuration at the polymer|metal interface with deactivation.

### **3.3. Impedance Measurements in the Sole Presence of the Supporting Electrolyte**

As was indicated, the model of Vorotyntsev et al. [23] also includes the impedance behavior of the polymer contacting the inactive electrolyte (absence of the redox couple in solution) by considering  $Z_e^{\text{fis}} \rightarrow \infty$  in Eq. (3). Charge transport and transfer parameters in the absence of the HQ/Q redox couple in solution were also obtained by fitting impedance diagrams in the sole presence of the supporting electrolyte by employing the model described in [23]. Impedance parameters not related to the presence of the redox couple in solution obtained by employing Eq. (3) are in coincidence with those extracted in the sole presence of the supporting electrolyte. However, it is often remarked that charge-transport parameter values extracted from impedance measurements depend on the model used to describe the charge propagation in electroactive materials. In this connection, the rate of charge transport in electroactive polymers is usually characterized by diffusion coefficient values, which can vary over several orders of magnitude ( $10^{-7}\text{-}10^{14} \text{ cm}^2 \text{ s}^{-1}$ ). The aim of this part of the work was to study the charge conduction process at POAP films employing a different impedance model to that described by Vorotyntsev et al. in [23] and then, compare charge-transport parameters obtained from both models. As the electroactivity of POAP is explained by a redox mechanism that involves an addition/elimination of protons coupled with a reversible electron transfer [6, 26], a modified electron hopping model, which considers a protonation reaction, developed by us in [37] was used to obtain charge-transport parameters of nondeactivated and deactivated POAP films in the sole presence of the supporting electrolyte solution. Although the model described in [37] is more limited than that described in [23], the charge-transport parameters obtained from both models were compared. As was indicated, the model given in [37] considers a

protonation reaction (Reaction (I) see below) coupled with a self-exchange process between oxidized and reduced sites (Reaction II, see below)



The analytical expression for the impedance derived in [37] is

$$Z(\omega) = R_{\text{Qt}} + (RT/nF^2Ac) [k_f + k_b(K+1)/K] A(\omega, D_e, k) \quad (8)$$

$R_{\text{Qt}}$  in Eq. (8) is a charge-transfer resistance (see also eq. (32) in [37]), which is given by the expression

$$R_{\text{Qt}} = (RT/nF^2Ac) [(k_f + k_b)(k_f k_b)^{-1} + 1/K k_f] \quad (9)$$

In Eqs. (8) and (9),  $A$  is the electrode area,  $c$  the volumetric redox site concentration, and  $K$  an equilibrium constant that can be explicitly written in terms of the solution  $pH$  as

$$K = (k'_1/k'_{-1}) K_p 10^{-pH} \quad (10)$$

$K$  also depends on the  $k'_1$  and  $k'_{-1}$  constants involved in step (I) and a partition coefficient  $K_p$ , which determines the ratio between the proton concentration inside the film ( $[\text{H}^+]_{\text{film}}$ ) and the actual proton concentration in solution ( $[\text{H}^+]_{\text{sol}}$ ), i.e.,

$$[\text{H}^+]_{\text{film}} = K_p [\text{H}^+]_{\text{sol}} \quad (11)$$

$k_f$  and  $k_b$  in Eq. (8) are the forward and backward electrochemical rate constants involved in step (II), respectively, and  $A(\omega, D_e, k)$  is a function of the frequency,  $\omega$ , which also contains an affective diffusion coefficient ( $D_e$ ) to describe the charge-transport process within the polymer film and the constant  $k = k'_{-1} + [\text{H}^+]_{\text{film}} k'_1$  (see eq. (33) in Ref. [37]).  $\text{OH}^+$  and  $\text{RH}$  (steps I and II) are the protonated oxidized and reduced forms of the polymer confined redox

couple, respectively. Other chemical equilibria following the self-exchange (II) were ignored in [37]. Concerning step (II), the electroactive centers OH<sup>+</sup> and RH can exchange electrons with the electrode at the metal/polymer interface following a Butler-Volmer kinetics, with  $k_f$  and  $k_b$  given by the expressions

$$k_f = k_{sh} \exp [b_f (E - E^{\circ})] \quad (12)$$

$$k_b = k_{sh} \exp [-b_b (E - E^{\circ})] \quad (13)$$

$E^{\circ}$  in expressions (12) and (13) is the standard potential of the redox couple,  $b_f$  and  $b_b$  are the Tafel coefficients,  $b_f = \alpha nF/RT$  and  $b_b = (1-\alpha) nF/RT$ , and  $k_{sh}$  is the electrochemical standard rate constant. The other constants have their usual meanings.

The redox centers are uniformly distributed throughout the polymer with a total concentration,  $c$ , given by

$$c = [\text{O}] + [\text{HO}^+] + [\text{RH}] \quad (14)$$

Eq. (8) was employed to fit experimental impedance diagrams of nondeactivated and deactivated POAP films in the presence of the supporting electrolyte. Deactivation by storage times was considered to only affect the charge-transfer process at the metal/polymer interface ( $R_{Qt}$ ) and the charge-diffusion process ( $D_e$ ) within the polymer film. As the solution *pH* and electrolyte composition remain constant, the other parameters of the model were assumed to be independent of the deactivation process, and values for nondeactivated POAP films obtained in [37] were employed.

Nyquist diagrams at the reduced state ( $E = -0.2$  V) for a nondeactivated POAP film and deactivated films in contact with a 0.1 M HClO<sub>4</sub> + 0.4 M NaClO<sub>4</sub> solution, are compared in Figure 19 (see discrete points). The early increase in the imaginary component of the impedance and the absence of any semicircle at high frequency for a nondeactivated film are indicative of a fast interfacial charge-transfer process. However, a well-defined high-frequency semicircle is observed in the impedance diagrams of POAP films stored for prolonged time periods. As the storage time increases, the high-frequency semicircle is more pronounced. As was indicated, the increase in the size of the high-frequency semicircle in Nyquist plots is indicative of a restriction in the charge-propagation process across the gold/POAP/solution system.

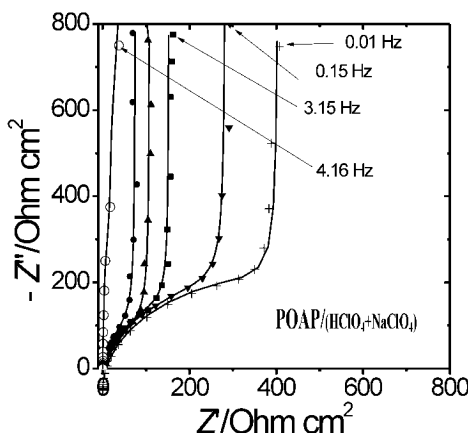


Figure 19. Nyquist diagrams for (O) a nondeactivated POAP film and for the deactivated films  $\theta_d$ : 0.05 (●); 0.10 (▲); 0.15 (■); 0.35 (▼); 0.41 (+).  $E = -0.2$  V. Discrete points are experimental data and continuous lines represent the fitting by using de model described in [37]. Electrolyte: 0.1 M HClO<sub>4</sub> + 0.4 M NaClO<sub>4</sub>. Thickness of the POAP film: 60 nm.

Continuous lines on the Nyquist plots shown in Figure 19 are simulated curves calculated by using Eq. (8). A good fitting was observed for all impedance diagrams. In the same way as in the previous model, the fitting procedure by using Eq. (8) was based on the CNLS (Complex Nonlinear Squares) method. A rigorous fitting procedure was performed where the error structure was assessed following the references [30-33]. Continuous lines in Figure 19 represent the weighted complex nonlinear least-squares fit to the data.

In the simulations the following parameter values were considered as known and constants: number of transferred electrons,  $n$  (= 0.44 [24]); polymer thickness,  $\phi_p$  (= 60 nm [17, 18]); total redox site concentration,  $c$  (=  $4.7 \times 10^{-3}$  mol cm<sup>-3</sup> [1]);  $E^\circ$  (= 0.015 V versus SCE [24]);  $K$  (= 0.085 for  $pH$  1 [37]) and  $k$  (= 0.18 s<sup>-1</sup>) [37]. Then, the remnant-parameters contained in Eq. (8), i.e.,  $k_{sh}$  and  $D_e$ , were calculated from experimental impedance data by the fitting procedure described above. Although the parameter  $k_{sh}$  varied without restraints during the fitting, for POAP film thickness ( $\phi_p$  = 60 nm) and solution  $pH$  = 1, used in this work,  $D_e$  was allowed to vary within the range  $10^{-7}$ – $10^{-11}$  cm<sup>2</sup> s<sup>-1</sup>.  $D_e$  values lower than  $10^{-11}$  cm<sup>2</sup> s<sup>-1</sup> were considered unrealistic for thick POAP films. A contribution of the interfacial capacitance,  $C_H$ , considered as a fitting parameter, was included in order to represent the actual impedance diagrams from the calculated ones.

**Table 3. Standard electrochemical rate constant values for deactivated POAP films extracted from the impedance model given in [37]**

<sup>a</sup> POAP films	<sup>b</sup> $10^5 k_{sh}$ /cm s <sup>-1</sup>	<sup>c</sup> $\theta_d$
1	10.5	0.05
2	3.09	0.10
3	3.11	0.15
4	2.04	0.25
5	1.97	0.35
6	1.48	0.41
7	0.67	0.62
8	0.46	0.77

<sup>a</sup> Numbers 1 to 8 represent different deactivated POAP films

<sup>b</sup> Values of the standard electrochemical rate constant,  $k_{sh}$ , for the different degrees of deactivation given in column 3. The value of  $k_{sh}$  for a nondeactivated film extracted from the fitting using Eq. (8) is  $2.7 \times 10^5$  cm s<sup>-1</sup>

<sup>c</sup> Degree of deactivation of each one of the POAP films after storage for the time periods indicated in column 2 of Table 1. The degree of deactivation was calculated from  $\theta_d = 1 - (Q_{Red,c}/Q_{Red,T})$ , where  $Q_{Red,T}$  ( $= 2.8$  mC cm<sup>-2</sup>) is the voltammetric reduction charge of a nondeactivated film

The dependence of the electrochemical standard rate constant ( $k_{sh}$ ) on the degree of deactivation extracted from the fitting procedure is shown in Table 3. As can be seen from Table 3,  $k_{sh}$  decreases as the POAP film becomes more deactivated with the storage time. Similar  $k_{sh}$  values for deactivated POAP films shown in Table 3 were previously reported for POAP in [24]. In this regard, low values of  $k_{sh}$  reported in previous work could indicate partial deactivation of the polymer. However, high  $k_{sh}$  values ( $2.7 \times 10^5$  cm s<sup>-1</sup>) such as that obtained in this work from impedance diagrams for a nondeactivated film (see notes at the foot of Table 3), which do not show an appreciable high-frequency semicircle (Figure 19), should correspond to a polymer matrix relatively free of deactivated zones. The  $R_{Qt}$  versus  $\theta_d$  dependence, extracted from  $k_{sh}$  values given in Table 3, is represented in Figure 20. As can be seen by comparing Figure 20 with Figure 13, the  $R_{Qt}$  versus  $\theta_d$  dependence extracted from the model given in [37] is in good coincidence with the  $R_{m/f}$  versus  $\theta_d$  dependence obtained from the model described in [23].

As was indicated, although electron hopping is believed to be the mechanism for electron transport at polymer materials, it is also possible that ion motions may partially or totally control the rate of charge transport. Then,

$D_e$  obtained with the model derived in [37] can be considered as an effective or binary diffusion coefficient value. As can be seen by comparing  $D_e$  versus  $\theta_d$  dependence extracted employing the model described in [37] (Figure 21) with  $D_i$  and  $D_e$  values extracted from Vorotyntsev's model (Figures 16 and 17, respectively), the order of magnitude of  $D_e$  obtained from the model developed in [37] is closer to that of  $D_i$  than to that of  $D_e$  extracted from the model given in [23]. This observation seems to be consistent with the assumption that ion transport controls the whole charge-transport process at POAP. However,  $D_e$  values obtained from the impedance model given in [37] again are one order of magnitude higher than  $D_e$  values extracted from RDEV.

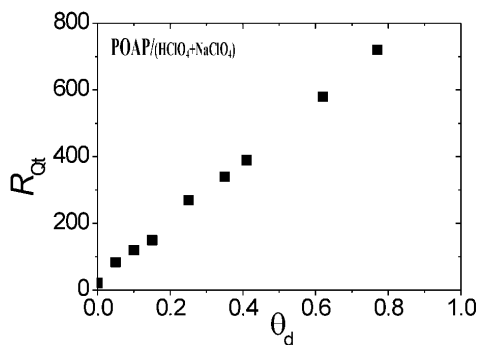


Figure 20.  $R_{Q_t}$  versus  $\theta_d$  dependence extracted employing the model described in [36]. Electrolyte: 0.1 M HClO<sub>4</sub> + 0.4 M NaClO<sub>4</sub> + 2 × 10<sup>-3</sup> M (HQ/Q) solution.

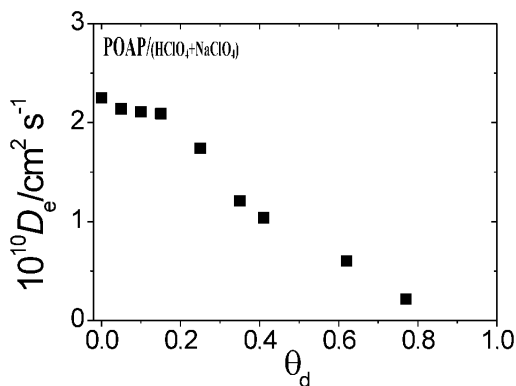


Figure 21. Diffusion coefficient  $D_e$  versus  $\theta_d$  dependence extracted employing the model described in [36]. Electrolyte: 0.1 M HClO<sub>4</sub> + 0.4 M NaClO<sub>4</sub> + 2 × 10<sup>-3</sup> M (HQ/Q) solution.

The storage without use for prolonged time periods could alter the molecular structure of a POAP film, and, hence, its physical properties. Thus, parameters obtained in this work from impedance models strictly represent fitting parameters of the model rather than real physical properties of the polymer. Even though one cannot expect a complete coincidence of the electrochemical properties of the polymer film with those predicted by the theory, a qualitative agreement might be expected, especially in order to compare the behaviors of films before and after they have been stored for prolonged time periods.

## 4. SURFACE RESISTANCE MEASUREMENTS

Although charge-transport parameters of electroactive polymers are usually obtained employing traditional techniques such as, CV, RDEV and EIS, some experiments employing a non-traditional technique, the surface resistance (SR), were carried out in this work in order to study the POAP deactivation after storage. It is interesting to remark that conversely to other techniques, such as EIS, which is based on complicated models, the SR technique is based on a simple electron dispersion model [38, 39]. The SR technique is sensitive to the distribution of scatterers at a metal film surface [12]. In previous works it was proved that SR is a useful technique to detect changes in the redox sites distribution during the redox switching of a POAP film deposited on a thin gold film [13, 40]. However, as the SR technique may be considered as a non-traditional approach in Electrochemistry, a brief explanation about the interpretation of the resistance changes exhibited by a thin metal film coated with an electroactive polymer film is given in the next paragraphs.

### 4.1. Electronic Transport in Thin Metal Films

Electronic transport in thin metal films is strongly affected by interfacial phenomena. For example, the scattering of conduction electrons at planar interfaces defined by the top and bottom surfaces of the film under study can contribute significantly to the resistivity. In the case of thin metal films, the electrical resistivity  $\rho_f$  is higher than the bulk resistivity  $\rho_m$  of the massive

metal of the same structure as the metal film and the  $\rho_f/\rho_m$  ratio decreases with increasing the film thickness,  $\phi_m$ . This “Size Effect” becomes evident when  $\phi_m$  is comparable with the mean free path,  $l_m$ , of the conduction electrons. The theory to account for the size effect was postulated by Fuchs [39, 38] and Sondheimer [39]. The exact expression for the dependence of the film resistivity,  $\rho_f$ , as a function of  $\phi_m$  is complicated. However, it can be reduced to a limiting form when  $\phi_m/l_m \geq 1$ :

$$\rho_f / \rho_m = 1 + (3/8) (1-p) l_m / \phi_m \quad (15)$$

In Eq. (15), p is the specularity parameter [39]. This parameter represents the probability of an electron being reflected specularly or diffusely at the film surface. The p value ranges from 0 for complete diffuse scattering to 1 for complete specular scattering. At first, it should be considered that thin metal films can be prepared to satisfy the Fuch's model in a sufficient way to exhibit a specularity parameter near 1 (a surface with a smooth mirrorlike finish which is free of defects). However, this parameter, which is also interpreted as the fraction of the surface which specularly reflects electrons, depends on the quality of the metal film surface, that is, on the method of preparation of the metal film [41]. In this sense, an appreciable fraction of the conduction electrons can be scattered diffusely and give rise to an additional resistance, which correlates with roughness of surface topography and the presence of surface defects. All these imperfections should lead to experimental p values lower than 1.

Besides factors above mentioned if foreign entities are present on the film surface, translational symmetry parallel to the interface, changes and additional scattering of the conduction electrons occurs. This electron dispersion effect brought about by the presence of entities on the metal surface, thereby acting as dispersion centres for the surface reflection of the electrons from the inside of the metal, has been analysed on the basis of Eq. (15). Assuming that the specularity, p, is the principal parameter influenced by the surface concentration of foreign scattering centres at the film surface  $\Gamma_{\text{surf}}$ , differentiation of Eq. (15) leads to the relationship:

$$\Delta\rho_f = - 3/8 (\rho_m l_m / \phi_m) (\Delta p) \quad (16)$$

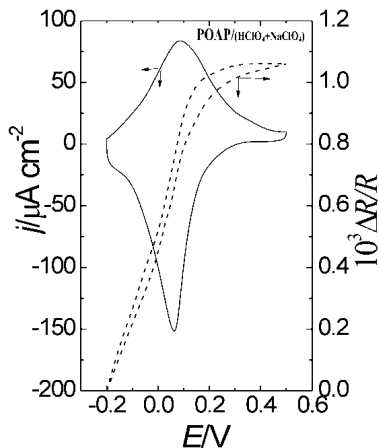


Figure 22. Simultaneous  $\Delta R/R$ -E and  $j$ -E responses of a 30 nm thick gold film coated with a 2.8  $mC\text{ cm}^{-2}$  ( $\phi_p = 60$  nm) thick POAP film. Electrolyte: 0.1 M  $HClO_4 + 0.4$  M  $NaClO_4$ . Scan rate:  $v = 0.01$  V  $s^{-1}$ .

On the assumption that the increase of  $\Gamma_{Surf}$  increases the diffuse scattering of the electrons,  $\Delta p = -k \Gamma_{Surf}$ , an increase  $\Delta p_f$  would be expected with increasing  $\Gamma_{surf}$  (Eq. (16)). In terms of the resistance changes ( $\Delta R = \Delta p_f G/\phi_m$ ), Eq. (16) can be written as:

$$\Delta R = -3/8 G (\rho_m l_m / \phi^2 m) \Delta p \quad (17)$$

## 4.2. The POAP-Coated Gold Film Electrode

As was described in the experimental section, POAP was deposited on a thin gold film electrode whose thickness was of the order of the mean free path of conduction electrons of gold and SR was employed to investigate changes in the electronic properties at the gold/POAP interface during deactivation of the polymer. Simultaneous voltammetric and SR responses corresponding to a nondeactivated POAP film within the potential range comprised between -0.2 V and 0.5 V are shown in Figure 22.

As was indicated, the POAP film maintains these responses even after storage without use for a time period of 30 h. However, after a higher storage time these responses start to change. The evolution of the  $\Delta R/R$  vs.  $E$  response for a 60 nm thick POAP film with the storage time is shown in Figure 23. Simultaneously with the  $\Delta R/R$  vs.  $E$  response, the evolution of the

voltammetric response was also recorded for each POAP film. As the electrode area and the thickness of the POAP films employed in SR were the same as those used in CV, RDEV and EIS measurements, the evolution of the voltammetric response with storage was practically the same as that shown in Figure 1.

With regard to  $\Delta R/R$  vs.  $E$  response, the potential drop along the thin gold film electrode was compensated at the reduced state of POAP ( $E = -0.2\text{ V}$ ) (see experimental section). Then, an increase in the SR of the POAP-coated gold electrode is recorded in going from  $-0.2\text{ V}$  to  $0.5\text{ V}$ . The increase of the gold film resistance during the transition from the reduced state to the oxidized state of a nondeactivated POAP film (Figure 22), was explained in terms of the generation of electronic entities at the polymer chains near the electrode surface, which occurs by electron transfer across the polymer|metal interface [12]. In this connection, the redox switching of POAP was interpreted in terms of the oxidation of the amino groups to imine [6]. It is not unreasonable to expect that imine sites act themselves as different scattering centres compared with amine sites, increasing in this way the diffuse reflection of conduction electrons on the gold surface during POAP oxidation (increase of the resistance) [40]. That is, the  $\Delta R/R$  increase in going from  $E = -0.2\text{ V}$  to  $E = 0.5\text{ V}$  in Figure 22 can be explained in terms of a  $p$  decrease (Eq. (17)). Respect to the polymer redox conversion at the gold film surface, one has to keep in mind that the resistance changes at metal films are not the direct result of the electron transfer between the species on the metal film surface and the metal but they rather originate from the effect of foreign surface entities on the conduction electrons of the metal itself. On the other hand, as the potential drop along the resistive electrode ( $R \sim 20.02\text{ ohm}$  for  $\phi_m = 30\text{ nm}$ ) due to the measuring current  $I_m$  (see experimental section) is compensated only  $\Delta R$  changes associated to interfacial phenomena are recorded. Thus, the measured resistance change for a POAP-coated gold film electrode is only related to an interfacial (metal|polymer) electron dispersion process occurring during the reduction-oxidation process of the polymer film.

The increase of  $\Delta R/R$  during POAP oxidation can be explained in terms of an interfacial distribution of scatterers (imine sites) in the oxidised state with a spacing among them larger than that corresponding to amine sites in the reduced state [6, 12]. That is, the distribution of imine species in the oxidized state of POAP should be less compact than the corresponding distribution of amine species in the reduced state, which should lead to a more diffuse reflection of conduction electrons at the gold|POAP interface (lower

specularity parameter at the oxidized state as compared with the value at the reduced one ( $p_{\text{ox}} < p_{\text{red}}$ ) [12]. A confirmation that supports a more extended configuration of oxidized sites, as compared with that of reduced ones, at POAP can be given in terms of gaps, which appear during POAP oxidation. In this respect, optical measurements on POAP films reveal that only one in every four or five amine sites is converted to the corresponding imine site [6]. Thus, the existence of inactive gaps within the distribution of oxidized sites of POAP could justify that POAP in its oxidized state reflects conduction electrons of gold more diffusely than in its reduced state. Further confirmation about the different reflecting properties of the oxidized and reduced states of POAP can be found in the different values of the site interaction parameters ( $r$ ) obtained from the cathodic and anodic voltammetric response of POAP. A nonideal behaviour of POAP, which is actually expected considering the rather high concentration of active sites in the film (*i.e.*,  $c = 4.7 \text{ M}$  [1, 2]), leads to the following values of anodic and cathodic site interaction parameters:  $r_a = -0.55 \text{ M}^{-1}$  and  $r_c = -0.18 \text{ M}^{-1}$ , respectively. Both are negative, thus involving a repulsive energy of interaction. As a higher repulsion is observed between oxidized sites than between reduced ones at POAP, a more extended configuration of oxidized sites should be expected as compared with the corresponding distribution of reduced sites.

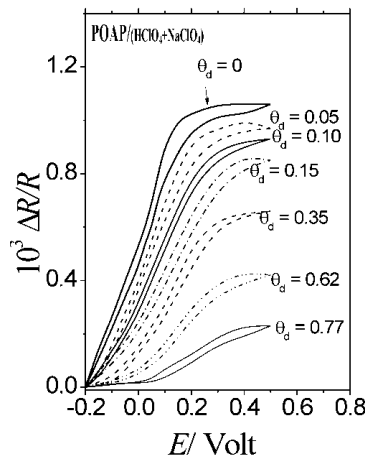


Figure 23.  $\Delta R/R$ - $E$  responses obtained simultaneously with the ( $j$ - $E$ ) responses shown in Figure 1. The degrees of deactivation are indicated in the figure (see also Table 1). Thickness of the gold film  $\phi_m = 30 \text{ nm}$ , resistance value of the gold film,  $R = 20.02 \text{ ohm}$ . Thickness of the POAP film,  $\phi_p = 60 \text{ nm}$ . Electrolyte:  $0.1 \text{ M HClO}_4 + 0.4 \text{ M NaClO}_4$ . Scan rate:  $v = 0.01 \text{ V s}^{-1}$ .

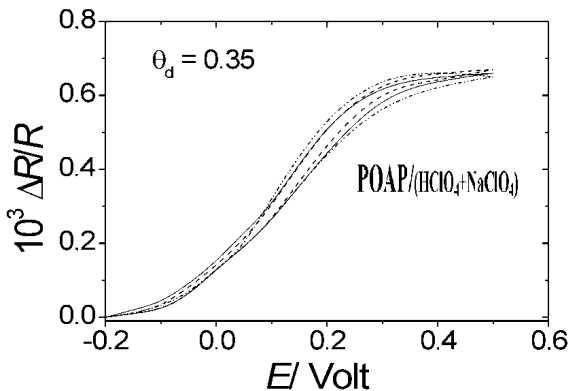


Figure 24.  $\Delta R/R$ - $E$  responses of a deactivated POAP film ( $\theta_d = 0.35$ ) deposited on a 30 nm thick gold film. Thicknesses of the POAP films: (---)  $\phi_P = 69$  nm; (—)  $\phi_P = 60$  nm; (—•—)  $\phi_P = 52$  nm. Electrolyte: 0.1 M HClO<sub>4</sub> + 0.4 M NaClO<sub>4</sub>. Scan rate:  $v = 0.01$  V s<sup>-1</sup>.

With regard to POAP deactivation after storage, as can be seen from Figure 23, the more deactivated becomes the POAP film the more attenuated is the  $\Delta R/R$  change in going from the reduced to the oxidized state of POAP. As was indicated, the measured resistance change is only related to an interfacial (metal|polymer) electron dispersion process which occurs during reduction-oxidation of the polymer film. This fact was proved by changing the POAP film thickness (Figure 24). Figure 24 shows that increasing the POAP film thickness between 50 nm to 69 nm, the  $\Delta R/R$  change remains practically the same. Obviously, the voltammetric responses (not shown) depend on the POAP thickness. However, the  $\Delta R/R$  vs.  $E$  change, at constant POAP film thickness, depends on the gold film thickness (Figure 25). That is, as the thinner is the gold film (see Eq. (17)) the higher is the  $\Delta R$  value, and then, the more pronounced becomes the resistance  $\Delta R/R$  change (compare Figures 23 and 25 for the same  $\theta_d$  values). Although the absolute resistance value,  $R$  increases as the metal film thickness decreases, the interfacial effects in the  $\Delta R/R$  change become magnified as the thickness of the gold film decreases. In this regard, as the lower is the metal film thickness, more sensitive the SR technique becomes to study interfacial phenomena. This effect is quantitatively shown in Figure 26, where the maximum  $\Delta R/R$  change in going from -0.2 V to 0.5 V was represented as a function of the degree of deactivation of the POAP film for two different gold film thicknesses.

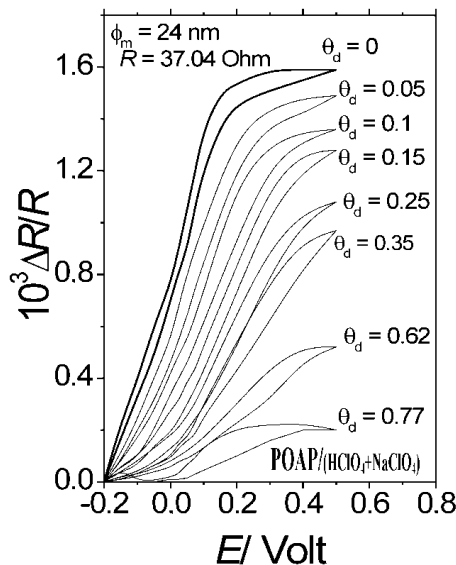


Figure 25.  $\Delta R/R-E$  responses of a POAP-coated gold film electrode. Thickness of the POAP film,  $\phi_p = 60$  nm. Thickness of the gold film  $\phi_m = 24$  nm, resistance value of the gold film,  $R = 37.04$  ohm. ( $\theta_d = 0$ ) A nondeactivated POAP film. Curves with  $\theta_d$  values higher than 0 correspond to different deactivated POAP films indicated in Table 1. Electrolyte: 0.1 M HClO<sub>4</sub> + 0.4 M NaClO<sub>4</sub>. Scan rate:  $v = 0.01$  V s<sup>-1</sup>.

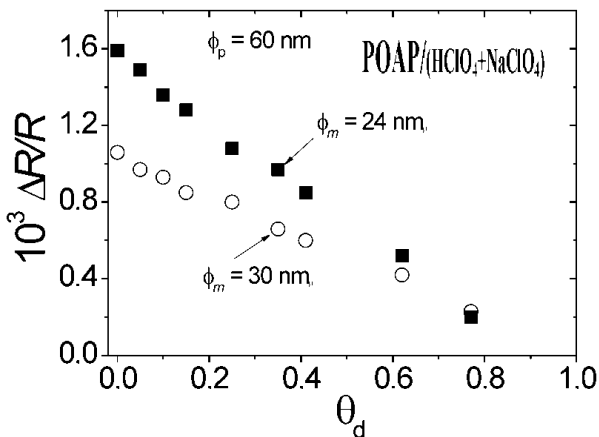


Figure 26. Maximum  $\Delta R/R$  change in going from the reduced to the oxidized state of POAP as a function of the degree of degradation,  $\theta_d$ . Thickness of the POAP film,  $\phi_p = 60$  nm. Thickness of the gold film,  $\phi_m$ : (O) 30 nm; (■) 24 nm.

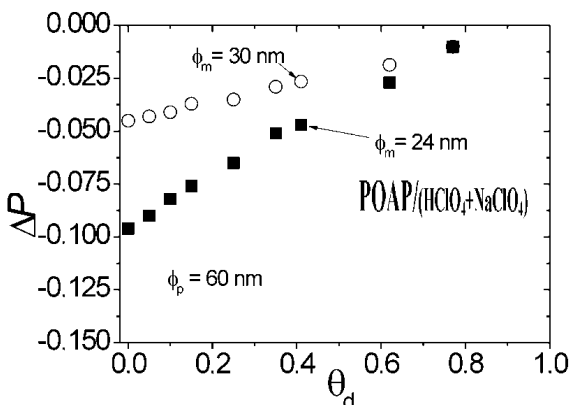


Figure 27. The  $\Delta p$  vs  $\theta_d$  dependence for the different gold film thicknesses:  $\phi_m = 30$  nm;  $\phi_m = 24$  nm. The corresponding resistances are:  $R = 20.02$  ohm;  $R = 37.04$  ohm.

Although the absolute values of the specularity parameters at the reduced and oxidized state of POAP at each degree of deactivation are unknown (both parameters should depend on the degree of POAP deactivation), by employing Eq. (17), one can obtain the specularity parameter change ( $\Delta p$ ) in going from the reduced to the oxidized state of POAP at each degree of deactivation. The  $\Delta p$  vs.  $\theta_d$  dependences for the two different gold film thickness indicated in Figure 26 are shown in Figure 27. The following values were employed in Eq. (17) to calculate  $\Delta p$ :  $l_m$  (= 22 nm at 25°C) is the mean free path of the conduction electrons of gold,  $\rho_m$  (=  $2.4 \times 10^{-6}$  ohm cm) is the bulk resistivity of the massive metal (gold) of the same structure as the metal film,  $\phi_m$  is the thickness of the metal film,  $G$  (= 2) is the relationship between the length  $l$  and the width  $w$  of the rectangular gold film on which the POAP film was deposited. The resistance values  $R$  of the gold films are experimentally obtained. As was indicated,  $\Delta p$  is always negative, that is,  $p_{ox} < p_{red}$ . However, as can be seen Figure 27, as the degree of deactivation increases,  $\Delta p$  tends to increase. The maximal difference in the reflecting properties of the POAP/gold interface for the conduction electron of gold between the reduced and the oxidized states of POAP occurs for a nondeactivated POAP film, however, the reflecting properties of the POAP/gold interface at the reduced and oxidized state of POAP tend to match as the degree of deactivation increases. This finding seems to be indicative of a redox sites distribution that changes as the polymer becomes more deactivated. This change in the redox site distribution could explain the change in the electron hopping distance between redox sites,

as is proposed in RDEV and EIS measurements to explain the changes of the charge-transport parameters (i.e., diffusion coefficients) with the degree of deactivation. As can be seen from Figure 27, again as the lower is the thickness of the gold film, the more pronounced becomes the  $\Delta p$  change at the gold/POAP interfaced at each degree of deactivation. As was indicated, this effect is due to the higher sensitivity of the SR technique to detect surface phenomena as the metal film thickness decreases.

At this point a comparison between  $R_{m|f}$  and  $\Delta R/R$  changes with the degree of deactivation (Figures 13 and 26, respectively) can be established. While the increase of  $R_{m|f}$  during the deactivation of the polymer film should be associated with a transversal resistance due to the electron transfer across the polymer/metal interface, the  $\Delta R/R$  decrease with POAP deactivation can be attributed to the scattering of conduction electrons from the inside of the metal to the metal/polymer interface, caused by changes in the translational symmetry parallel to the interface due to the presence of a different distributions of redox sites at the interface. Despite both resistances should be associated to the redox sites distribution at the metal/POAP interface, it should be taken into account that the while  $\Delta R/R$  change (-0.2 V to 0.5 V) is obtained from a potentiodynamic technique (CV)  $R_{m|f}$  is extracted at the reduced state of POAP employing EIE. Then, while the increase of  $R_{m|f}$  should be associated to an increase of the amount of inactive redox sites at the reduced state during POAP deactivation, the  $\Delta R/R$  decrease could be attributed to the change of the reflecting properties of the redox sites distributions at the reduced and oxidized states of POAP for the conduction electrons of the gold film which tend to match as the polymer becomes more deactivated.

## CONCLUSION

In this work it is demonstrated that poly(o-aminophenol) films maintain their conducting properties unaltered even after a storage time without use of one day. However, a loss of conductivity was observed as the storage time was extended beyond 30 h. This loss of conductivity was studied by CV, RDEV, EIS and SR measurements. An attenuation of the voltammetric response of POAP is observed with the increase of the storage time. This attenuation allows one to define a degree of deactivation of the polymer. Dependences of conduction parameters on the degree of deactivation were obtained in the presence of an electroactive solution employing RDEV and *ac* impedance

measurements. The electron hopping model was employed to interpret RDEV experiments. EIS data were interpreted on the basis of a model which allows one to explain both ionic and electronic interfacial exchange across the POAP/solution interface. EIS data obtained in the only presence of the supporting electrolyte were interpreted employing a modified electron-hopping model, which considers a protonation reaction coupled with a self-exchange process between oxidized and reduced sites. Parameters extracted from both models were compared. While electron ( $D_e$ ) and ion ( $D_i$ ) diffusion coefficients decrease, interfacial resistances ( $R_{m|f}$ ,  $R_i^{fs}$ ,  $R_e^{fs}$ ) increase as the degree of deactivation of the polymer increases. The slower electron transport with the increase in the degree of deactivation was attributed to the increase of the electron hopping distance between redox sites. While parameters representing electron motion extracted from RDEV and impedance measurements seem to change continuously within the whole range of deactivation degree, parameters representing the ion transport show a break at a degree of deactivation of about 0.35. This characteristic of the ion transport at POAP was associated with the existence of two forms of hydrogen ions in the POAP film.

The relative surface resistance change of a thin gold film coated with poly(*o*-aminophenol) is gradually attenuated with the increase of the storage time. The surface resistance change in going from the reduced to the oxidized state of POAP was attributed to a change from specular to diffuse scattering of conduction electrons from the inside of the gold film to the POAP/gold film interface. The attenuation of the surface resistance change as the degree of deactivation of POAP increases was attributed to a change in the redox site configuration, which seems to be in agreement with the increase in the electron hopping distance between redox sites, proposed to explain the decrease of diffusion coefficient values obtained from RDEV and EIS measurements with the increase of the degree of deactivation.

## ACKNOWLEDGMENTS

The author gratefully acknowledges the Consejo Nacional de Investigaciones Científicas y Técnicas (CONICET) and also the Facultad de Ciencias Exactas, National University of La Plata (UNLP).

**Conflict of interest:** The author declares that he has no conflict of interest.

## REFERENCES

- [1] Barbero, C.; Silber, J.J.; Sereno, L. (1990). Electrochemical properties of poly(o-aminophenol) modified electrodes in aqueous acid solutions. *J. Electroanal. Chem.* 291: 81-101.
- [2] Barbero, C.; Silber, J.J.; Sereno, L. (1989). Formation of a novel electroactive film by electropolymerization of *ortho*aminophenol. Study of its chemical structure and formation mechanism. Electropolymerization of analogous compounds. *J. Electroanal. Chem.* 263: 333-352.
- [3] Ohsaka, T.; Kunimura, S.; Oyama, N. (1988). Electrode Kinetics of Poly(*o*-aminophenol) Film Prepared by Electrooxidative Polymerization of Aminophenol and its Electrochromic Propertes. *Electrochim. Acta*. 33: 639-645.
- [4] Tucceri, R.; Arnal, P.M.; Scian, A.N. (2013). Poly(*o*-aminophenol) film electrodes. Synthesis and characterization. Formation mechanisms. A review article. *Canadian Journal of Chemistry*, 91: 91-112.
- [5] Scolari, D.; R. Tucceri, R. (2011). Some applications of nonconducting poly(*o*-aminophenol) films in Bioelectrochemistry and Electrocatalysis. *Micro and Nanosystems*, 3: 115-130.
- [6] Tucceri, R.I.; Barbero, C.; Silber, J.J.; Sereno, L.; Posadas, D. (1997). Spectroelectrochemical Study of Poly(*o*-aminophenol). *Electrochim. Acta*, 42: 919-927.
- [7] Levin, O.; Kondratiev, V.; Malev, V. (2005). Charge transfer processes at poly-*o*-phenylenediamine and poly-*o*-aminophenol films. *Electrochim. Acta*. 50: 1573-1585.
- [8] Miras, M.C.; Badano, A.; Bruno, M.M.; Barbero, C. (2003). Nitric oxide electrochemical sensors based on hybrid films of conducting polymers and metal phtalocyanines. *Portugaliae Electrochimica Acta*, 21: 235-243.
- [9] Yano, J.; Kawakami, H.; Yamasaki, S.; Kanno, Y. (2001). Cation capture ability and the potential response of a poly(*o*-aminophenol) film electrode to dissolved ferric ions. *J. Electrochem. Soc.* 148: E61-E65.
- [10] Lobo, M.J.; Miranda, A.J.; López-Fonseca, J.M.; Tuñón, P. (1996). Electrocatalytic detection of nicotinamide coenzymes by poly(*o*-aminophenol) and poly(*o*-phenylenediamine)-modified carbon paste electrode. *Analytica Chimica Acta*, 325: 33-42.

- [11] Zhang, A.Q.; Cui, C.Q.; Lee, J.Y. (1996). Metal-polymer interaction in the Ag<sup>+</sup>/poly-*o*-aminophenol system. *J. Electroanal. Chem.* 413: 143-151.
- [12] Tucceri, R. (2004). A review about the surface resistance technique in electrochemistry. *Surface Science Reports*, 56: 85-157.
- [13] Tucceri, R.I. (2001). Surface resistance measurements on thin gold film electrodes coated with poly(*o*-aminophenol) films. *J. Electroanal. Chem.* 505: 72-84.
- [14] Chopra, K.L. (1969). *Thin Film Phenomena*, McGraw-Hill Co., New York.
- [15] Tucceri, R.I.; Posadas, D. (1985). A surface conductance study of the anion adsorption on gold. *J. Electroanal. Chem.* 191: 387-399.
- [16] Tucceri, R.I.; Posadas, D. (1983). Resistive behaviour of thin gold film electrodes under direct current polarization. *J. Electrochem. Soc.* 130: 104-107.
- [17] Barbero, C.; Zerbino, J.; Sereno, L.; Posadas, D. (1987). Optical Properties of Electropolymerized *Ortho*aminophenol. *Electrochim. Acta*, 32: 693-697.
- [18] Bonfranceschi, A.; Pérez Córdoba, A.; Keunchkarian, S.; Zapata, S.; Tucceri, R. (1999). Transport across poly(*o*-aminophenol) modified electrodes in contact with media containing redox active couples. A study using rotating disc electrode voltammetry. *J. Electroanal. Chem.* 477: 1-13.
- [19] Tucceri, R.I.; Posadas, D. (1981). Theoretical approach to the resistive behaviour of thin solid film electrodes under direct current polarization. *J. Electrochem. Soc.* 128: 1478-1483.
- [20] Andrieux, C.P.; Savéant, J.M. (1980). Electron transfer through redox polymers films. *J. Electroanal. Chem.* 111: 377-381.
- [21] Laviron, E. (1980). A multilayer model for the study of spaced distribute redox modified electrodes. Part 1. Description and discussion of the model. *J. Electroanal. Chem.* 112: 1-9.
- [22] Deslouis, C.; Tribollet, B. (1992). *Advances in Electrochemical Science and Engineering*, Gerischer, H.; Tobias, C. Eds., VCH Publishers, New York, USA, vol. 2, pp. 205.
- [23] Vorotyntsev, M.A.; Deslouis, C.; Musiani, M.M.; Tribollet, B.; Aoki, K. (1999). Transport across an electroactive polymer film in contact with media allowing both ionic and electronic interfacial exchange. *Electrochim. Acta*, 44: 2105-2115.

- [24] Barbero, C.; Tucceri, R.I.; Posadas, D.; Silber, J.J.; Sereno, L. (1995). Impedance characteristics of poly(o-aminophenol) electrodes. *Electrochim. Acta*, 40: 1037-1040.
- [25] Chidsey, Ch.E.D.; Murray, R.W. (1986). Redox capacity and direct current electron conductivity in electroactive materials. *J. Phys. Chem.* 90: 1479-1484.
- [26] Komura, T.; Ito, Y.; Yamaguti, T.; Takahasi, K. (1988). Charge-transport process at poly(o-aminophenol) film electrodes: electron hopping accompanied by proton Exchange. *Electrochim. Acta*, 43: 723-731.
- [27] Albery, W.J.; Boutelle, M.G.; Hillman, A.R. (1985). The mechanism of faradaic reactions at the thionine coated electrode. *J. Electroanal. Chem.* 182: 99-111.
- [28] Tucceri, R. (2013). The metal/electroactive polymer interface studied by surface resistance. *J. of Surface and Engineered Materials and Advanced Technology*, 3: 205-216.
- [29] Vorotyntsev, M.A. (2002). Impedance of thin films with two mobile charge carriers, interfacial exchange of both species with adjacent media. Effect of the double layer charge. *Electrochim. Acta*, 47: 2071-2079.
- [30] Agarwal, P. Orazem, M.E., García-Rubio, L.H. (1992). Measurement models for electrochemical impedance spectroscopy. 1. Demonstration of applicability. *J. Electrochem. Soc.* 139: 1917-1927.
- [31] Agarwal, P.; Crisalle, O.D.; Orazem, M.E.; García-Rubio, L.H. (1995). Application of measurement models to impedance spectroscopy. II. Determination of the stochastic contribution to the error structure. *J. Electrochem. Soc.* 142: 4149-4158.
- [32] Agarwal, P.; Orazem, M.E.; García-Rubio, L.H. (1995). Application of measurement models to impedance spectroscopy. III. Evaluation of consistency with Kramer-Kronig relations. *J. Electrochem. Soc.* 142: 4159-4168.
- [33] Orazem, M.E. (2004). A systematic approach toward error structure identification for impedance spectroscopy. *J. Electroanal. Chem.* 572: 317-327.
- [34] Musiani, M.M. (1990). Characterizaton of electroactive polymer layers by electrochemical impedance spectroscopy (EIS). *Electrochim. Acta*, 35: 1665-1670.

- [35] Salavagione, H.J.; Arias-Padilla, J.; Pérez, J.M.; Vázquez, J.L.; Morallón, E.; Miras, M.C.; Barbero, C. (2005). Study of the redox mechanism of poly(o-aminophenol) using in-situ techniques: evidence of two redox processes. *J. Electroanal Chem.* 576: 139-145.
- [36] Bisquert, J. (2002). Analysis of kinetics of ion intercalation: ion trapping approach to solid-state relaxation processes. *Electrochim. Acta*, 47: 2435-2449.
- [37] Rodríguez Nieto, F.J.; Tucceri, R.I. (1996). The effect of *pH* on the charge transport at redox polymer-modified electrodes: an *ac* impedance study applied to poly(o-aminophenol) film electrodes. *J. Electroanal. Chem.* 416: 1-24.
- [38] Fuchs, F. (1938). The conductivity of thin metallic films according to the electron theory of metals. *Proc. Camb., Phil. Soc. Math. Phys. Sci.* 34: 100-155.
- [39] Sondheimer, E.H. (1952). Electrical transport in metallic films. *Adv. Phys.*, 1: 1-143.
- [40] Tucceri, R.I. (2003). Specularity change on a thin gold film surface coated with poly(o-aminophenol) during the polymer redox conversion. The pH effect of the redox sites distribution at the metal/polymer interface. *J. Electroanal. Chem.* 543: 61-71.
- [41] Romeo, F.M.; Tucceri, R.I.; Posadas, D. (1988). Surface conductivity changes during the electrochemical adsorption of upd layers on silver and gold. *Surf. Sci.* 203: 186-200.



### ***Chapter 3***

# **THE EFFECT OF CERIUM CONTENT ON THE CORROSION BEHAVIOR OF AMORPHOUS $\text{Al}_{85}\text{Ce}_x\text{Ni}_{15-x}$ ( $x = 4, 5, 6, 7$ , AND $10$ ) ALLOYS OBTAINED BY MELT SPINNING**

***Carlos Triveño Ríos<sup>1</sup>, Mara Cristina Lopes de Oliveira<sup>2</sup>  
and Renato Altobelli Antunes<sup>1,\*</sup>***

<sup>1</sup>Centro de Engenharia, Modelagem e Ciências Sociais Aplicadas (CECS), Universidade Federal do ABC (UFABC), Santo André, Brazil

<sup>2</sup>Electrocell Ind. Com. Equip. Elet. LTDA, Centro de Inovação, Empreendedorismo e Tecnologia (CIETEC), São Paulo, Brazil

## **ABSTRACT**

The aim of the present work was to study the effect of the cerium content on the corrosion behavior of  $\text{Al}_{85}\text{Ce}_x\text{Ni}_{15-x}$  ( $x = 4, 5, 6, 7$  and  $10$ ) amorphous alloys obtained by melt spinning. The as-quenched amorphous ribbons were studied by differential scanning calorimetry and the amorphous character was confirmed by X-ray diffraction and transmission electron microscopy. The corrosion behavior was investigated using electrochemical impedance spectroscopy and

---

\* Corresponding author Email: renato.antunes@ufabc.edu.br.

potentiodynamic polarization. The results showed that the  $\text{Al}_{85}\text{Ce}_x\text{Ni}_{15-x}$  alloys were amorphous independently of the cerium concentration. The corrosion behavior was dependent on the cerium concentration. The general corrosion resistance decreased with the cerium content. However, increasing the cerium content led to a beneficial effect on the localized corrosion resistance of the alloys.

**Keywords:** Al-Ce-Ni, amorphous alloys, melt spun ribbons, corrosion, crystallization

## 1. INTRODUCTION

Metallic alloys obtained in the amorphous state from rapid solidification techniques are attractive technological materials. The major interests in their actual engineering applications derive from a combination of attributes such as high corrosion resistance, mechanical stability and excellent magnetic properties [1-3]. This outstanding performance relies on the unique structural features of metallic glasses such as the absence of crystalline defects, especially grain boundaries, dislocations and stacking faults [4, 5].

In this scenario, Al-TM-RE (TM: transition metal element; RE: rare earth element) alloys have inspired several investigations due to the enhanced ductility and thermal stability when compared to other amorphous aluminum-based systems [6, 7]. Nickel is frequently incorporated as the transition metal in these systems due to its beneficial effect on the glass forming ability (GFA) of the alloy [8]. Indeed, GFA is a major aspect driving the development of Al-Ni-RE amorphous alloys. Several investigations were based on the study of how different compositions affect the GFA of Al-Ni-RE amorphous alloys [9-11]. Different rare earth elements have been added to Al-Ni-RE systems in order to improve glass forming ability [12, 13]. GFA of Al-Ni-RE alloys was found to vary linearly with the size of the rare earth atom. In this respect, the atomic radius of La is 0.1877 nm whereas that of Ce is 0.1822 nm [14]. Notwithstanding, the mixing enthalpy of Ni-Ce (-28 kJ.mol<sup>-1</sup>) is more negative than that of Ni-La (-27 kJ.mol<sup>-1</sup>) and this would favor the formation of a glassy alloy [1]. This favorable picture has triggered the development of ternary Al-Ni-Ce amorphous alloys.

The corrosion resistance of amorphous alloys is frequently reported as an advantageous property over their crystalline counterparts allowing for the applications of metallic glasses in a variety of environments [15, 16]. The

electrochemical behavior of glassy alloys is affected by their atomic structure which, in turn, depends on the crystallization behavior. Li et al. [17] studied the corrosion properties of Al-Ni-Gd glassy alloys. They observed that the tendency for metastable pitting in chloride containing solutions increased with the nickel concentration in the alloy. This result was explained based on the residual stress between the nickel-rich corroded part and the uncorroded matrix, leading to the formation of cracks that were preferential sites for pit nucleation. In another publication [18] the same research group has investigated the corrosion behavior of Al<sub>86</sub>Ni<sub>9</sub>La<sub>5</sub> amorphous alloys submitted to different annealing temperatures. The formation of nanocrystalline phases at specific heat treatment condition improved the corrosion resistance of the Al-based alloy. The improved corrosion resistance after formation of nanocrystalline phases upon annealing of metallic glasses was ascribed to the increased stability of the passive film. This effect can be a consequence of faster diffusion of passive elements at the interface between the amorphous phase and nanocrystalline particles and the uniform distribution of impurities allowing the formation of a stable passive film [19, 20]. Recently, Jindal et al. [21] studied the corrosion behavior of Al-Ni-Y glassy alloys and reported that surface chemistry played a central role in the electrochemical stability of the amorphous materials. The affinity of yttrium by oxygen promoted the formation of a more stable passive film upon annealing the samples at 150°C. X-ray photoelectron spectroscopy (XPS) analyses showed that yttrium was enriched on the surface of annealed samples with respect to the as-spun state. As a consequence, the corrosion resistance increased due to the increased stability of the oxide film with yttrium incorporation. Tailleart et al. [22] investigated the corrosion behavior of Al-Co-Ce amorphous alloys. They studied three different crystalline states: fully amorphous alloys, partially relaxed structure containing crystalline precipitates detected by X-ray diffraction analyses and devitrified structures. The precipitate-containing and devitrified structures were obtained after annealing at specific temperatures. They observed that the pitting potential determined from potentiodynamic polarization tests in NaCl solution was affected by the crystalline state. It was higher for the partially relaxed alloy when compared to the as-spun ribbons. The alloy was relaxed by heating at temperatures below 308°C without extended devitrification, but presenting the formation of aluminum nanocrystals. However, it was possible to infer if the relaxation process improved the stability of the passive film or lowered pit initiation and growth rates. It was observed, though, that relaxation was not effective at diminishing advanced active dissolution and did not affect repassivation stages. This was

indicated by the similar repassivation potentials presented by the as-spun and relaxed alloys. Sweitzer et al. [23] studied the localized corrosion behavior of Al-Fe-Y and Al-Ni-Gd alloys in NaCl solution. They evaluated the resistance to pitting corrosion after annealing treatments undertaken to provide controlled formation of nanocrystals or fully crystalline structures and to compare these structures with the fully amorphous states of the Al-based alloys. Higher pitting and repassivation potentials were associated to the fully amorphous and nanocrystalline states, whereas the crystalline materials were more susceptible to micrometer scale-pitting. According to these authors, two effects can be considered to explain the increased stability of the amorphous and nanocrystalline states with respect to the onset of pitting corrosion. The first one is related to elimination of grain boundaries and second phase particles that act as pit initiation sites. The second one relies on the fact that transition metals and rare earth elements in solid solution may enhance the corrosion resistance of metallic alloys by improving the passive film stability in aqueous electrolytes. These effects have been documented by several authors [24-26]. Additional effects can be related to changes in the dissolution kinetics inside pits and formation of insoluble compounds that hamper pit stabilization [27, 28].

Whereas the crystallization behavior of Al-Ce-Ni amorphous alloys has been reported in the literature [29-32], studies devoted to the corrosion behavior of this promising glass forming system are scarce. The aim of the present work was to investigate the correlation between alloy composition and corrosion resistance for Al-Ce-Ni metallic glasses produced by melt spinning. The melt spun ribbons were characterized by X-ray diffraction, differential scanning calorimetry and transmission electron microscopy. Corrosion studies were carried out using electrochemical impedance spectroscopy and potentiodynamic polarization.

## 2. EXPERIMENTAL PROCEDURE

$\text{Al}_{85}\text{Ce}_x\text{Ni}_{15-x}$  with  $x = 4, 5, 6, 7$  and  $10$  (atomic composition) alloys were prepared by arc-melting the mixtures of high purity elements in a copper crucible. The crucible was water-cooled and the casting operation was carried out under argon atmosphere and repeated several times, thus ensuring compositional homogeneity for the ingots. The as-cast ingots were, then, used to produce ribbons through single roller melt-spinning under argon atmosphere, using a water-cooled copper wheel at a circumferential velocity of

42 m.s<sup>-1</sup>. Ribbons dimensions were 3 mm and 40 µm for the width and thickness, respectively.

The ribbons were structurally characterized by X-ray diffraction with CuK $\alpha$  radiation ( $\lambda = 0.1542$  nm) on a Philips X'pert powder diffractometer in  $\theta - 2\theta$  geometry. Additionally, the structure of selected compositions was also analyzed using a transmission electron microscope (TEM) Jeol JEM 2010 equipped with an energy dispersive x-ray (EDS) detector. Samples for TEM observation were prepared by focused ion beam (FIB) milling. Thermal analysis of the melt-spun ribbons was carried out by differential scanning calorimetry (DSC) under high purity argon flow at a heating rate 0.5 K.s<sup>-1</sup> in a Perkin Elmer DSC-7.

Electrochemical characterization was carried out using an Autolab PGSTAT100 potentiostat/galvanostat. The measurements were performed in NaCl 3.5wt.% solution at room temperature in a conventional three-electrode cell set-up. The immersion time was up to 8 days. A saturated calomel electrode (SCE) was used as reference, a platinum wire as the counter-electrode and the Al-Ce-Ni alloys as the working electrodes. The specimens were initially degreased with acetone, washed with deionized water and dried in hot air stream provided by a standard heat gun. The open circuit potential was initially monitored for 30 minutes in order to ensure a steady state condition. Next, electrochemical impedance spectroscopy (EIS) measurements were performed at the open circuit potential in the frequency range from 100 kHz to 0.01 Hz with amplitude of the perturbation signal of  $\pm 10$  mV (rms) at an acquisition rate of 10 points per decade. Right after the EIS measurements, the specimens were submitted to potentiodynamic polarization at a sweep rate of 1 mV.s<sup>-1</sup> starting from -0.25 V with respect to the open circuit potential up to 0.5 V<sub>SCE</sub>. All potentials mentioned throughout the text are given referred to the SCE. The specimens were tested in triplicate.

### 3. RESULTS AND DISCUSSION

#### 3.1. Structural and Thermal Characterization

The XRD patterns of the Al<sub>85</sub>Ce<sub>x</sub>Ni<sub>15-x</sub> alloys are shown in Figure 1. The diffractograms exhibit a broad halo in the  $2\theta$  range between 32° and 48° independently of the cerium concentration, indicating the amorphous character of the as-spun ribbons. The amorphous character of the alloys was confirmed

using TEM analysis. This is exemplified in Figure 2 for the Al<sub>85</sub>Ce<sub>7</sub>Ni<sub>8</sub> alloy. Featureless contrast in the bright field TEM image and absence of spots in the high resolution TEM image (HRTEM) along with the broad halo in the selected area electron diffraction (SAED) pattern confirm the amorphous nature of this alloy. Similar observations were made for the other alloys and the results are not presented here. Another distinguishable feature in the XRD patterns is the presence of a small hump next to the broad halo at 42° to 48° whose intensity decreases as the cerium concentration increases. Such structural feature has been reported for Al<sub>87</sub>Co<sub>10</sub>Ce<sub>3</sub> amorphous ribbons and is associated with the presence of small nuclei of crystalline phases [33]. Although not detected with TEM analysis, the occurrence of similar structural features for the Al<sub>85</sub>Ce<sub>x</sub>Ni<sub>15-x</sub> system studied in the present work should not be disregarded.

Figure 3 shows the DSC thermograms of the melt-spun ribbons of the Al<sub>85</sub>Ce<sub>x</sub>Ni<sub>15-x</sub> alloys. The DSC curves show the occurrence of two exothermic peaks for compositions up to 7% Ce, indicating that structural transformation into the final phases took place in two single steps. Crystallization occurred with three exothermic peaks for the Al<sub>85</sub>Ce<sub>10</sub>Ni<sub>5</sub> alloy, indicating a different transformation sequence.

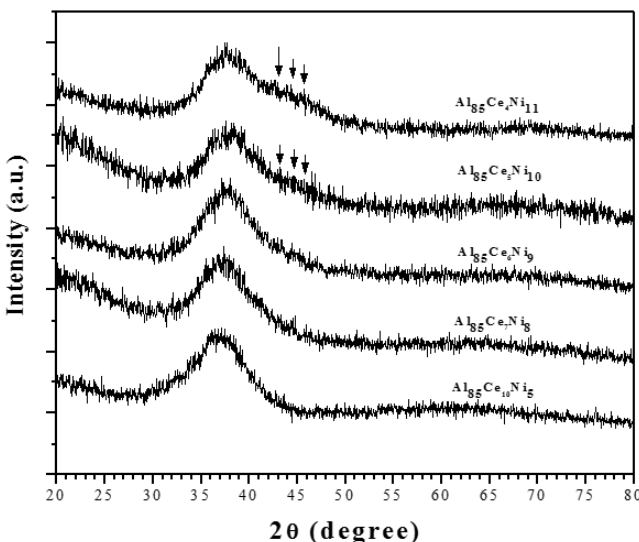


Figure 1. XRD patterns of melt spun ribbons of Al<sub>85</sub>Ce<sub>x</sub>Ni<sub>15-x</sub> alloys.

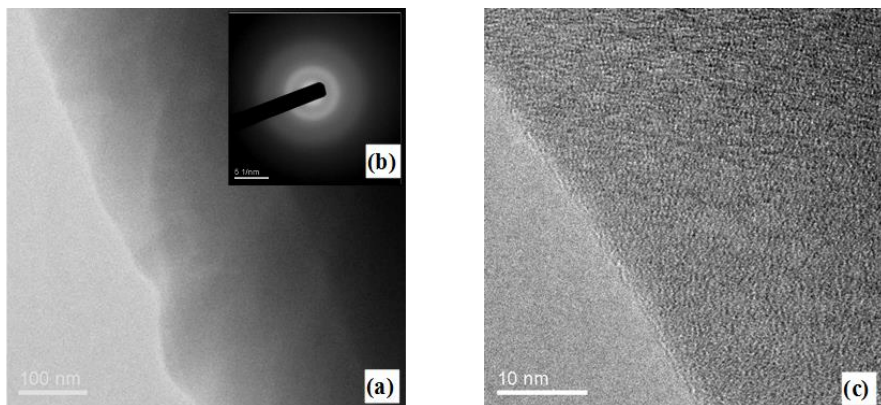


Figure 2. (a) TEM image (bright field) and (b) SAED pattern of the  $\text{Al}_{85}\text{Ce}_7\text{Ni}_8$  alloy; (c) corresponding HRTEM image.

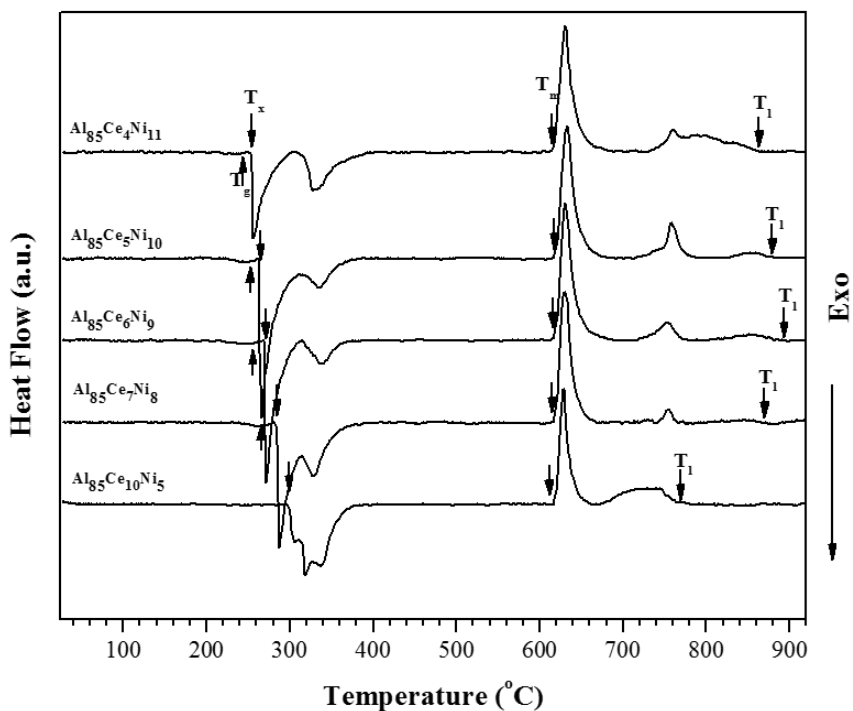


Figure 3. DSC thermograms of the  $\text{Al}_{85}\text{Ce}_x\text{Ni}_{15-x}$  alloys.

The alloys containing up to 7% Ce showed a clear glass transition temperature,  $T_g$ , but  $T_g$  was not detected for Al<sub>85</sub>Ce<sub>10</sub>Ni<sub>5</sub> alloy. The supercooled liquid region ( $\Delta T_x = T_x - T_g$ ) increased from 8.9 to 19.9 K as the Ce content increased from 4 to 7% and the Ni content simultaneously decreased from 11 to 8%.

All the samples showed a sharp endothermic peak with an extended tail involving other peaks of smaller intensity, suggesting that the Al–Ni–Ce alloys were not in a eutectic composition. By increasing the Ce content, the melting temperature ( $T_m$ ) remained almost constant; however, the behavior of the *liquidus* temperature ( $T_L$ ) was different, which was ascribed to the detection or non-detection of  $T_g$ . For instance,  $T_g$  was not detected in Al<sub>85</sub>Ce<sub>10</sub>Ni<sub>5</sub> alloy and  $T_g$  was detected in the alloys with up to 7% Ce; in this case,  $T_g$  increased from 517.3 K to 536.6 K when the Ce content raised from 4% to 7%. On the other hand, the formation of Al<sub>85</sub>Ce<sub>x</sub>Ni<sub>15-x</sub> amorphous alloys might be explained by the empirical rules proposed by Inoue [1] for multicomponent alloys.

### 3.2. Corrosion Behavior

EIS measurements of the Al<sub>85</sub>Ce<sub>x</sub>Ni<sub>15-x</sub> alloys were carried out in a NaCl 3.5 wt.% solution at room temperature after 8 days of immersion. The results are shown in Figure 4. Nyquist plots (Figure 4a) are characterized by the presence of a capacitive loop whose radius decreases as the cerium content increase up to 6 at.%. The diameter of the capacitive loop at the lowest frequencies is associated with the general corrosion resistance of the electrode surface [21]. Thus, our results indicate that the corrosion resistance is reduced as nickel is replaced by cerium in the alloy. This effect is not sustained for the Al<sub>85</sub>Ce<sub>7</sub>Ni<sub>8</sub> alloy for which the diameter of the capacitive loop increased at the lowest frequencies when compared to the Al<sub>85</sub>Ce<sub>5</sub>Ni<sub>10</sub> and Al<sub>85</sub>Ce<sub>6</sub>Ni<sub>9</sub> alloys. When the cerium content is further increased to 10 at.%, the corrosion resistance is depressed as suggested by the decrease of the diameter of the capacitive loop.

Bode plots of the alloys are also showed in Figures 4b and 4c. Phase angle plots (Figure 4b) are clearly characterized by the presence of two time constants. The first one appear at the medium to high frequency domain whereas the second time constant appears in the low frequency region of the plot. This behavior was observed for all the alloys, suggesting that the corrosion mechanism is governed by the same features. The variation of the log |Z| with frequency (Figure 4c) confirms the indications of the Nyquist

plots. The highest value of  $|Z|$  at low frequency was observed for the Al<sub>85</sub>Ce<sub>4</sub>Ni<sub>11</sub> alloy. This value is associated with the corrosion resistance of the alloy and diminishes with increase of the cerium content up to 6 at.%. Then, it increases again for the Al<sub>85</sub>Ce<sub>7</sub>Ni<sub>8</sub> alloy.

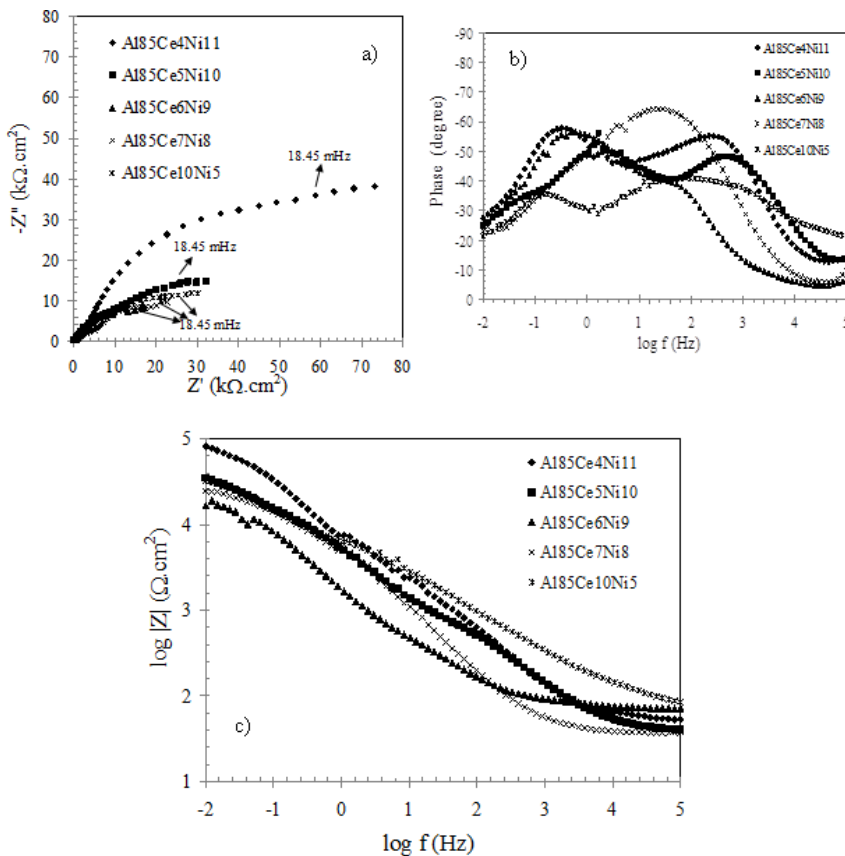


Figure 4. EIS plots of the Al<sub>85</sub>Ce<sub>x</sub>Ni<sub>15-x</sub> alloys: (a) Nyquist; (b) Bode phase angle plot; (c) Bode magnitude plot.

A more quantitative analysis of the EIS data was carried out using an electrical equivalent circuit. A two-time constant model was employed to simulate the experimental data by means of a non-linear least square procedure using the FRA software. The circuit is shown in Figure 5. This model applied well to all the alloys and consists of the following elements: R<sub>1</sub> is the electrolyte resistance; R<sub>2</sub> is the oxide film resistance and Q<sub>1</sub> is the capacitance

of CPE<sub>1</sub> and models the capacitance associated with the oxide film. This element is associated with the first time constant in the medium to high frequencies. Next, a second element is used to model the charge transfer reactions at the base of the defects of the oxide film. R<sub>3</sub> is the charge transfer resistance, Q<sub>2</sub> is the capacitance of CPE<sub>2</sub> and is used to model the double layer capacitance at the interface between the metallic surface and the electrolyte. Constant phase elements (CPEs) were used instead of pure capacitors in order to account for the surface heterogeneities. The exponent of the CPE (n) is a measure of these heterogeneities, being 1 for pure capacitors and 0.5 for diffusion-controlled processes [34]. Circuit parameters are displayed in Tab. 1. The impedance of a CPE is given by equation (1) where Q is the CPE capacitance, n is the CPE exponent, j is the complex variable and ω is the angular frequency.

$$Z_{CPE} = [Q(j\omega)^n]^{-1} \quad (1)$$

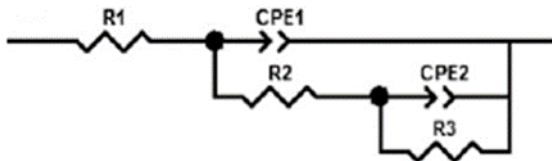


Figure 5. Equivalent circuit used to simulate the EIS experimental data.

**Table 1. EIS fitting parameters obtained using the equivalent circuit shown in Figure 5**

Alloy	R <sub>1</sub> (Ω.cm <sup>2</sup> )	Q <sub>1</sub> (10 <sup>-4</sup> F.cm <sup>2</sup> .s <sup>n-1</sup> )	R <sub>2</sub> (kΩ.cm <sup>2</sup> )	n <sub>1</sub>	Q <sub>2</sub> (10 <sup>-4</sup> F.cm <sup>2</sup> .s <sup>n-1</sup> )	R <sub>3</sub> (kΩ.cm <sup>2</sup> )	n <sub>2</sub>
Al <sub>85</sub> Ce <sub>4</sub> Ni <sub>11</sub>	50.7	0.15	5.13	0.72	0.25	106	0.76
Al <sub>85</sub> Ce <sub>5</sub> Ni <sub>10</sub>	37.7	0.21	0.73	0.73	0.55	49.7	0.58
Al <sub>85</sub> Ce <sub>6</sub> Ni <sub>9</sub>	73.5	0.95	1.13	0.69	0.45	16.2	0.93
Al <sub>85</sub> Ce <sub>7</sub> Ni <sub>8</sub>	37.0	0.33	8.40	0.79	1.04	43.8	0.46
Al <sub>85</sub> Ce <sub>10</sub> Ni <sub>5</sub>	60.7	0.37	14.3	0.51	0.75	30.2	0.90

The data in Table 1 shows that  $R_2$  decreases when the cerium content increases from 4 at.% up to 6 at.% and then increases again for the Al<sub>85</sub>Ce<sub>7</sub>Ni<sub>8</sub> alloy. The same occurs for the value of  $R_3$ . The total resistance can be approximately given by the sum of  $R_2 + R_3$  which is nearly equal to polarization resistance. In this regard, the corrosion resistance seems to be governed by the cerium content, being depressed up to 6 at.% and increasing for higher cerium contents. Moreover, the capacitance of the oxide film ( $Q_1$ ) follows a similar trend. It increases up to a cerium content of 6 at.% and then decreases for higher contents. The capacitance variation is related to the area exposed to the electrolyte. Increasing capacitances are associated with an increment of the reactive area and, hence, to a higher corrosion susceptibility [35]. Another aspect to be considered is that the capacitance decreases for thicker oxide films. In this respect, the values of  $Q_1$  obtained for the Al<sub>85</sub>Ce<sub>7</sub>Ni<sub>8</sub> and Al<sub>85</sub>Ce<sub>10</sub>Ni<sub>5</sub> alloys suggest that the oxide film formed on these surfaces would be thicker than those formed on the Al<sub>85</sub>Ce<sub>5</sub>Ni<sub>10</sub> and Al<sub>85</sub>Ce<sub>5</sub>Ni<sub>10</sub> alloys.

Potentiodynamic polarization curves for the Al<sub>85</sub>Ce<sub>x</sub>Ni<sub>15-x</sub> alloys obtained after 8 days immersion in NaCl 3.5 wt.% solution at room temperature are shown in Figure 6. Electrochemical parameters determined from these curves are shown in Table 2. The values of corrosion potential ( $E_{corr}$ ), pitting potential ( $E_{pit}$ ), corrosion current density ( $i_{corr}$ ), passive current density ( $i_{pass}$ ) and passive range width ( $\Delta E = E_{pit} - E_{corr}$ ) are provided. The values of  $i_{corr}$  have been determined using the Tafel extrapolation method, considering only the cathodic branches. This is an acceptable approximation for determining  $i_{corr}$  when the polarization curves are characterized by the presence of a passive range in the anodic branch, preventing an accurate determination of the anodic Tafel slope [36]. The values of  $i_{pass}$  were determined at the middle of the passive range [37].

The values of  $E_{corr}$  were shifted to more negative potentials as the cerium content increased. A similar behavior has been reported other Al-Ni-RE systems such Al-Ni-Gd [17]. The addition of a rare earth element can have a detrimental effect over the thermodynamic stability of the electrode surface, since this type of element is more active than Al and Ni, thus decreasing the corrosion potential of the alloy. The standard electrode potential of Ce is -2.34 V<sub>SHE</sub> whereas those of Al and Ni are -1.66 V<sub>SHE</sub> and -0.25 V<sub>SHE</sub>, respectively [17, 38]. This behavior facilitates the occurrence of the anodic processes and, as a consequence, the corrosion current densities increased with the cerium content as well as the passive current densities.

The polarization curves are characterized by a passive behavior independently of the cerium content. Passivation has been found in other Al-Ce-Ni systems for as-spun ribbons such as AlLaNi [18], AlYNi [21] and AlGdNi [17]. The extension of the passive range ( $\Delta E$ ) decreased as the cerium content increased up to 6 at.% and then increased again for the Al<sub>85</sub>Ce<sub>7</sub>Ni<sub>8</sub> and Al<sub>85</sub>Ce<sub>10</sub>Ni<sub>5</sub> alloys. The same trend is followed by the pitting potential ( $E_{pit}$ ) that was defined as the potential at which the current density sharply and continuously increases with the applied potential [39]. High values of  $E_{pit}$  and wide passive ranges are associated with a more stable passive film capable of withstanding pitting corrosion at nobler applied potentials [40]. Hence, these results point to an initial decrease of the passive film stability as the cerium content reaches 6 at.% followed by an improved pitting corrosion resistance as the cerium content is further increased. These results are in agreement with the general corrosion behavior observed with the EIS measurements. Hence, there is an apparent critical cerium concentration above which the stability of the passive film is further enhanced. As obtained from the simulation of the EIS experimental data, the decrease of the values of  $Q_1$  and the increase of the values of  $R_1$  for a cerium content above 6 at.% could also reflect this behavior.

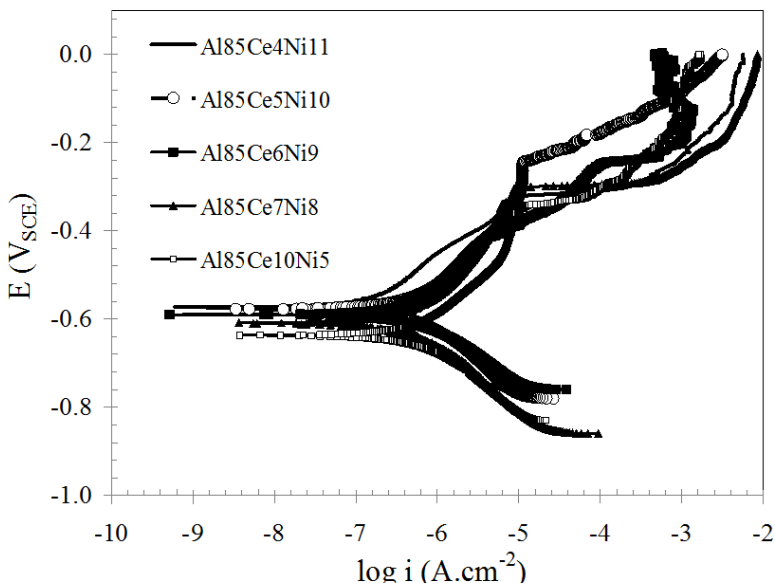


Figure 6. Potentiodynamic polarization curves of the Al<sub>85</sub>Ce<sub>x</sub>Ni<sub>15-x</sub> alloys obtained after 8 days immersion in NaCl 3.5 wt.% solution at room temperature.

**Table 2. Electrochemical parameters obtained from the potentiodynamic polarization curves**

Alloy	$E_{corr}$ (mV <sub>SCE</sub> )	$E_{pit}$ (mV <sub>SCE</sub> )	$\Delta E$ (mV <sub>SCE</sub> )	$i_{pass}$ ( $\mu\text{A.cm}^{-2}$ )	$i_{corr}$ ( $\mu\text{A.cm}^{-2}$ )
Al <sub>85</sub> Ce <sub>4</sub> Ni <sub>11</sub>	-574	-324	250	1.04	0.16
Al <sub>85</sub> Ce <sub>5</sub> Ni <sub>10</sub>	-577	-259	318	3.80	0.50
Al <sub>85</sub> Ce <sub>6</sub> Ni <sub>9</sub>	-590	-415	175	2.34	0.49
Al <sub>85</sub> Ce <sub>7</sub> Ni <sub>8</sub>	-610	-316	294	3.16	0.51
Al <sub>85</sub> Ce <sub>10</sub> Ni <sub>5</sub>	-637	-352	285	4.25	0.55

The increment of the passive range as the cerium content increases can be caused by the relatively high thermodynamic stability of cerium in comparison with nickel. As denoted by the Pourbaix diagrams of these elements [41], cerium is passive in a wider pH range than nickel. This could imply that an increment of the cerium content would lead the formation of a more stable passive film. In this context, in spite of the shift of  $E_{corr}$  and  $i_{corr}$  to less noble values, the pitting corrosion resistance is higher for the alloys with increased cerium concentration.

Working with the same alloys studied here, our group has demonstrated using differential scanning calorimetry (DSC) analysis that the glass forming ability (GFA) of the Al<sub>85</sub>Ce<sub>x</sub>Ni<sub>15-x</sub> alloys increased with the cerium content [31]. Thus, it is interesting to note that the pitting corrosion resistance follows the same trend of the GFA of the Al<sub>85</sub>Ce<sub>x</sub>Ni<sub>15-x</sub> alloys. In spite of the fact that the passivation behavior of a metallic alloy is fundamentally governed by the composition of the passive film [42] and not directly related to the structural features of the bulk alloy, our results point to an agreement between GFA and the pitting corrosion resistance. Other authors have also reported on the increased corrosion resistance of metallic materials with improved GFA in different systems such as Zr-Cu-Al and Zr-Cu-Al-Co [43, 44]. It seems that the concomitant effect of adding an element with a negative heat of mixing with the major components of the alloy, which enhances GFA, combined with a high thermodynamic stability of its oxidized form can provide a suitable combination of enhanced GFA and resistance to localized corrosion. However, in spite of the indications obtained in the present work, further studies with other alloy systems are needed to confirm this hypothesis.

## CONCLUSION

The amorphous character of the as-spun ribbons was confirmed independently of the cerium content. The glass transition temperature,  $T_g$ , and the supercooled liquid region,  $\Delta T_x$ , were affected by the cerium content. Cerium addition presented two conflicting effects regarding the corrosion behavior of the  $Al_{85}Ce_xNi_{15-x}$  system. In one hand, it led to higher dissolution rate by decreasing the corrosion potential and facilitating the onset of the anodic processes. On the other hand, it promoted the formation of a more stable passive film, increasing the passive range of the amorphous alloys.

## ACKNOWLEDGMENTS

Authors acknowledge the Brazilian agencies Fundação de Amparo à Pesquisa do Estado de São Paulo (FAPESP) and Conselho Nacional de Desenvolvimento Científico e Tecnológico (CNPq) for their financial support. Dr. Claudio Shintyi Kiminani and Dr. Walter José Botta Filho from the Federal University of São Carlos are kindly acknowledged for the use of the melt spinning apparatus.

## REFERENCES

- [1] Inoue A., 2000. Stabilization of metallic supercooled liquid and bulk amorphous alloys. *Acta Mater.* 48, 279-306.
- [2] Han B., Kim Y. K., Choi-Yim H., 2014. Effect of compositional variation on the soft magnetic properties of  $Fe_{(87-x-y)}Co_xTi_7Zr_6By$  amorphous alloys. *Current Appl. Phys.* 14, 685-687.
- [3] Vincent S., Khan A. F., Murty B. S., Bhatt J., 2013. Corrosion characterization of melt spun  $Cu_{60}Zr_{20}Ti_{20}$  metallic glass: An experimental case study. *J. Non-Cryst. Solids* 379, 48-53.
- [4] Greer A. L., Ma E., 2007. Bulk metallic glasses: At the cutting edge of metals research. *MRS Bull.* 32, 611-619.
- [5] Kong F. L., Chang C. T., Inoue A., Shalaan E., Al-Marzouki F., 2014. Fe-based amorphous soft magnetic alloys with high saturation magnetization and good bending ductility. *J. Alloys Compd.* 615, 163-168.

- [6] Gu X. J., Wang J. Q., Ye F., Lu K., 2001. Influence of pressure on crystallization kinetics in an Al-Ni-Ce-Fe amorphous alloy. *J. Non-Cryst. Solids* 296, 74-80.
- [7] Sun F., Gloriant T., 2009. Primary crystallization process of amorphous Al<sub>88</sub>Ni<sub>6</sub>Sm<sub>6</sub> alloy investigated by differential scanning calorimetry and by electrical resistivity. *J. Alloys Compd.* 477, 133-138.
- [8] Sun S. P., Yi D. Q., Liu H. Q., Zang B., Jiang Y., 2010. Calculation of glass forming ranges in Al-Ni-Re (Ce, La, Y) ternary alloys and their sub-binaries based on Miedema's model. *J. Alloys Compd.* 506, 377-387.
- [9] Zhang Z., Xiong X. Z., Zhou W., Lin X., Inoue A., Li J. F., 2013. Glass forming ability and crystallization behavior of Al-Ni-RE metallic glasses. *Intermetallics* 42, 23-31.
- [10] Yi J. J., Xu W., Xiong X. Z., Kong L. T., Ferry M., Li J. F., 2015. Influence of mutual substitution between La and Gd on the glass-forming ability of Al-Ni-La-Gd alloys. *J. Alloys Compd.* 628, 245-250.
- [11] Aliaga L. C. R., Danez G. P., Kiminami C. S., Bolfarini C., Botta W. J., 2011. Topological instability and glass forming ability of Al-Ni-Sm alloy. *J. Alloys Compd.* 5095, S141-S144.
- [12] Chen S.-F., Chen C.-Y., Lin C.-H., 2015. Insight on the glass-forming ability of Al-Y-Ni-Ce bulk metallic glass. *J. Alloys Compd.* 637, 418-425.
- [13] Zhang Z., Xiong X.-Z., Yi J.-J., Li J.-F., 2013. Effects of substitution of La by other rare-earth elements on the glass forming ability of Al<sub>86</sub>Ni<sub>9</sub>La<sub>5</sub> alloy. *J. Non-Cryst. Solids* 369, 1-4.
- [14] Inoue A., 1998. Amorphous, nanoquasicrystalline and nanocrystalline alloys in Al-based systems. *Prog. Mater. Sci.* 43, 365-520.
- [15] Yoshida H., Yoshida S., Kawashima A., Asami K., Hashimoto K., 1986. The pitting corrosion behavior of rapidly solidified aluminum alloys. *Corros. Sci.* 26, 795-812.
- [16] Nam S. W., Kim W. T., Kim D. H., Kim T. S., 2013. Microstructure and corrosion behavior of rapidly solidified Mg-Zn-Y alloys. *Met. Mater. Int.* 19, 205-209.
- [17] Li G. H., Pan S. P., Qin J. Y., Zhang Z. H., Wang W. M., 2013. Insight into thermodynamics and corrosion behavior of Al-Ni-Gd glassy alloys from atomic structure. *Corros. Sci.* 66, 360-368.

- [18] Li G. H., Wang W. M., Ma H. J., Li R., Zhang Z. H., Niu Y. C., Qu D. J., 2011. Effect of different annealing atmospheres on crystallization and corrosion resistance of Al<sub>86</sub>Ni<sub>9</sub>La<sub>5</sub> amorphous alloy. *Mater. Chem. Phys.* 125, 136-142.
- [19] Souza C. A. C., Politi F. S., Kiminami C. S., 1998. Influence of structural relaxation and partial devitrification on the corrosion resistance of Fe<sub>78</sub>B<sub>13</sub>Si<sub>9</sub> amorphous alloy. *Scr. Mater.* 39, 329-334.
- [20] Souza C. A. C., Kuri S. E., Politti F. S., May J. E., Kiminami C. S., 1999. Corrosion resistance of amorphous and polycrystalline FeCuNbSiB alloys in sulphuric acid solution. *J. Non-Cryst. Solids* 247, 69-73.
- [21] Jindal R., Raja V. S., Gibson M. A., Styles M. J., Bastow T. J., Hutchinson C. R., 2014. Effect of annealing below the crystallization temperature on the corrosion behavior of Al-Ni-Y metallic glasses. *Corros. Sci.* 84, 54-65.
- [22] Tailleart N. R., Huang R., Aburada T., Horton D. J., Scully J. R., 2012. Effect of thermally induced relaxation on passivity and corrosion of an amorphous Al-Co-Ce alloy. *Corros. Sci.* 59, 238-248.
- [23] Sweitzer J. E., Shiflet G. J., Scully J. R., 2003. Localized corrosion of Al<sub>90</sub>Fe<sub>5</sub>Gd<sub>5</sub> and Al<sub>87</sub>Ni<sub>8.7</sub>Y<sub>4.3</sub> alloys in the amorphous, nanocrystalline and crystalline states: resistance to micrometer-scale pit formation. *Electrochim. Acta* 48, 1223-1234.
- [24] Lee H.-J., Akiyama E., Habazaki H., Kawashima A., Asami K., Hashimoto K., 1996. The corrosion behavior of amorphous and crystalline Ni-10Ta-20P alloys in 12 M HCl. *Corros. Sci.* 38, 1269-1279.
- [25] Virtanen S., Böhni H., 1993. Studies of passive films on amorphous Fe-Cr-(B,P,C) alloys. *Corros. Sci.* 35, 27-34.
- [26] Mansour A. N., Melendres C. A., Poon S. J., He Y., Shiflet G. J., 1996. An X-ray absorption near-edge spectroscopic study of the structure of passive films on amorphous Al-Fe-Ce alloys. *J. Electrochem. Soc.* 143, 614-619.
- [27] Frankel G. S., 1990. The growth of 2-D pits in thin film aluminum. *Corros. Sci.* 30, 1203-1218.
- [28] Szklarska-Smialowska Z., 1992. Insight into the pitting corrosion behavior of aluminum alloys. *Corros. Sci.* 33, 1193-1202.

- [29] Song K., Bian X., Lv X., Guo J., Li G., Xie M., 2009 Compositional dependence of glass-forming ability, medium-range order, thermal stability and liquid fragility of Al-Ni-Ce based amorphous alloys. *Mater. Sci. Eng. A* 506, 87-93.
- [30] Muñoz-Morris M. A., Suriñach S., Varga L. K., Baro M. D., Morris D. G., 2002. The influence of composition and low temperature annealing on hardness and ductility of rapidly solidified Al-Ni-Ce alloys. *Scr. Mater.* 47, 31-37.
- [31] Ríos C. T., Suriñach S., Baró M. D., Bolfarini C., Botta W. J., Kiminami C. S., 2008. Glass forming ability of the Al-Ce-Ni system. *J. Non-Cryst. Solids* 354, 4874-4877.
- [32] Botta W. J., Ríos C. T., Lisboa R. D. S., de Andrade A. R., de Oliveira M. F., Bolfarini C., Kiminami C. S., 2009. Crystallisation behaviours of Al-based metallic glasses: Compositional and topological aspects. *J. Alloys Compd.* 483, 89-93.
- [33] Sun B., Bian X., Guo J., Zhang J., Mao T., 2007. Hump peak formation and the crystallization in amorphous Al87Co10Ce3 alloy. *Mater. Lett.* 61, 111-114.
- [34] Bastos A. C., Ferreira M. G., Simões A. M., 2006. Corrosion inhibition by chromate and phosphate extracts for iron substrates studied by EIS and SVET. *Corros. Sci.* 48, 1500-1512.
- [35] Rosero-Navarro N. C., Pellice S. A., Durán A., Aparicio M., 2008. Effects of Ce-containing sol-gel coatings reinforced with SiO<sub>2</sub> nanoparticles on the protection of AA2024. *Corros. Sci.* 50, 1283-1291.
- [36] Bockris J.O. M., A. K. N. Reddy, Modern Electrochemistry, vol. 2, Plenum Press, New York, 1972, pp. 1265.
- [37] Pillis M. F., Geribola G. A., Scheidt G., de Araújo E. G., de Oliveira M. C. L., Antunes R. A., 2016. Corrosion of thin, magnetron sputtered Nb<sub>2</sub>O<sub>5</sub> films. *Corros. Sci.* 102, 317-325.
- [38] Zhang C., Wang J., Qiu N., Xie K., Li H., 2015. Cerium addition on pitting corrosion of (CuroZr50)100-2xCe2x(x = 0, 1, 2 and 3) metallic glasses in seawater. *J. Rare Earths* 33, 102-106.
- [39] Ha H.-Y., Jang M.-H., Lee T.-H., Moon J., 2015. Understanding the relation between phase fraction and pitting corrosion resistance of UNS S32750 stainless steel. *Mater. Charact.* 106, 338-345.
- [40] Zhang Z., Zhang H., Zhao H., Li J., 2016. Effect of prolonged thermal cycles on the pitting corrosion resistance of a newly developed LDX 2404 lean duplex stainless steel. *Corros. Sci.* 103, 189-195.

- [41] Pourbaix M., *Atlas of Electrochemical Equilibria in Aqueous Solutions*, Pergamon Press, New York, 1966.
- [42] Marcus P., 1994. On some fundamental factors in the effect of alloying elements on passivation of alloys. *Corros. Sci.* 36, 2155-2158.
- [43] Li Y. H., Zhang W., Dong C., Qiang J. B., Fukuhara M., Makino A., Inoue A., 2011. Effects of Ni addition on the glass-forming ability, mechanical properties and corrosion resistance of Zr-Cu-Al bulk metallic glasses. *Mater. Sci. Eng. A* 528, 8551-8556.
- [44] Zhou W., Weng W. P., Hou J. X., 2016. Glass-forming ability and corrosion resistance of ZrCuAlCo bulk metallic glass. *J. Mater. Sci. Technol.* 32, 349-354.

## BIOGRAPHICAL SKETCH

***Renato Altobelli Antunes, PhD***

Federal University of ABC (UFABC)

Av. Dos Estados 5001, Santo André – SP – Brazil Zip code: 09210-580

### **Research and Professional Experience:**

1999-2002 M.Sc. –Materials Science and Engineering - IPEN/CNEN-SP São Paulo – SP – Brazil

2002-2006 PhD – Materials Science and Engineering - IPEN/CNEN-SP São Paulo – SP – Brazil

2004-2008 Professor at Faculdades Oswaldo Cruz, São Paulo – SP - Brazil;

2005-2008 Professor at Centro Universitário Fundação Santo André – Santo André – SP – Brazil

### **Professional Appointments:**

2009- Adjunct Professor, Center for Engineering, Modeling and Applied Social Sciences, Federal University of ABC (UFABC)

### **Publications from the Last 3 Years:**

1. Antunes, R. A.; Lopes De Oliveira, M. C. ; Batista De Souza, J. A.. Effect of temperature on corrosion and semiconducting properties of oxide films formed on M5 zirconium alloy. *Corrosion Engineering, Science and Technology*, v. 51, p. 104-109, 2016.

2. Pillis, Marina Fuser; Geribola, Guilherme Altomari; Scheidt, Guilherme; De Araújo, Edval Gonçalves; De Oliveira, Mara Cristina Lopes; Antunes, Renato Altobelli. Corrosion of thin, magnetron sputtered Nb<sub>2</sub>O<sub>5</sub> films. *Corrosion Science*, v. 102, p. 317-325, 2016.
3. De Oliveira, A. Carolina; De Oliveira, M. C. Lopes; Ríos, C. T.; Antunes, R. A. The effect of mechanical polishing and finishing on the corrosion resistance of AISI 304 stainless steel. *Corrosion Engineering, Science and Technology*, v. 51, p. 416-428, 2016.
4. Ríos, Carlos Triveño; De Souza, Juliana Sarango; Antunes, Renato Altobelli. Preparation and characterization of the structure and corrosion behavior of wedge mold cast Fe43.2Co28.8B19.2Si4.8Nb4 bulk amorphous alloy. *Journal of Alloys and Compounds*, v. 682C, p. 412-417, 2016.
5. Santos, R. C. F.; Oliveira, M. C. L.; Antunes, R.A. . Mapping the corrosion behavior of AZ91D magnesium alloy: influence of chloride concentration and potentiostatic polarization. *Innovations in Corrosion and Materials Science*, v. 6, p. 146-156, 2016.
6. ITO, Nathalie Minako; Nacas, Amanda Martins; Antunes, Renato Altobelli; Salvadori, Maria Cecília; Santos, Demetrio JACKSON DOS. Study of the correlation between flexible food packaging peeling resistance and surface composition for aluminum metallized BOPP films aged at 60°C. *The Journal of Adhesion (Print)*, v. 93, p. 4-17, 2017.
7. Santos, D.J. ; Tavares, L. B.; Antunes, R. A.; Droppa Jr, R; Silva, T. F. ; Salvadori, M. C. Properties of aluminum oxide thin film obtained by metal plasma immersion ion implantation and deposition after zirconium-based pretreatment. *Vacuum (Oxford)*, v. 121, p. 32-41, 2015.
8. Dos Santos, Silvano Leal; Antunes, Renato Altobelli; Santos, Sydney Ferreira. Influence of injection temperature and pressure on the microstructure, mechanical and corrosion properties of a AlSiCu alloy processed by HPDC. *Materials & Design*, v. 88, p. 1071-1081, 2015.
9. Fernandes, Stela Maria De Carvalho; Correa, Olandir Vercino; Souza, José Antonio Batista De; Antunes, Renato Altobelli; Lima, Nelson Batista De; Ramanathan, Lalgudi Venkataraman. Effect of Processing on Microstructure and Corrosion Mitigating Properties of Hydrotalcite Coatings on AA 6061 Alloy. *Materials Research*, v. 18, p. 1203-1208, 2015.
10. Oliveira, Mara Cristina Lopes; Pereira, Viviam Serra Marques; Correa, Olandir Vercino; Antunes, Renato Altobelli . Corrosion Performance of Anodized AZ91D Magnesium Alloy: Effect of the Anodizing Potential on

- the Film Structure and Corrosion Behavior. *Journal of Materials Engineering and Performance (Print)*, v. 23, p. 593-603, 2014.
11. Scalise, Taís Campos; De Oliveira, Mara Cristina Lopes; Sayeg, Isaac Jamil ; Antunes, Renato Altobelli. Sensitization Behavior of Type 409 Ferritic Stainless Steel: Confronting DL-EPR Test and Practice W of ASTM A763. *Journal of Materials Engineering and Performance (Print)*, v. 23, p. 2164-2173, 2014.
  12. Antunes, R. A.; Ichikawa, R. U.; Martinez, L. G.; Costa, I.. Characterization of Corrosion Products on Carbon Steel Exposed to Natural Weathering and to Accelerated Corrosion Tests. *International Journal of Corrosion*, v. 2014, p. 1-9, 2014.
  13. Antunes, Renato Altobelli; Oliveira, Mara Cristina Lopes De. Materials selection for hot stamped automotive body parts: an application of the Ashby approach based on the strain hardening exponent and stacking fault energy of materials. *Materials in Engineering (Cessou em 1982. Cont. ISSN 0264-1275 Materials and Design)*, v. 63, p. 247-256, 2014.
  14. Machado, C.A.V.A. ; ANTUNES, R. A. ; Pessine, E.J. ; Correa O.V. . Influence of Testing Temperature on the Corrosion Behavior of API 5L X70 Pipeline Steel. *Journal of Mechanics Engineering and Automation*, v. 4, p. 528-532, 2014.
  15. Rejowski, E.D.; De Oliveira, Mara Cristina Lopes; Antunes, R. A.; Pillis, M.F. . Structural Characterization and Corrosion Stability of a Si-Doped DLC Coating Applied on Cylinder Liner. *Journal of Materials Engineering and Performance (Print)*, v. 23, p. 3926-3933, 2014.
  16. Oliveira, M. C. L.; Sayeg, Isaac Jamil; Ett, G.; Antunes, R. A.. Corrosion behavior of polyphenylene sulfide-carbon black-graphite composites for bipolar plates of polymer electrolyte membrane fuel cells. *International Journal of Hydrogen Energy*, v. 39, p. 16405-16418, 2014.
  17. Altobelli Antunes, Renato; Cristina Lopes De Oliveira, Mara. Hydrogen Embrittlement of Zirconium-Based Alloys for Nuclear Fuel Cladding. *Innovations in Corrosion and Materials Science (Formerly Recent Patents on Corrosion Science)*, v. 04, p. 1-1, 2014.
  18. De Paula, V.C.; ANTUNES, R.A.; OLIVEIRA, M.C.L.. Investigaton on the Effect of Solution Treatment on the Intergranular Corrosion Susceptibility of Cold-Rolled AISI 304 Stainless Steel. *International Journal of Mechanical Engineering and Automation*, v. 1, p. 247-252, 2014.

# INDEX

## A

acetone, 81  
acid, 4, 10, 11, 12, 19, 30, 72, 92  
active site, 53, 66  
adenine, 30  
adhesion, vii, 1, 2, 26  
adsorption, 73, 75  
agencies, 90  
aggregation, 16  
Al-Ce-Ni, 78, 80, 81, 88, 93  
alkaline media, 30  
alpha-fetoprotein, 22  
aluminum oxide, 95  
amine, 9, 55, 65  
amine group, 9  
amino acid, 19  
amino groups, 65  
amorphous alloys, vii, viii, 77, 78, 80, 84, 90, 93  
amplitude, 33, 47, 81  
aniline, 8, 22  
annealing, 79, 92  
anodic stripping voltammetry, 18  
antibody, 12  
antigen, 10, 15, 18, 19, 23  
antitumor, 19  
Argentina, 29  
argon, 80, 81  
asymmetry, 47

atmosphere, 80  
atoms, 55  
Au nanoparticles, 12, 13  
autoimmune diseases, 12

## B

background noise, 4  
bacteria, 4, 7, 8, 11, 18, 20, 26  
barriers, 55  
base, 31, 34, 86  
basic research, 30  
behaviors, 62  
bending, 90  
beneficial effect, ix, 78  
biomarker, viii, 2, 9, 12, 23, 25  
biomolecules, 17, 18  
biosensing, 2, 3, 5, 12, 18, 23, 25, 26  
biosensors, 2, 12, 22, 23, 24, 25, 26  
bode, 5, 84, 85  
Brazil, 77, 94

## C

$\text{Ca}^{2+}$ , 6  
calibration, 12, 13  
calorimetry, 14, 24  
cancer, vii, 1, 2, 7, 9, 10, 11, 12, 15, 20, 22, 23  
cancer cells, 2, 7, 11, 20

carbohydrate, vii, 2, 4, 5, 6, 7, 9, 10, 13, 14, 15, 16, 17, 18, 19, 20, 21, 22, 24, 25, 26, 27  
 carbohydrate–protein interactions, vii, 2, 5, 6, 7, 14, 15, 18, 19, 26  
 carbon, 6, 15, 18, 22, 26, 30, 72, 96  
 carbon nanotubes, 6, 15, 22, 26  
 carboxyl, 9  
 casting, 80  
 cell line, 15  
 cell signaling, 2  
 cell surface, 6, 8, 11, 20  
 cerium, vii, viii, 77, 81, 84, 85, 87, 88, 89, 90  
 charge transfer resistance, 5, 13, 86  
 charge-transfer, 2, 30, 31, 47, 50, 57, 58  
 charge-transfer parameters, 30, 31, 50  
 charge-transfer resistance, 2, 47, 57  
 charge-transport, 30, 37, 41, 50, 53, 56, 57, 61, 62, 70, 74  
 chemical inertness, 5  
 children, 11  
 cleaning, 4, 6, 19, 32  
 coatings, 93  
 colorimetry, 16  
 composites, 96  
 composition, 58, 80, 84, 89, 93, 95  
 compounds, 8, 72, 80  
 Concanavalin A, 8, 10, 22, 24  
 conductance, 18, 55, 73  
 conduction, 46, 55, 56, 62, 63, 64, 65, 69, 70, 71  
 conductivity, 31, 42, 47, 55, 70, 74, 75  
 configuration, 31, 56, 66, 71  
 conflict of interest, 71  
 copper, 80  
 corrosion, vii, viii, 3, 21, 77, 78, 80, 84, 87, 88, 89, 90, 91, 92, 93, 94, 95, 96  
 cracks, 79  
 crystalline, 78, 82, 92  
 crystallization, 78, 79, 80, 82, 91, 92, 93  
 crystallization kinetics, 91  
 current-potential curves, 33, 37, 40  
 cyanide, 6  
 cycles, 32, 93

## D

deactivation, viii, 30, 31, 35, 36, 37, 40, 42, 45, 48, 49, 50, 51, 53, 56, 58, 60, 62, 64, 66, 67, 69, 70, 71  
 deactivation by storage, 30, 31, 42, 58  
 decay, 31  
 defects, 46, 63, 78, 86  
 degradation, 68  
 dengue, 10, 13, 15, 23, 24  
 dengue fever, 10, 13, 15  
 deposition, 46, 95  
 detection, 2, 4, 5, 6, 8, 9, 11, 12, 13, 15, 16, 17, 18, 20, 21, 22, 23, 24, 25, 26, 27, 30, 72, 84  
 differential scanning, viii, 77, 80, 81, 89, 91  
 differential scanning calorimetry, viii, 77, 80, 81, 89, 91  
 diffusion, 5, 37, 38, 41, 43, 46, 47, 48, 50, 53, 54, 55, 56, 57, 58, 61, 70, 71, 79, 86  
 diffusion process, 38, 55, 58  
 discrimination, 13, 22  
 diseases, 9  
 dispersion, 62, 63, 65, 67  
 dissociation, 13, 18  
 dissolved oxygen, 31  
 distribution, 62, 65, 69, 70, 75, 79  
 DNA, 4, 17  
 DNAs, 22  
 drug design, 20  
 drugs, 2, 13  
 DSC, 81, 82, 83, 89  
 ductility, 78, 90, 93  
 durability, 29, 31  
 dyes, 14

## E

E. coli, 11, 15, 16, 17, 18, 24  
 EIS, vii, viii, 1, 2, 3, 4, 5, 6, 7, 9, 11, 12, 13, 14, 15, 16, 17, 18, 19, 21, 29, 37, 62, 65, 70, 71, 74, 81, 84, 85, 86, 88, 93  
 electric current, 3  
 electrical conductivity, 5

electroactivity, viii, 30, 31, 56  
electrocatalysis, 30  
electrochemical behavior, 38, 79  
electrochemical impedance, vii, viii, 1, 3, 14, 20, 21, 22, 23, 27, 46, 74, 77, 80, 81  
electrochemical standard rate constant, 58, 60  
electrochemistry, 73  
electrode surface, 5, 6, 8, 9, 11, 46, 65, 84, 87  
electrodes, vii, viii, 3, 5, 9, 13, 16, 21, 22, 23, 29, 30, 31, 32, 33, 34, 38, 46, 72, 73, 74, 75, 81  
electrolysis, 37  
electrolyte, vii, viii, 5, 29, 31, 32, 34, 35, 36, 37, 41, 46, 47, 48, 51, 56, 58, 71, 85, 87, 96  
electromagnetic, 17  
electron, viii, 3, 5, 21, 30, 31, 37, 38, 40, 41, 47, 48, 52, 53, 56, 60, 62, 63, 65, 67, 69, 70, 71, 74, 75, 81  
electron diffusion coefficient, 41, 43, 53, 54  
endothermic, 84  
energy, 41, 55, 66, 81, 96  
engineering, 78  
environmental factors, 14  
environments, 78  
enzyme, 2, 17, 20  
epididymis, 10  
epithelial cells, 24  
epitopes, 22  
EPR, 96  
equilibrium, 13, 57  
equipment, 33  
ERS, 17, 20  
etching, 6  
ethanol, 4  
ethylene, 25  
ethylene glycol, 25  
evanescent waves, 17  
evaporation, 32, 33, 45, 46  
evolution, 45, 64  
excitation, 3  
exothermic peaks, 82  
extracts, 15, 93

**F**

false positive, 2, 19  
FDA, 9, 10, 12, 23  
ferric ion, viii, 30, 72  
fertilization, 2  
fever, 13  
field-effect transistor, 16, 18, 26  
film thickness, 40, 47, 50, 59, 63, 67, 69  
films, viii, 24, 30, 31, 32, 34, 35, 36, 37, 38, 39, 40, 42, 43, 45, 46, 50, 55, 56, 58, 59, 60, 62, 63, 65, 66, 67, 68, 69, 70, 72, 73, 75, 87, 92, 93, 94, 95  
financial, 90  
financial support, 90  
food, 17, 26, 95  
Food and Drug Administration, 23  
formation, 8, 46, 72, 78, 79, 84, 89, 90, 92, 93  
formula, 3  
fragility, 93  
fragments, 55  
fuel cell, 96

**G**

geometry, 47, 81  
Germany, 33  
glass forming ability, 78, 89, 91, 93  
glass transition temperature, 84, 90  
glasses, 78, 80, 90, 91, 92, 93, 94  
glucose, 10  
glycan, vii, 2, 6, 7, 8, 12, 19, 20, 22, 25  
glycol, 8  
glycoproteins, vii, 2, 8, 10, 12, 13, 15, 22, 23, 24  
glycosylation, viii, 2, 12  
gold nanoparticles, 13, 16, 18, 19, 22, 25, 26, 27  
grain boundaries, 78, 80  
graph, 4  
graphite, 96  
growth, 79, 92  
growth rate, 79

**H**

*H.* pylori, 18  
hardness, 93  
heating rate, 81  
*Helicobacter pylori*, 18  
hepatitis, 22  
hepatocellular carcinoma, 12  
high-frequency semicircle, 45, 52, 58, 60  
history, 3, 21  
HIV, 19, 20  
HIV-1, 20  
homogeneity, 80  
HRTEM, 82, 83  
human, 10, 11, 15, 22, 25  
hybrid, 72  
hybridization, 17  
hydrogen, 45, 54, 71  
hydroquinone, 32, 33, 37, 38  
hypothesis, 89

**I**

immersion, 81, 84, 87, 88, 95  
immobilization, 17  
immunoglobulins, 8  
impedance measurements, 33, 43, 54, 56, 71  
impedance parameters, 56  
impurities, 79  
in vitro, 6  
income, 11  
indium, 6, 8, 15, 30  
individuals, 12  
infection, 2  
inflammation, vii, 1, 2  
inhibition, 55, 93  
inhomogeneity, 5  
initiation, 79  
insertion, 54  
integration, 35  
interaction parameters, 66  
interface, 5, 17, 22, 38, 40, 46, 48, 52, 53,  
  55, 56, 58, 63, 64, 65, 69, 70, 71, 74, 75,  
  79, 86

interference, 6, 17  
ion implantation, 95  
ion transport, 47, 53, 55, 61, 71  
ions, 6, 37, 52, 54, 71  
iron, 93  
isolation, 8  
issues, 4

**K**

$K^+$ , 57  
kinetics, 5, 58, 75, 80

**L**

labeling, 2, 14  
lactose, 16  
laminar, 42  
lead, 63, 65, 89  
Levich equation, 40  
light, 31  
lipids, 4  
liver, 11  
liver cancer, 11  
lysine, 9

**M**

magnesium, 95  
magnetic properties, 78, 90  
magnetization, 90  
magnitude, 51, 53, 56, 61, 85  
mass, 17, 26  
materials, 2, 14, 30, 41, 55, 56, 74, 78, 79,  
  89, 96  
matrix, 79  
mechanical properties, 94  
media, 30, 73, 74  
mediation, 38  
melt, vii, viii, 77, 78, 80, 81, 82, 90  
melt spinning, vii, viii, 77, 80, 90  
melt spun ribbons, 78, 80, 82  
melting, 80, 84  
melting temperature, 84

membranes, 24  
metal ions, 6  
metals, 75, 90  
metastasis, vii, 1, 2  
 $Mg^{2+}$ , 6  
microcalorimetry, 14, 24  
micrometer, 80, 92  
microscope, 81  
microstructure, 95  
migration, 47  
miniature, 25  
Missouri, 1, 19  
mixing, 78, 89  
models, viii, 3, 30, 31, 56, 62, 71, 74, 86  
molar ratios, 8, 9  
mold, 95  
molecular structure, 62  
molecules, vii, 1, 2, 6, 7, 14  
monolayer, 7, 23  
monosaccharide, 20  
Moon, 93  
mucin, 10

**N**

NaCl, 6, 79, 81, 84, 87, 88  
NAD, 30  
nanocrystalline alloys, 91  
nanocrystals, 79  
nanoparticles, 2, 16, 93  
nanotechnology, 14, 23  
nanotube, 18  
Nepal, 1  
neutral, 30  
NHS, 7, 9  
nickel, 79, 84, 89  
nicotinamide, 72  
nitric oxide, 30  
nitrogen, 55  
NMR, 20, 24  
nucleation, 79  
nuclei, 82  
Nyquist, 4, 5, 6, 7, 8, 9, 13, 43, 44, 45, 48,  
    58, 59, 84, 85  
Nyquist diagrams, 43, 58, 59

**O**

oligosaccharide, 20  
opportunities, 22  
ox, 48  
oxidation, 30, 37, 38, 54, 65, 67  
oxygen, 79

**P**

pancreatic cancer, 15  
parallel, 46, 63, 70  
partition, 57  
passivation, 89, 94  
pathogens, 6  
permeability, 31  
permeation, 46  
pH, 42, 50, 57, 58, 59, 75, 89  
phosphate, 6, 93  
physical properties, 62  
plants, 8  
platinum, 30, 81  
PNA, 8, 9, 10, 15  
polarization, viii, 34, 73, 78, 79, 80, 81, 87,  
    88, 89, 95  
poly(*o*-aminophenol) film electrodes, 30,  
    72, 74, 75  
polymer, viii, 8, 21, 22, 30, 31, 32, 37, 38,  
    40, 42, 46, 47, 48, 50, 52, 53, 55, 56, 57,  
    58, 59, 60, 62, 64, 65, 67, 69, 70, 73, 74,  
    75, 96  
polymer chains, 55, 65  
polymer films, 32, 50, 54  
polymer materials, 37, 60  
polymer matrix, 52, 60  
polymers, 20, 42, 55, 56, 62, 72, 73  
poly-*o*-aminophenol, 30, 72, 73  
potassium, 6  
probability, 63  
probe, 2, 4, 5, 6  
proliferation, vii, 1, 2  
propagation, 54, 56, 58  
proportionality, 42  
protection, 93

proteins, vii, 1, 4, 8, 13, 19, 26  
 protons, 54, 56  
 PSA, 10  
*Pseudomonas aeruginosa*, 18  
 purification, 33  
 purity, 80, 81

response, viii, 3, 6, 7, 12, 13, 17, 18, 30, 31,  
 32, 35, 51, 64, 65, 66, 70, 72  
 rheumatoid arthritis, 12  
 room temperature, 81, 84, 87, 88  
 roughness, 5, 46, 63  
 rules, 84

**Q**

quantification, 25  
 quantitative technique, 16  
 quartz, vii, 1, 12, 14, 16, 17, 21, 24, 26  
 quartz-crystal microbalance, 17

**R**

radiation, 81  
 radioactive isotopes, 2  
 radius, 78, 84  
 Raman spectroscopy, 17, 20  
 Randles, 5, 7  
 rare earth elements, 78, 80  
 reactions, 74, 86  
 reading, 19  
 receptor, 2, 6, 7, 9, 11, 12, 16, 17, 18  
 recognition, 20, 25  
 recovery, 11, 12  
 redox probe, 6  
 redox sites distribution, 62, 69, 70, 75  
 refractive index, 17  
 regression, 50  
 relaxation, 75, 79, 92  
 relaxation process, 75, 79  
 reliability, 17  
 repulsion, 66  
 residuals, 50  
 residues, 9  
 resistance, viii, ix, 2, 3, 5, 13, 29, 31, 33, 34,  
 46, 47, 48, 50, 52, 53, 57, 62, 63, 64, 65,  
 66, 67, 68, 69, 70, 71, 73, 74, 78, 80, 84,  
 85, 87, 88, 89, 92, 93, 94, 95  
 resistance measurements, 31, 46, 73  
 resolution, 82

**S**

safety, 2  
 saliva, 12  
 saturation, 90  
 scaling, 49  
 scattering, 46, 62, 63, 64, 65, 70, 71  
 selected area electron diffraction, 82  
 selectivity, vii, 2, 16  
 self-assembled monolayer, 5, 7, 9, 22, 23  
 semicircle, 5, 43, 45, 52, 58, 60  
 sensitivity, vii, 2, 4, 5, 12, 16, 17, 18, 70  
 sensor, 17, 18, 21, 22, 24, 25, 26, 30, 72  
 serum, 4, 10, 11, 12, 13, 15, 22, 23, 24, 25  
 serum albumin, 13  
 showing, 4, 7, 9, 17  
 sialic acid, 10, 12, 17, 19, 24  
 signals, 3  
 silver, 18, 26, 75  
 simulations, 50, 88, 59  
 sodium, 4  
 solar cells, 21  
 sol-gel, 93  
 solidification, 78  
 solution, vii, viii, 5, 6, 8, 14, 16, 29, 31, 32,  
 34, 35, 36, 37, 38, 39, 40, 41, 42, 43, 44,  
 45, 46, 47, 48, 49, 50, 51, 52, 53, 54, 55,  
 56, 57, 58, 59, 61, 70, 79, 81, 84, 87, 88,  
 92  
 species, 11, 32, 38, 46, 47, 48, 50, 65, 74  
 specific adsorption, 46  
 specific heat, 79  
 spectroscopy, vii, viii, 1, 3, 14, 20, 21, 22,  
 23, 27, 74, 77, 80, 81  
 specularity parameter, 46, 63, 66, 69  
 stability, vii, 2, 31, 78, 79, 87, 88, 89  
 steel, 93, 95

storage, vii, viii, 29, 30, 31, 32, 35, 36, 37, 40, 42, 43, 53, 58, 60, 62, 64, 67, 70, 71  
storage time without use, vii, viii, 29, 30, 36, 43, 53, 70  
stress, 79  
structural relaxation, 92  
structure, 17, 46, 49, 59, 63, 69, 72, 74, 79, 81, 91, 92, 95  
substitution, 91  
substrate, 14, 17, 46, 50, 51, 93  
surface chemistry, 79  
surface plasmon resonance, vii, 1, 12, 14, 17, 24, 25, 26, 27  
surface resistance, viii, 29, 62, 71, 73, 74  
SWNTs, 13, 15  
symmetry, 63, 70  
synthesis, vii, 2, 20, 27

**T**

TEG, 8, 9  
TEM, 81, 82, 83  
temperature, 84, 92, 93, 94, 95  
temperature annealing, 93  
tension, 34  
therapeutics, 11  
thermal stability, 78, 93  
thermodynamics, 91  
thermograms, 82, 83  
thin films, 21, 74  
thyroglobulin, 10  
tin, 6, 8, 15, 30  
tin oxide, 6, 8, 15, 30  
transducer, 3  
transference, 47  
transferrin, 15  
transformation, 33, 82  
transistor, 16, 18, 26  
transition metal, 78, 80  
transmission, viii, 77, 80, 81  
transmission electron microscopy, viii, 77, 80  
transport, viii, 3, 21, 30, 37, 40, 42, 50, 53, 55, 56, 57, 60, 62, 70, 71, 74, 75

treatment, 5, 79  
tumor, 10, 12, 19, 23

**U**

uniform, 46, 47, 79  
urinary tract infection, 11, 24  
urine, 12  
USA, 33, 73

**V**

vacuum, 32, 33, 45  
validation, 23, 33  
velocity, 80  
viruses, 2, 4  
viscosity, 48  
voltammetric response, viii, 30, 32, 35, 36, 51, 65, 66, 67, 70  
Vorotyntsev's model, 61

**W**

water, 33, 80, 81  
wires, 16  
workers, 16, 19  
working conditions, vii, 2

**X**

X-ray diffraction, viii, 77, 79, 80, 81, 82  
X-ray photoelectron spectroscopy (XPS), 79

**Y**

yttrium, 79

**Z**

zirconium, 94, 95